University of Alberta

Stability of Biomolecules and Noncovalent Complexes

Studied by Nanoflow Electrospray FT-ICR Mass Spectrometry

by

Rambod Daneshfar   Ⓒ

A thesis submitted to the Faculty of Graduate Studies and Research in partial fulfillment

of the requirements for the degree of Doctor of Philosophy

Department of Chemistry

Edmonton, Alberta

Spring 2006

Canada

To Monireh and Moez

Abstract

To understand the origin of the differential reactivity of nucleobases in oligodeoxynucleotides (ODNs), the loss of neutral nucleobases from a series of deprotonated thymine-rich ODN 10-, 15- and 20-mers, XT_9, T_9X, T_5XT_4, XT_{14}, XT_{19} and $T_{19}X$, containing a single reactive base (X = adenine (A), guanine (G), cytosine (C)) were investigated. Time-resolved blackbody infrared radiative dissociation experiments, implemented with a Fourier transform ion cyclotron mass spectrometer (FT-ICR/MS) equipped with a nanoflow electrospray (nanoES) ion source, were used to evaluate the dissociation kinetics and energetics for the loss of a neutral nucleobase (XH). Over the temperature range investigated, the kinetics for the loss of CH was significantly slower than the loss of AH and GH. In contrast to loss of CH, the activation energies (E_a) for the loss of AH are sensitive to the length and charge state of the ODN and position of the base. Importantly, the trend in E_a values does not correlate with trends in deprotonation enthalpies or proton affinities of the nucleobases which indicates that the differences in energetics are not simply a result of differences in their gas phase acidity or basicity. Instead, the results suggest an inherent difference in the internal solvation of the reactive base, with A being significantly more solvated than C.

A novel temperature-controlled nanoES device which allows for determination of protein-ligand binding affinities (K_{assoc}) over a range of temperatures was developed. Values of K_{assoc} for carbohydrate complexes of two carbohydrate binding proteins were measured for solutions in the temperatures range of 5 - 40 °C. From the temperature dependence of MS-derived K_{assoc} values, the enthalpies and entropies of association were

determined. The thermochemical data were found to be in good agreement with values determined previously by isothermal titration calorimetry.

The influence of solution conditions (protein concentration, temperature, pH, and ionic strength) on stability of structurally similar B_5 homopentamers of Shiga toxins (Stx) 1 and 2 were investigated using temperature-controlled nanoES-FT-ICR/MS. At temperatures ranging from 0 to 60 °C, the Stx1 B subunit exists almost exclusively in its pentameric form at neutral pH. Acidification was found to promote disassembly. The Stx2 subunit forms abundant pentamers at subunit concentrations > 50 μM, neutral pH, ambient temperature and relatively high salt concentration. The lower thermodynamic stability of the B subunits of Stx2, compared with Stx1, is a significant finding because it may provide an explanation for the greater toxicity of Stx2 relative to Stx1.

Acknowledgements

I would like to express my sincere gratitude to my supervisor, Dr. John Klassen for his guidance, encouragement and inspiration throughout the course of my graduate study. I would also like to give special thanks to Dr. Elena Kitova for all her help in the laboratory and her thoughtful suggestions during my research work.

I would also like to thank the members of my research group, both past and present, for their help and more importantly for their friendship. I am grateful to Dr. Weijie Wang, Igor Sinelnikov, Jiangxiao Sun, and Glen Shoemaker for their fraternal support and encouragement over the period of my research work and building an enjoyable and friendly working environment.

My appreciation is also extended to Professor Paul Kebarle and Dr. Arthur Blades for our many interesting scientific conversations and sharing years of their experience with me.

A special thanks goes to Professor David Bundle for generously providing the carbohydrate compounds used in my research work.

Finally, my deepest gratitude goes to my parents, for their love, support and inspiration.

Table of Contents

Chapter 4   94

Determination of Protein-Ligand Association Thermochemistry Using
Variable-Temperature Nanoelectrospray Mass Spectrometry

Chapter 5 126

Stability of the Homopentameric B Subunits of Shiga Toxins 1 and 2 in Solution as Revealed by NanoES-FT-ICR/MS

List of Tables

List of Figures

$(T_9G)^{-2}$ (134 °C, 55 s), (g) $(CT_9)^{-2}$ (191.1 °C, 50 s),

(h) $(T_5CT_4)^{-2}$ (185.4 °C, 600 s), (i) $(T_9C)^{-2}$ (192.6 °C,

250 s).

thermocouples and Cu liner is also 1 cm. To satisfy the gas intake
requirement of the ion source, a portion of the regulated air (~700
mL/min) is introduced into the chamber through the Plexiglas disc.
The total volume inside the chamber is approximately 60 mL.   101

Figure 4.3   Temperature recorded at the nanoES tip, TC_1, versus the
temperatures at the two ends of the chamber, TC_2 ($\square$) and
TC_3 ($\circ$), over the temperature range of this study 5-40 °C.   102

Figure 4.4   NanoES mass spectra obtained in positive mode for an
aqueous solution of scFv (4 µM) and 1 (7 µM) with 6 mM
CH_3COONH_4 at (a) 15 °C, (b) 25 °C, (c) 35 °C.   110

Figure 4.5   Temperature dependence of K_{assoc} for the reaction,
scFv + 1 $\leftrightarrow$ scFv•1, determined by nanoES/MS ($\bullet$), and
the reaction IgG + 1 $\leftrightarrow$ IgG•1, determined by ITC ($\circ$),
ref 40. The dashed line corresponds to the nonlinear fit of
the vant't Hoff equation (eq 4.7) to the MS-derived values
of K_{assoc}. The error bars correspond to one standard deviation.   111

Figure 4.6   Van't Hoff plots, constructed from K_{assoc} values measured
by nanoES-MS, for the formation of the complexes: scFv•L,
where L = 2 ($\blacktriangle$), 3 ($\circ$), 4 ($\square$), 5 ($\blacklozenge$) and B_5•6 ($\bullet$). Each value
of K_{assoc} corresponds to the average of four measurements. The
solid lines correspond to the non-linear fit (eq 4.7) of the
experimental K_{assoc} values for each complex.   112

Figure 4.7   NanoES mass spectra obtained for an aqueous solution of
Stx1 B_5 (22 µM), P^k (46 µM) and CH_3COONH_4 (9 mM) at

List of Abbreviations

AFM	Atomic force microscopy
BIRD	Blackbody infrared radiative dissociation
CD	Circular dichroism
CID	Collision induced dissociation
DSC	Differential scanning calorimetry
ECD	Electron capture dissociation
EDTA	Ethylenediaminetetraacetic acid
ES	Electrospray
FAC/MS	Frontal affinity chromatography-mass spectrometry
FT-ICR/MS	Fourier transform ion cyclotron resonance mass spectrometry
IRMPD	Infrared multiphoton dissociation
ITC	Isothermal titration calorimetry
MALDI	Matrix-assisted laser desorption ionization
MS	Mass spectrometry
m/z	Mass-to-charge ratio
nanoES	Nanoflow electrospray
NMR	Nuclear magnetic resonance
ODN	Oligodeoxynucleotide
PA	Proton affinity
REX	Rapid energy exchange
rf	Radio frequency
scFv	Single chain variable domain fragment

SEM	Scanning electron microscopy
S/N	Signal-to-noise ratio
SPR	Surface plasmon resonance
Stx	Shiga toxin
TOF	Time of flight

Chapter 1

Study of Biomolecules and Biomolecular Complexes by

Mass Spectrometry

1.1   Introduction

Noncovalent macromolecular interaction is a common mechanism responsible for functioning of numerous processes in a cell. Protein complex formations are crucial for regulatory processes, including signal transduction [1-3], antigen-antibody interaction [4, 5], and formation of intracellular structures [6]. Biological function of a protein or protein complexes is directly related to the structure. However, the structure of a biomolecular complex is mediated by inter- or intra-molecular interactions between complex components or with other biomolecules present in the living cell. The function of a biological system is also defined by the energetics of these changes in molecular interactions through the biological process. Hence, a combination of the structure and energetics make it possible to acquire a more complete description of the biological processes in the molecular level [7, 8].

Due to complexity of biological systems, several different approaches have been used to understand and characterize macromolecular interactions, mapping functional epitopes of protein, and elucidation of higher order structures of a biopolymer and its noncovalent complexes. Optical spectroscopy (e.g. UV absorption, fluorescence, circular dichroism (CD) and light scattering), surface plasmon resonance (SPR), isothermal titration microcalorimetry (ITC), differential scanning calorimetry (DSC), nuclear

magnetic resonance (NMR), and X-ray crystallography are among the widely used techniques [9].

The application of mass spectrometry (MS) to study biological molecules, such as oligonucleotides, oligosaccharides, peptides, and proteins, and their noncovalent complexes has grown dramatically in recent years, due in large part to the advent of soft ionization techniques, in particular, matrix-assisted laser desorption/ionization (MALDI) [10], electrospray ionization (ES) [11-13] and, more recently, desorption electrospray ionization (DESI) [14]. These ionization methods allow for the transfer of intact nonvolatile macromolecules from condensed phase to the gas phase in an ionized form. Arguably, the greatest impact in the field of MS has been the introduction of ES and the low flow version, nanoflow electrospray ionization (nanoES), *vide infra*. ES and nanoES are able to transfer intact noncovalent biomolecular complexes from solution to the gas phase. Thus, it becomes possible to study noncovalent biomolecular complexes by using ES/MS [15, 16]. The study of noncovalent complexes by MS can also benefit of speed and sensitivity, two major advantageous of MS-based methods. There are reports of study of noncovalently bound complexes using ES/MS with amounts as low as subpicomole of analyte for such experiments [16]. Meanwhile, the introduction of the nanoES has offered an enhancement in mass range detection limit of MS-based methods [17, 18]. Taking advantage of its ability to perform simultaneous measurements on mixtures of analytes, ES/MS is an extremely useful tool for screening possible drug targets from combinatorial libraries in a rapid, accurate, and sensitive manner [19, 20]. In such experiments, a protein is introduced to a library of ligands. Protein will attach to ligands with appropriate binding characteristics. In addition, the stoichiometry of a complex can be deduced

2

directly from the molecular mass measurement of the complex, obtained from resulting mass spectrum. Furthermore, the relative [21] and absolute binding affinities [22] of the complexes can be evaluated from relative ion abundances observed in the mass spectra. A detailed overview of the observation of noncovalent bimolecular complexes by ES/MS has appeared in several review articles [16, 23].

Nonenzymatic gas phase sequencing (primary structure) of proteins, peptides, oligosaccharides and oligodeoxynucleotides (ODNs) can be performed by direct sampling of ions and carrying out unimolecular dissociation reactions using ES and tandem mass spectrometry (MS^n). MS^n experiments can be performed based on different techniques, such as collision-induced dissociation (CID) [24], blackbody infrared dissociation (BIRD) [25-28], electron capture dissociation (ECD) [29-31], or multiphoton dissociation (IRMPD) [32]. Sequence information is extracted from the mass differences of the sequential fragment ions of the same general structure [33, 34]. The high mass resolution and mass accuracy with ion manipulation capabilities of Fourier transform ion cyclotron resonance (FT-ICR) mass spectrometer make it a prime candidate to characterize biopolymers [35]. ES and nanoES are also providing MS with new capabilities to probe higher order structures of large biomolecules and noncovalent complexes in the gas phase. Ion-ion [36] and ion-molecule reactions [37, 38] benefit from multiply charged ions produced by ES and nanoES. Ion-molecule reactions of multiply protonated proteins and protein-ligand complexes with deuterating agent, *i.e.* hydrogen-deuterium (H/D) reaction, have been used to qualitatively probe gas phase structure [39, 40]. There is evidence that proteins and protein-ligand complexes transferred from solution to the gas phase using gentle ES process may retain aspects of higher order

3

solution structure [21c, 41]. Meanwhile, H/D exchange reactions have also been reported for negatively charged oligonucleotide ions [42-44].

1.2 Mass Spectrometry

Mass spectrometric analyses involve the formation of gas phase ions by ionization methods and detection of the mass-to-charge ratio (m/z) of these ions by mass analyzers. The choice of ionization method depends on the nature of the sample and the type of information sought. Electron impact ionization and chemical ionization are used for volatile, low mass molecules. For nonvolatile sample molecules, other ionization methods have been used. Desorption ionization methods for nonvolatile samples with medium to high mass molecules include secondary ion mass spectrometry and fast atom bombardment for analytes soluble in a liquid, and MALDI in.which analytes are co-crystallized with a chemical matrix. Atmospheric pressure ionization methods, include ES and nanoES are also used for nonvolatile samples.

There are a number of different types of mass analyzers. These include magnetic sector [45], quadrupole [46], ion trap [47], time of flight (TOF) [48], FT-ICR [49] and, more recently, orbitrap [50]. They are very different in design and performance, each with its own strength and weakness. High mass resolution and high mass detection of TOF and FT-ICR have been used to determine the stoichiometry of macromolecular complexes even for small molecules (*e.g.* drug molecules) bound to larger molecular mass targets. MALDI is usually coupled to TOF analyzers that measure the mass of intact peptides, whereas ES has mostly been coupled to ion trap, triple quadrupole, and FT-ICR analyzers, and used to generate fragment ion spectra (CID spectra) of selected precursor

4

ions [51]. The versatility of MS techniques is continuously enhanced through the combination of multiple mass analyzers [52, 53].

1.3   Electrospray Ionization

The mechanism of ES process, as described by Kebarle and Tang [54], involves the production of charged droplets from an electrolyte dissolved in a solvent; shrinkage of the droplets by solvent evaporation accompanied with droplet fissions, formation of very small, highly charged droplets from which gaseous ions are produced.

Shown in Figure 1.1 [54] is a diagram describing the ES process. The high positive voltage applied to the capillary induces charge separation of electrolytes in solution, positive charges drift towards the liquid surface leading to the formation of a liquid cone referred to as a Taylor cone. At a sufficiently high electric field, the liquid cone becomes unstable and emits a thin liquid filament which subsequently breaks up into small positively charged droplets. With solvent evaporation, these droplets start to shrink into the smaller droplets. As the charge density on the droplet surface increases to the Rayleigh limit (the point at which the Coulombic repulsion of the surface charges is equal to the surface tension of the droplets), these droplets undergo Rayleigh fission, eventually forming small highly charged offspring droplets. Production of gas phase ions from small droplets follows one of two mechanisms: the ion evaporation model and the charge residue model. The ion evaporation model, proposed by Iribarne and Thomson [55, 56] assumes ion emission directly from very small and highly charged droplets. This model accounts for the production of gas phase ions of small molecules. In the charge residue model, proposed by Dole [57], the droplets undergo many fissions, finally

5
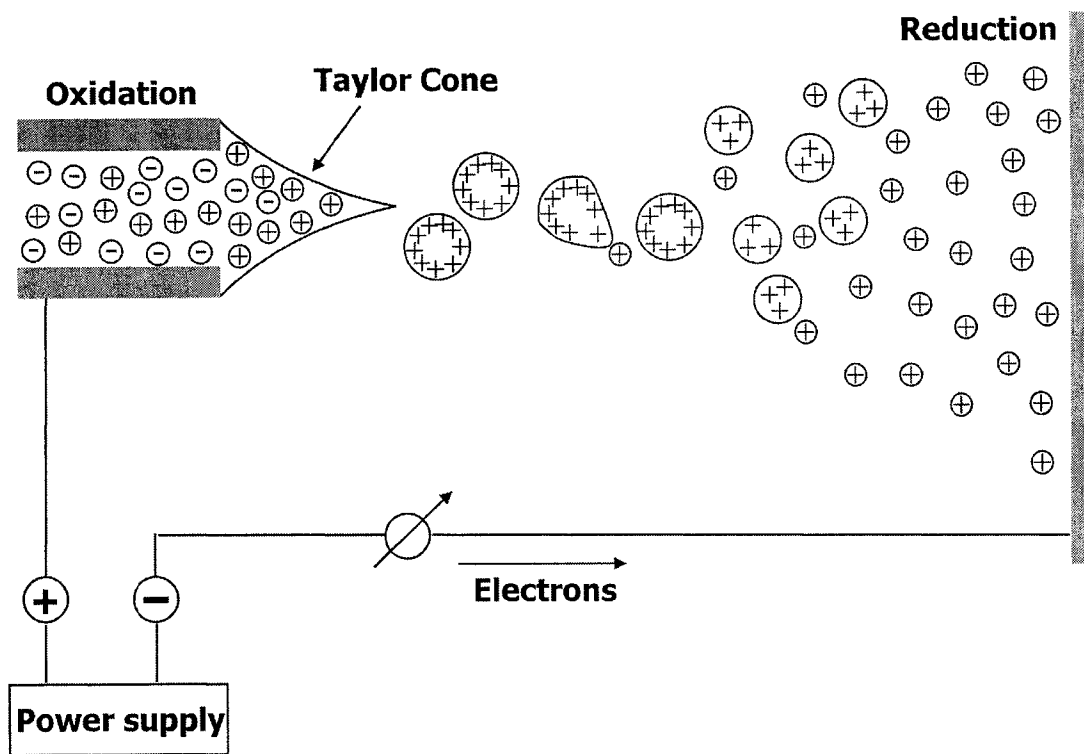
Figure 1.1 Illustration of the ES process.

producing droplets containing a few analyte molecules which, by further solvent evaporation, results in gaseous ions. This model is believed to be most significant for macromolecules.

According to the ES process described above, the question of whether the solution binding is preserved following ES conversion to the gas phase is raised. To better understand this, several issues should be considered. First, during ion separation in solution, electrochemical reactions (*i.e.* solvent oxidation, emitter electrode corrosion and analyte oxidation) occur at the electrode in the ES tip to supply excess charges required to maintain the productions of charged droplets. As a result, the composition (pH, metal ion concentration and analyte charge state) of the initial solution may be altered during the course of sampling. It has been reported by Van Berkel and coworkers [58, 59] that the degree of alteration of solution composition by electrochemical reactions depends on the experimental conditions (solvent, ES currents, flow rates, electrode materials, *etc.*) and analyte properties (pK_a, metal-binding affinity, equilibrium redox potential, *etc.*). Since most biocomplexes are sensitive to the solution pH, one should be aware of the influence of electrochemical reactions occurring during the ES processes, *e.g.* oxidation of water solvent in aqueous solutions (eq 1.1).

$$2H_2O \leftrightarrow O_2 + 4H^+ + 4e^- \tag{1.1}$$

The second factor to be considered is whether the distribution of species at equilibrium in solution could be perturbed in the ES droplets due to the increasing ionic strength and analyte concentration during the solvent evaporation. A comparison of the residence time of droplets in the ES source and the lifetime of the complexes, determined by the kinetics of association/dissociation reactions, provides useful information about the possibility of

an equilibrium shift during the ES process. However, due to the complexity of the ES process, estimates of droplet lifetimes are uncertain. Factors such as the size of droplets, fission events, solvent evaporation rates and temperatures of the droplets will influence the lifetime of droplets. In spite of these uncertainties, an insightful study on the complexation of strontium with EDTA by Wang *et al.* [60] has shown that a smaller than expected shift in the equilibrium distribution, based on the kinetics of reaction and the estimated time scale of the ES process. This study suggests that kinetically labile species could be monitored by ES. The third consideration is related to the issue of ionization efficiency. The binding affinity of complexes is evaluated from the relative abundances of ions corresponding to solution species observed in the mass spectra. Any difference in the ionization efficiency would lead to incorrect relative ion abundances in the mass spectra. The ionization efficiency is dependent on the chemical properties of analytes, solvents, charge agents, and droplet size. To eliminate the influence of ionization efficiency on the binding constant measurements, ions with similar ionization efficiencies are chosen to derive the binding constant. If this is not the case, the equilibrium concentration of each component in solution can be derived from the intensity of the corresponding ion in the mass spectra, based on a calibration plot of ion abundance as a function of solution concentration. This approach relies on the assumption that the ES response to a particular compound is dependent only on its concentration in solution and is not affected significantly by the presence of other species. This approach has been successfully applied to the determination of binding constants of vancomycin and ristocetin complexes with peptides [61]. The last consideration is the formation of complexes from random aggregation during the ES process. These artificial complexes,

8

which are commonly referred to as "nonspecific complexes", may be sufficiently long-lived in the gas phase to be detected. Their presence in the mass spectra may obscure the binding stoichiometry of specific complexes in solution. All these issues represent challenges in developing an ES-MS-based methodology for the characterization of solution phase noncovalent complexes.

Instead of conventional ES, the low solution flow version, nanoES, introduced by Wilm and Mann [17, 18], is used in the present work. The mechanism of nanoES is similar to that of ES. NanoES operates at lower solution flow rates, typically 10-50 nL/min and emits correspondingly smaller droplets than conventional ES. The low flow rate of nanoES was realized experimentally with nanoES tips pulled from glass capillaries to a fine tip with a diameter in the order of μm. In our laboratory, aluminosilicate glass capillaries, pulled with a laser micropipette puller to a very fine tip with an external diameter around 2-7 μm were used. The features of nanoES make it more convenient than conventional ES for investigating noncovalent complexes. Only picomoles or less of analyte per analysis are needed in using nanoES, a very important feature in the analysis of limited amounts of biosamples. NanoES, also, allows for.the transfer of noncovalent complexes from buffered aqueous solutions to the gas phase and, therefore, can be directly performed on the complex solution remained under near physiological conditions. The short lifetimes of the nanoES droplets, which are estimated to be tens of microseconds, are likely advantageous for preserving the original solution composition throughout the formation of gaseous ions.

9

1.4   FT-ICR/MS

To date, FT-ICR/MS exhibits the highest resolving power and mass accuracy with multiple capabilities for probing the structure of ions among mass spectrometry methods. The general principle of FTICR is described in detail in several review and tutorial articles [49, 62], and only a brief introduction is given here.

The basis for FT-ICR/MS is ion cyclotron motion, which arises from interaction of an ion, in a cyclotron cell (analyzer cell), with the spatially homogeneous static magnetic field. In this technique ionic mass to charge ratio, m/q, is converted to an experimentally measurable ion cyclotron motion. Figure 1.2 illustrates the cyclotron motion of a positive ion subjected to a static magnetic field, B, pointing into the plane of the paper. The cyclotron frequency, ω_c can be expressed as:

$$\omega_c = \frac{qB}{m} \tag{1.2}$$

where ω_c is the cyclotron frequency, q the charge of the ion ($q = ze$, where z and e are the charge and the elementary charge, respectively), B the magnetic strength and m the mass of the ion. To obtain the cyclotron frequency in Hertz (f) the results in radiation per second has to be divided by 2π ($\omega_c = 2\pi f$). Notably, equation 1.2 does not include the velocity of the ion, inferring that ions of one mass have the same cyclotron frequency, irrespective of their velocity. Therefore the ultra high resolution achievable by FT-ICR/MS is a direct result of insensitivity of cyclotron frequency to the kinetic energy of an ion. The radii of the trapped ions' cyclotron orbits in the analyzer cell are usually small compared with the dimensions of the cell. To detect the trapped ions in the cell, an rf pulse (sweep pulse) equal to the cyclotron (resonance) frequencies of the ions is

10

transmitted by the excitation plates, an opposing pair of plates which lie in parallel to the magnetic field, of the cell. Figure 1.3a shows the trajectory of a group of excited ions of the same mass to charge ratio at their cyclotron frequency. As the coherently orbiting excited ions passing another opposing pair of electrodes (detection plates), also parallel to the magnetic axis, they induce an alternating current to the plates called image current (Fig. 1.3b). The amplitude of the transient signal is proportional to the number of ions in the cell while its frequency is the same as cyclotron frequency of the ions. The transient signal is subsequently amplified, digitized and stored by computer for processing. To obtain a mass spectrum, Fourier transform is applied to time domain of the digitized and stored transient signal. Subsequently, the resultant frequency components of the signal (frequency domain) are converted into a mass spectrum using eq 1.2. A unique and notable feature of the FT-ICR is its non-destructive nature of the image current detection; ions remain in the cell after detection process. Improved sensitivity is a direct result of remeasurement and repetition of the excitation and detection cycles on trapped ions in FT-ICR/MS cell.

Shown in Figure 1.4 is a schematic diagram of the nanoES-FT-ICR/MS used in the present work. Gaseous ions are produced by nanoES performed on aqueous solutions containing analyte molecule. The electric field required to spray the solution is established by applying a voltage (±800 - ±1000) to a platinum wire inserted inside the glass tip. Droplets and gaseous ions produced by nanoES are sampled into the mass spectrometer through a heated metal capillary. Gaseous ions are transmitted through the skimmer and accumulated in the hexapole for a certain time to enhance signal-to-noise (S/N) ratio. The accumulated ions are ejected from the hexapole and accelerated (±2700

11

V) into a 4.7 T superconducting magnet, decelerated, and eventually trapped by a combination of electric and magnetic field in FT-ICR cell for detection. The typical base pressure for the instrument is ~5 x 10^{-10} mbar, maintained by the differential pumping system.

To perform time-resolved dissociation experiments on the ions of interest, the ions are isolated using a single rf frequency and broadband rf sweep excitation. The isolated ions are stored inside the cyclotron cell for variable reaction times prior to excitation and detection. During the reaction time, stored ions undergo the dissociation by a variety of dissociation techniques, such as CID, IRMPD, ECD, and BIRD. The principle of the BIRD, the technique used in the present work, will be described in the following section.

12
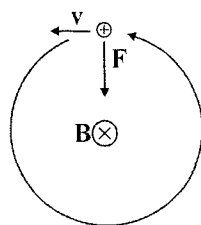
Figure 1.2 Cyclotron motion of a positive ion of charge q moving at velocity $\mathbf{v}$ in the presence of constant magnetic field, $\mathbf{B}$. The magnetic field is pointing into the plane of the page. The ion moving to the left experiences a downward force, $\mathbf{F} = q(\mathbf{v} \times \mathbf{B})$, that drives it into counterclockwise orbit.

$$\omega_c = \frac{qB}{m}$$

$$q = ze$$
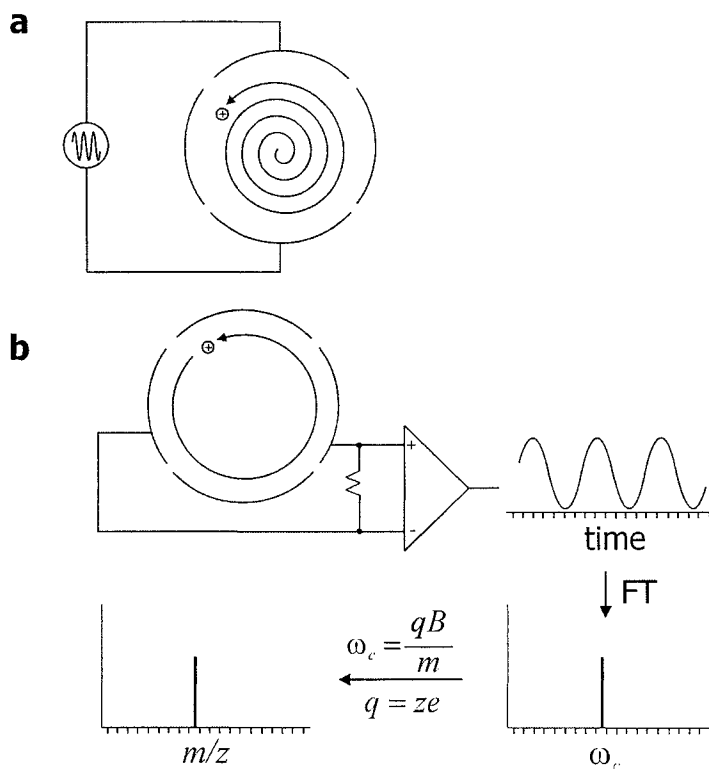
Figure 1.3 Illustration of excitation and image current detection for mass analyzing ions in a FT-ICR/MS analyzer cell (a) ion excitation, (b) ion image current detection, time domain transient and its corresponding spectrum produced by performing a Fourier transform.

13
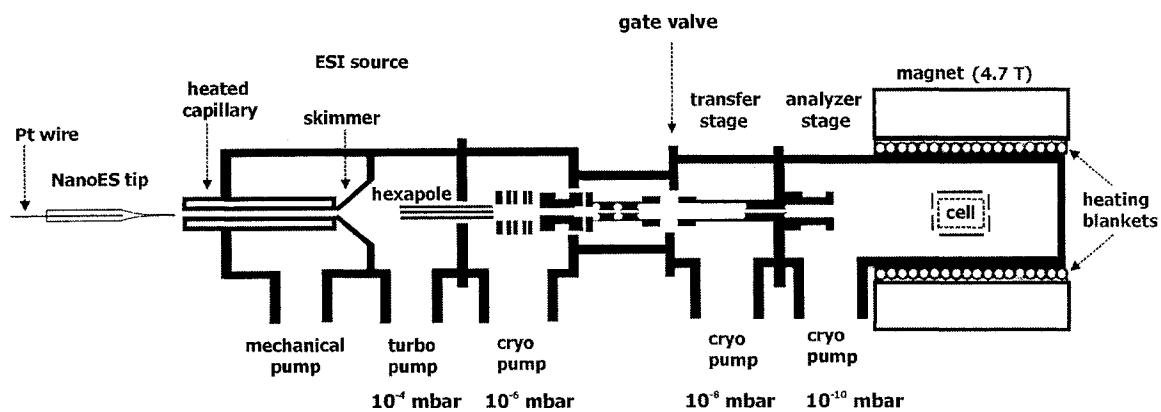
Figure 1.4 NanoES-FT-ICR/MS instrument diagram.

14

1.5 Blackbody Infrared Radiative Dissociation (BIRD)

BIRD is a dissociation technique which allows ions to undergo unimolecular dissociation reactions at essentially zero pressure by the exchange of energy with ambient blackbody radiation field. Consequently, BIRD experiments can be performed in ultra low pressure heated cyclotron cell of the FT-ICR/MS.

Molecular activation by blackbody photons, was originally suggested by Perrin [63]. The unimolecular dissociation reaction of a hypothetical molecular ion, AB^+, can be envisioned as a two step mechanism (eq 1.3a-c) [25-28]. First step involves excitation of AB^+ to activated species, AB^{+*}, by the absorption of infrared photons, eq 1.3b. Activated species could relax back into AB^+ through the emission of infrared photons, or dissociate into products, A^+ and B (eq 1.3c). Under steady state conditions, the observed collisionless unimolecular rate constant, k_{uni}, is expressed in terms of radiative activation and deactivation rate constants, $k_{1,rad}$ and $k_{-1,rad}$, and unimolecular dissociation rate constant, k_d, eq 1.4a. If k_d is much larger than $k_{-1,rad}$, the observed reaction kinetic, k_{uni}, reflects only the rate of photon absorption, $k_{1,rad}$, eq 1.4b. Therefore, no information about the dynamics of the dissociation process is obtained. If k_d is much smaller than $k_{-1,rad}$, k_{uni} is determined by the dissociation kinetics of ions with a Boltzmann distribution of internal energies (eq 1.4c) [27]. From the temperature dependence of the unimolecular rate constants for dissociation, k_{uni}, Arrhenius activation energy (E_a) and preexponential factor (A) can be determined. This is the case for large ions such as protein ions which are in the rapid energy exchange limit (REX) [27]. In this limit, the unimolecular dissociation rate of the activated ions is slow compared with the rate of energy equilibration of a

15

molecule with the surroundings by photon exchange, and the internal energy of a population of ions is given by a Boltzmann distribution.

$$AB^+ \xrightarrow{\ k_{uni}\ } A^+ + B \tag{1.3a}$$

$$AB^+ + h\nu \underset{k_{-1,rad}}{\overset{k_{1,rad}}{\longleftrightarrow}} AB^{+*} \tag{1.3b}$$

$$AB^{+*} \xrightarrow{\ k_d\ } A^+ + B \tag{1.3c}$$

$$k_{uni} = k_d \left(\frac{k_{1,rad}}{k_{-1,rad} + k_d} \right) \tag{1.4a}$$

$$k_{uni} = k_{1,\,rad} \quad \text{if } k_d \gg k_{-1,\,rad} \tag{1.4b}$$

$$k_{uni} = k_d \left(\frac{k_{1,rad}}{k_{-1,rad}} \right) \quad \text{if } k_d \ll k_{-1,\,rad} \tag{1.4c}$$

The observation of ion-dissociation reactions using BIRD technique is based on two essential requirements. First, BIRD experiments should be performed at a low pressure (below 10^{-6} Torr). At this low pressure, infrared photon absorption and emission exchange between ions and their surroundings are the dominant phenomena compared with negligible collisional energy exchange. Second, the time scale of observation of the dissociating molecules should be long enough (on the order of seconds) to give a significant degree of dissociation of the population for this relatively slow mechanism [28].

1.6 The Present Work

Despite widespread application of MS-based techniques for sequencing biopolymers, fundamental questions regarding the gas phase dissociation mechanisms remain. Understanding the mechanism allows planning of experiments and making

16

rational choices of experimental parameters leading to a desired result. In the case of oligonucleotides (ODNs), a number of mechanisms have been proposed to account for the loss of neutral nucleobases from single strand ODNs. To date, most dissociation energetic data available for the loss of nucleobases from ODN anions have been inferred from trends in dissociation kinetics, normally established from CID experiments. However, trends in dissociation kinetics are generally not reliable indicators of the relative dissociation energetics, particularly when the internal energy distribution of the reactant ions is unknown, as is typically the case in CID experiments. Part of the present work is focused on the study of the origin of differential reactivity of the nucleobases and the influence of charge state, length, and position on the loss of neutral nucleobase and dissociation energetics from a series of single strand ODNs.

In Chapter 2, Arrhenius activation parameters, activation energy (E_a) and preexponential factor (A), for the loss of neutral nucleobase from a series of doubly deprotonated oligodexoynucleotide 10-mers of the type XT_9, T_9X and T_5XT_4, where X= A, C and G, have been determined using time-resolved BIRD experiments. At temperatures of 120 to 190 °C, the anions dissociate exclusively by the loss of a neutral nucleobase (XH), followed by cleavage of the sugar $3'$ C-O bond leading to (a – XH) and w type ions or, in the case of the T_9X^{-2} ions, the loss of H_2O. The dissociation kinetics and energetics are sensitive to the nature and position of X. Over the temperature range investigated, the kinetics for the loss of AH and GH were similar, but ~100 times faster than for the loss of CH. For the loss of AH and GH, the values of E_a are sensitive to the position of the base. The order of the E_a's for the loss of XH from the $5'$ and $3'$ termini is: C > G > A; while for T_5XT_4 the order is: C > A > G. The trends in the values of E_a do

17

not parallel the trend in deprotonation enthalpies or proton affinities of the nucleobases in the gas phase, indicating that the energetic differences do not simply reflect differences in their gas phase acidity or basicity. The A-factors vary from 10^{10} to 10^{15} s^{-1}, depending on the nature and position of X. These results suggest that the reactivity of individual nucleobases is influenced by stabilizing intramolecular interactions.

To answer the question whether the trends in the dissociation E_a and $\Delta S^{\ddagger}$ values measured for the 10-mers are general, evaluation of Arrhenius parameters for the dissociation of larger T-rich ODN anions was undertaken. In Chapter 3, Arrhenius activation parameters for the loss of neutral nucleobases from a series of T-rich, doubly and triply deprotonated 15- and 20-mer oligonucleotides containing a single reactive base, XT_{14}, XT_{19} and $T_{19}X$, where X = A or C, have been determined using the BIRD technique. The A-containing anions are found to be significantly more reactive ($\geq$ 3000 times) than the C-containing ions over the temperature range investigated. Importantly, the Arrhenius parameters for the loss of AH exhibit a strong dependence on size of the ODN and, to some extent, the charge state; the Arrhenius parameters increase with size and charge (E_a = 29 - 39 kcal mol^{-1}, $A = 10^{15}$ - 10^{20} s^{-1}). In contrast, the parameters for the loss of CH are largely insensitive to size (E_a = 35 - 39 kcal mol^{-1}, $A = 10^{14}$ - 10^{17} s^{-1}). The results suggest an inherent difference in the internal solvation of the reactive base, with A being significantly more solvated than C in the 15- and 20-mers. To further probe differences in internal solvation of A and C, hydrogen/deuterium (H/D) exchange was carried out on AT_{19}^{-3}, $T_{19}A^{-3}$, CT_{19}^{-3} and $T_{19}C^{-3}$ using D_2O as the exchange reagent. The relative extent of exchange was found to be sensitive to the sequence of the ODNs. However, the H/D exchange results did not, by themselves, suggest differences in

18

internal solvation within the ODN anions. Arrhenius parameters for the dissociation of noncovalent complexes of T_{20}^{-3} and the neutral nucleobase AH or CH have also been determined. Differences in the parameters indicate differences in the nature of the intermolecular interactions. It is proposed that neutral A-T interactions (*i.e.* base-base), which originate in solution, dominate in the case of $(T_{20} + AH)^{-3}$, while charge solvation, involving CH and a deprotonated phosphate group, is present for $(T_{20} + CH)^{-3}$.

Meanwhile, one of the fast growing applications of the ES/MS is the study of noncovalent biological complexes. ES/MS has been increasingly used in quantifying the noncovalent interactions. In the remaining parts of the present work, we examine a relatively new application of nanoES-MS; the study of the influence of temperature on association of noncovalent biological complexes [15, 64, 65] and stability of multiproteins assemblies. In Chapter 4, we describe a temperature-controlled nanoES device which was applied to a series of protein-carbohydrate complexes. We show, for the first time, that variable-temperature nanoES-MS can provide accurate protein-ligand binding affinities (K_{assoc}) over a range of solution temperatures. We further demonstrate that the thermodynamic parameters for association, ΔH_{assoc} and ΔS_{assoc}, can be evaluated from the MS-derived K_{assoc} values. From the temperature dependence of K_{assoc}, values of ΔH_{assoc} and ΔS_{assoc} were determined and compared to values obtained by ITC technique. In addition, the application of temperature-controlled device in competitive binding experiments, wherein binding affinities of several carbohydrate ligands were determined simultaneously, is also described.

In Chapter 5, the influence of temperature on the structure and stability of two related complexes in solution are examined using variable-temperature nanoES-MS. The

19

assembly of the B subunits of Shiga toxins (Stx) 1 and 2 and the influence of solution conditions (protein concentration, temperature, pH and ionic strength) on it are investigated using temperature-controlled nanoES-FT-ICR/MS. Despite the similar higher order structure predicted by X-ray crystallography analysis, the B_5 homopentamers of Stx1 and Stx2 exhibit differences in stability under the solution conditions investigated. At solution temperatures ranging from 0 to 60 °C and subunit concentrations ranging from 5 to 85 μM, the Stx1 B subunit exists almost entirely as the homopentamer in aqueous solutions, independent of the ionic strength. In contrast, the degree of assembly of Stx2 B subunit is strongly dependent on temperature, subunit concentration and ionic strength. At subunit concentrations > 50 μM, the Stx2 B subunit exists predominantly as a pentamer, although smaller multimers (dimer, trimer and tetramer) are also evident. At lower concentrations, the Stx2 B subunit exists predominantly as monomer and dimer. The relative abundance of multimeric species of the Stx2 B subunit was insensitive to the ion source conditions, suggesting that gas phase dissociation of the pentamer ions in the source does not influence the mass spectrum. Blackbody infrared radiative dissociation of the protonated B_5 ions of Stx2 at the +12 and +13 charge states proceeds, at reaction temperatures of 120 to 180 °C, predominantly by the ejection of a single subunit from the complex. Dissociation into dimer and trimer ions constitutes a minor pathway. It follows that the dimer and trimer ions and, likely, the monomer ions observed in the nanoES mass spectra of Stx2 B subunit originated in solution and not from gas phase reactions. It is concluded that, under the solution conditions investigated, the homopentamer of Stx2 B subunit is thermodynamically less stable than that of Stx1 B subunit.

20

1.7 Literature Cited

(1)   Eyster K. M. *Biochem. Pharmac.* **1998**, *55*, 1927-1938.

(2)   Klemm J. D.; Schreiber S. L.; Crabtree G. R. *A. Rev. Immunol.* **1998**, *16*, 569-592.

(3)   Souroujon, M. C.; Mochly-Rosen D. *Nat. Biotechnol.* **1998**, *16*, 919-924.

(4)   Salzmann, M.; Bachmann, M. F. *Mol. Immunol.* **1998**, *35*, 271-277.

(5)   Dall'Acqua, W.; Goldman, E. R.; Lin, W.; Teng, C.; Tsuchiya, D.; Li, H.; Ysern, X.; Smith-Gill, S. J.; Mariuzza, R. A. *Biochemsitry* **1998**, *37*, 7981-7991.

(6)   Herrmann, H.; Aebi, U. *Curr. Opin. Struct. Biol.* **1998**, *8*, 177-185.

(7)   Ackers, G. K.; Doyle, M. L.; Myers, D.; Daugherty, M. A. *Science* **1992**, *255*, 54-63.

(8)   Koblan, K. S.; Ackers, G. K. *Biochemistry* **1992**, *31*, 57-65.

(9)   (a) Su, T. M.; Yang, Y. S. *Biochemistry* **2003**, *42*, 6863-6870; (b) Pletneva, E. V.; Laederach, A. T.; Fulton, D. B.; Kostic, N. M. *J. Am. Chem. Soc.* **2001**, *26*, 6232-6245; (c) Zuiderweg, E. R. P. *Biochemistry* **2002**, *41*, 1-7; (d) Pickford, A. R.; Campbell, I. D. *Chem. Rev.* **2004**, *104*, 3557-3565; (e) Coille, I.; Gauglitz, G.; Hoebeke, J. *Anal. Bioanal. Chem.* **2002**, *372*, 293-300; (f) Madrid, K. P.; De Crescenzo, G.; Wang, S. W.; Jardim, A. *Mol. Cell. Biol.* **2004**, *24*, 7331-7344; (g) O'Shannessy, D. J. *Curr. Opin. Biotechnol.* **1994**, *5*, 65-71; (h) Malmqvist, M. *Curr. Opin. Immunol.* **1993**, *5*, 282-286; (i) O'Shannessy, D. J.; Brigham-Burke, M.; Soneson, K. K.; Hensley, P.; Brooks, I. *Anal. Biochem.* **1993**, *212*, 457-468; (j) Murphy, K. P.; Freire, E.; Paterson, Y. *Proteins* **1995**, *21* 83-90; (k) Brandts, J. F.; Lin, L. N. *Biochemistry* **1990**, *29*, 6927–6940; (l) Otto-Bruc, A.; Antonny, B.; Vuong, T. M.; Chardin, P.; Chambre, M. *Biochemistry* **1993**, *32*, 8636-8645; (m)

Wensel, T. G.; Stryer, L. *Biochemistry* **1990**, *29*, 2155-2161; (n) Formisano, S.; Johnson, M. L.; Edelhoch, H. *Proc. Natl. Acad. Sci. U.S.A.* **1977**, *74*, 3340-3344; (o) Formisano, S.; Johnson, M. L.; Edelhoch, H. *Biochemistry* **1978**, *17*, 1468-1473; (p) Lu, H. S.; Ratzkin, B. *J. Biol. Chem.* **1995**, *270*, 4784-4791.

(10)   Hillenkamp, F.; Karas, M.; Beavis, R. C.; Chait, B. T. *Anal. Chem.* **1991**, *63*, 1193A-1203A.

(11)   Yamashita, M.; Fenn, J. B. *J. Phys. Chem.* **1984**, *88*, 4451-4459.

(12)   Yamashita, M.; Fenn, J. B. *J. Phys. Chem.* **1984**, *88*, 4671-4675.

(13)   Fenn, J. B.; Mann, M.; Meng, C. K.; Wong, S. F.; Whitehouse, C. M. *Science* **1989**, *246*, 64-71.

(14)   Takats, Z.; wiseman, J. M.; Gologan, B.; Cooks, R. G. *Science* **2004**, *306*, 471-473.

(15)   Ogorzalek Loo , R. R.; Goodlett, D. R.; Smith, R. D.; Loo, J. A. *J. Am. Chem. Soc.* **1993**, *115*, 4391-4392.

(16)   Loo, J. A. *Mass Spectrom. Rev.* **1997**, *16*, 1-23.

(17)   Wilm, M. S.; Mann, M. *Int. J. Mass Spectrom. Ion Processes* **1994**, *136*, 167-180.

(18)   Wilm, M. S.; Mann, M. *Anal. Chem.* **1996**, *68*, 1-8.

(19)   Gao, J.; Cheng, X.; Chen, R.; Sigal, G. B.; Bruce, J. E.; Schwartz, B. L.; Hofstadler, S. A.; Anderson, G. A.; Smith, R. D.; Whitesides, G. M. *J. Med. Chem.* **1996**, *39*, 1949-1955.

(20)   Wigger, M.; Eyler, J. R.; Benner, S. A.; Li, W. Q.; Marshall, A. G. *J. Am. Soc. Mass Spectrom.* **2002**, *13*, 1162-1169.

(21) (a) Cheng, X.; Chen, R.; Bruce, J. E.; Schwartz, B. L.; Anderson, G. A.; Hofstadler, S. A.; Gale, D. C.; Smith, R. D.; Gao, J.; Sigal, G. B.; Mammen, M.; Whitesides, G. M. *J. Am. Chem. Soc.* **1995**, *117*, 8859-8860; (b) Loo, J. A.; Holler, T. P.; Foltin, S. K.; McConnell, P.; Banotai, C. A.; Horne, N. M.; Mueller, W. T.; Stevenson, T. I.; Mack, D. P. *Proteins: Struct. Funct. Genet.* Suppl **1998**, *2*, 28-37; (c) Rostom, A. A.; Tame, J. R. H.; Ladbury, J. E.; Robinson. C. V. *J. Mol. Biol.* **2000**, *296*, 269-279; (d) Hill, T. J.; Lafitte, D.; Wallace, J. I.; Cooper, H. J.; Tsvetkov, P. O.; Derrick, P. J. *Biochemistry* **2000**, *39*, 7284-7290.

(22) (a) Greig, M. J.; Gaus, H; Cummins, L. L; Sasmor, H.; Griffey, R. H. *J. Am. Chem. Soc.* **1995**, *117*, 10765-10766; (b) Loo, J. A.; Hu, P.; McConnell, P.; Mueller, W. T.; Sawyer, T. K.; Thanabal, V. *J. Am. Soc. Mass Spectrom.* **1997**, *8*, 234-243; (c) Ayed, A; Krutchinsky, A. N.; Ens, W.; Standing, K. G.; Duckworth, H. W. *Rapid Commun. Mass Spectrom.* **1998**, *12*, 339-344; (d) Sannes-Lowery, K. A.; Griffey, R. H.; Hofstadler, S. A. *Anal. Biochem.* **2000**, *280*, 264-271; (e) Kitova, E. N.; Kitova, P. I.; Bundle, D. R.; Klassen, J. S. *Glycobiology* **2001**, *11*, 605-611; (f) Wang, W.; Kitova, E. N.; Klassen, J. S. *Anal. Chem.* **2003**, *75*, 4945-4955; (g) Zhang, S.; Van Pelt, C. K.; Wilson, D. B. *Anal. Chem.* **2003**, *75*, 3010-3018; (h) Hagan, N.; Fabris, D. *Biochemistry* **2003**, *42*, 10736-10745; (i) Tjernberg, A.; Carnö, S.; Oliv, F.; Benkestock, K.; Edlund, P.-O.; Griffiths, W. J.; Hallén, D. *Anal. Chem.* **2004**, *76*, 4325-4331.

(23) (a) Smith, R. D., Light-Wahl, K. J. *Biol. Mass Spectrom.* **1993**, *22*, 493-501; (b) Smith, R. D., Zhang, Z. *Mass Spectrom. Rev.* **1994**, *13*, 411-429; (c) Loo, J. A.

Bioconj. Chem. **1995**, *6*, 644-665; (d) Przybylski, M.; Glocker, M. O. *Angew. Chem. Int. Ed. Engl.* **1996**, *35*, 807-826.

(24) McLuckey, S. A. *J. Am. Soc. Mass Spectrom.* **1992**, *3*, 599-614.

(25) Tholmann, D.; Tonner, D. S.; McMahon, T. B. *J. Phys. Chem.* **1994**, *98*, 2002-2004.

(26) Price, W. D.; Schnier, P. D.; Jockusch, R. A.; Strittmatter, E. F.; Williams, E. R. *J. Am. Chem. Soc.* **1996**, *118*, 10640-10644.

(27) Price, W. D.; Williams, E. R. *J. Phys. Chem. A* **1997**, *101*, 8844-8852.

(28) Dunbar, R. C. *Mass Spectrom. Rev.* **2004**, *23*, 127-158.

(29) Zubarev, R. A.; Kelleher, N. L.; McLafferty, F. W. *J. Am. Chem. Soc.* **1998**, *120*, 3265-3266.

(30) Zubarev, R. A.; Kruger, N. A.; Fridriksson, E. K.; Lewis, M. A.; Horn, D. M.; Carpenter, B. K.; McLafferty, F. W. *J. Am. Chem. Soc.* **1999**, *121*, 2857-2862.

(31) Zubarev, R. A.; Horn, D. M.; Fridriksson, E. K.; Kelleher, N. L.; Kruger, N. A.; Lewis, M. A.; Carpenter, B. K.; McLafferty, F. W. *Anal. Chem.* **2000**, *72*, 563-573.

(32) Little, D. P.; Speir, J. P.; Senko, M. W.; O'Connor, P. B.; McLafferty, F. W. *Anal. Chem.* **1994**, *66*, 2809-2815.

(33) McLuckey, S. A.; Van Berkel, G. J.; Glish, G. L. *J. Am. Soc. Mass Spectrom.* **1992**, *3*, 60-70.

(34) Little, D. P.; Aaserud, D. J.; Valaskovic, G. A.; McLafferty, F. W. *J. Am. Chem. Soc.* **1996**, *118*, 9352-9359.

(35) Marshall, A. G. *Int. J. Mass Spectrom.* **2000**, *200*, 331-356.

(36) Pitteri, S. J.; McLuckey, S. A. *Mass Spectrom. Rev.* **2005**, *24*, 931-958.

(37) Blades, A. T.; Jayaweera, P.; Ikonomou, M. G.; Kebarle, P. *Int. J. Mass Spectrom. Ion Proc.* **1990**, *102*, 251-267.

(38) Ogorzalek Loo , R. R.; Loo, J. A.; Udseth, H. R.; Fulton, J. L.; Smith, R. D. *Rapid Commun. Mass Spectrom.* **1992**, *6*, 159-165.

(39) Winger, B. E.; Lightwahl, K. J.; Rockwood, A. L.; Smith, R. D. *J. Am. Chem. Soc.* **1992**, *114*, 5897-5898.

(40) Green, M. K.; Lebrilla, C. B. *Mass Spectrom. Rev.* **1997**, *16*, 53-71.

(41) Hunter, C. L.; Mauk, A. G.; Douglas, D. J. *Biochemistry* **1997**, *36*, 1018-1025.

(42) Felix, T.; Reyzer, M.; Brodbelt, J. *Int. J. Mass Spectrom.* **1999**, *190/191*, 161-170.

(43) Robinson, J. M.; Greig, M. J.; Griffey, R. H.; Mohan, V.; Laude, D. A. *Anal. Chem.* **1998**, *70*, 3566-3571.

(44) Hofstadler, S. A.; Sannes-Lowery, K. A.; Griffey, R. H. *J. Mass Spectrom.* **2000**, *35*, 62-70.

(45) Mattauch, J.; Herzog, R. *Z. Physik* **1934**, *89*, 786.

(46) Dawson, P. H. *Quadrupole Mass Spectrometry and its Applications*; Elsevier Scientific Publishing: New York, 1976.

(47) March, R. E. *J. Mass Spectrom.* **1997**, *32*, 351-369.

(48) Wiley, W. C.; McLaren, I. H. *Rev. Sci. Instrum.* **1955**, *26*, 1150-1157.

(49) Amster, I. J. *J. Mass Spectrom.* **1996**, *31*, 1325-1337.

(50) Hu, Q.; Noll, R. J.; Li, H.; Makarov, A.; Hardman, M.; Cooks, R. G. *J. Mass Spectrom.* **2005**, *40*, 430-443.

(51) Aebersold, R; Goodlett, D. R. *Chem. Rev.* **2001**, *101*, 269-295.

25

(52) de Hoffmann E. *J. Mass Spectrom.* **1996**, *31*, 129-137.

(53) Aebersold, R; Mann, M. *Nature* **2003**, *442*, 198-207.

(54) Kebarle, P.; Tang, L. *Anal. Chem.* **1993**, *65*, 972A-986A.

(55) Iribarne, J. V.; Thomson, B. A. *J. Chem. Phys.* **1976**, 64, 2287-2294.

(56) Thomson, B. A.; Iribarne, J. V. *J. Chem. Phys.* **1979**, 71, 4451-4463.

(57) Dole, M.; Mack, L. L.; Hines, R. L.; Mobley, R. C.; Ferguson, L. D.; Alice, M. B. *J. Chem. Phys.* **1968**, *49*, 2240-2249.

(58) de la Mora, J. F.; Van Berkel; G. J.; Enke, C. G.; Cole, R. B.; Martinez-Sanchez, M.; Fenn, J. B. *J. Mass Spectrom.* **2000**, *35*, 939-952.

(59) Van Berkel, G. J.; Asano, K. G.; Schnier, P. D. *J. Am. Soc. Mass Spectrom.* **2001**, *12*, 853-862.

(60) Wang, H.; Agnes, G. R. *Anal. Chem.* **1999**, *71*, 3785-3792.

(61) Lim, H.-K.; Hsieh, Y.; Ganem, B.; Henion, J. *J. Mass Spectrom.* **1995**, *30*, 708-714.

(62) (a) Marshall, A. G.; Grosshans, P. B. *Anal. Chem.* 1991, *63*, 215A-229A; (b) Buchanan, M. V.; Hettich, R. L. *Anal. Chem.* 1993, *65*, 245A-259A; (c) Marshall, A. G.; Shenheng Guan. *Rapid Commun. Mass spectrom.* 1996, *10*, 1819-1823; (d) Marshall, A. G.; Hendrickson, C. L. *Int. J. Mass Spectrom.* 2002, *215*, 59-75.

(63) Perrin, J. *Ann. Phys.* **1919**, *11*, 1-5.

(64) Benesch, J. L. P.; Sobott, F.; Robinson, C. V. *Anal. Chem.* **2003**, *75*, 2208-2214.

(65) Lentze, N.; Aquilina, J. A.; Lindbauer, M.; Robinson, C. V.; Narberhaus, F. *Eur. J. Biochem.* **2004**, *271*, 2494-2503.

Chapter 2

Arrhenius Activation Parameters for the Loss of Neutral Nucleobases

from Deprotonated Oligonucleotide Anions in the Gas Phase*

2.1   Introduction

Mass spectrometry (MS), combined with soft ionization techniques such as electrospray (ES) and matrix assisted laser desorption/ionization (MALDI), has become an indispensable tool for identifying the primary structure (sequence) of biopolymers: peptides, oligosaccharides and oligonucleotides. The mass spectrometry-based sequencing approach typically involves isolating the biopolymer ion of interest in the gas phase, dissociating it to produce sequence specific fragment ions and accurately determining the mass of the ions. Sequence information is extracted from the mass differences of the sequential fragment ions of the same general structure. The MS-based sequencing approach has many attractive features, most notably its inherent speed and sensitivity and its ability to sequence biopolymers containing unnatural or unusual modifications. Despite its widespread use in the sequencing of biopolymers, fundamental questions regarding the gas phase dissociation mechanisms remain. Elucidating these mechanisms is of practical importance, since it will facilitate the rational development of MS-based techniques for sequencing. In addition, the dissociation of biomolecules in the gas phase reflects their intrinsic properties, which are of fundamental interest.

* A version of this chapter has been published: Daneshfar, R.; Klassen J. S. *J. Am. Soc. Mass Spectrom.* **2004**, *15*, 55-64.

For oligodeoxynucleotides (ODNs), sequence information can be obtained from the fragmentation behavior of either the protonated or deprotonated gaseous ions and the dissociation behavior of both forms has been extensively investigated [1-10]. The dissociation of deprotonated ODNs, the focus of the present study, has been shown to proceed first by the loss of a nucleobase, adenine (A), guanine (G), cytosine (C) or thymine (T), in its neutral or deprotonated form, followed by fragmentation of the phosphoester bond at the deoxyribose 3' C-O bond at the site of base loss to produce (a-base) and w type ions, according to the nomenclature proposed by McLuckey and coworkers [7].

For ODN anions in low charge states, the nucleobases are lost in their neutral form. Interestingly, a survey of the literature reveals that the reactivity of the bases is highly variable and influenced by the sequence and charge state, and, seemingly, the activation technique. For example, Gross and coworkers examined the reactivity of the different bases in doubly deprotonated T-rich 8-mers using collision-induced dissociation (CID) implemented in an ion trap mass spectrometer (ITMS) [11]. The tendency to lose a given base and form the corresponding (a-base) ion was found to have the following order: $G > C \approx A \gg T$. A similar trend was observed by Smith and coworkers for the -2 and -3 charge states of a number of 12-mers [12]. However, in this same study the authors noted different trends at higher charge states: $A > C \approx G \gg T$ (-4); $A > C > G \gg T$ (-5). McLafferty and coworkers, using infrared multiphoton dissociation (IRMPD) and CID implemented with a Fourier-transform ion cyclotron resonance mass spectrometer (FT-ICR/MS), observed the following trend for large multiply deprotonated oligonucleotides (up to 100-mers): $A > C \approx G \gg T$ [9]. In contrast, McLuckey and

28

coworkers did not observe any preferential loss of the nucleobases in CID-ITMS experiments perform on small, but relatively highly charged, ODN anions (4-, 5- and 8-mers) [8].

At present, the origin of the differential reactivity of the nucleobases is not fully understood. A number of mechanisms have been proposed to account for the loss of a neutral base and subsequent backbone fragmentation and these have been summarized by Gross and coworkers [11, 13]. Briefly, the proposed mechanisms involve either the loss of the nucleobase in its deprotonated form, followed by proton abstraction from the ODN such that the base is ultimately lost as a neutral, or the loss of the nucleobase in its neutral form, which requires proton transfer either before or in concert with cleavage of the N-glycosidic linkage. It has been suggested that these two general mechanisms might be distinguished based on a correlation between the dissociation energetics of the different nucleobases and their proton affinity (PA), if the base is protonated prior to cleavage of the glycosidic bond [11, 13-15], or their gas phase deprotonation enthalpy (ΔH_{acid}) [2, 10, 16, 17], if the base is lost in its deprotonated form. To date, however, there are few energetic data available for the loss of nucleobases from ODN anions with which to compare the thermodynamic acid/base properties. Consequently, the relative dissociation energies have been inferred from trends in the dissociation kinetics, normally established from CID experiments. For example, Gross and coworkers have suggested that correlation of the reactivity of bases (determined by CID) and their PA's as evidence for a dissociation mechanism in which the nucleobase abstracts a proton prior to cleavage of the N-glycosidic bond [11]. However, trends in dissociation kinetics are generally not reliable indicators of the relative dissociation energetics, particularly when the internal

29

energy distribution of the reactant ions is unknown, as is typically the case in CID experiments.

The first quantitative study of the dissociation kinetics and energetics of deprotonated ODNs was performed by Williams and coworkers [16]. Using the blackbody infrared radiative dissociation (BIRD) technique and FT-ICR/MS, they determined Arrhenius activation parameters for the loss of neutral AH, CH and GH from a small number of doubly deprotonated 7-mers. However, all of the oligonucleotides investigated contained multiple reactive bases and the values of E_a reported in this work represent *average* values, reflecting base loss from multiple sites. These authors also reported that thymine was stable, independent of sequence, at temperatures up to 210 °C. Recently, Muddiman and coworkers used IRMPD experiments to investigate the *relative* energetics for the loss of neutral bases from some triply deprotonated 16-mers [18]. The relative energetics established for multiple reactive bases were in good agreement with the aforementioned BIRD study. The present work represents the first systematic study of the kinetics and energetics for the loss of neutral nucleobase from a series of doubly deprotonated T-rich ODN 10-mers, XT_9, T_9X and T_5XT_4, containing a single reactive base (X = A, C or G). Time-resolved BIRD experiments have been used to evaluate the dissociation kinetics for the loss of XH. From the temperature dependence of the dissociation rate constants, Arrhenius activation parameters have been determined. The trends in the kinetics and energetics for the loss of nucleobase are compared with trends reported in previous dissociation studies and discussed in terms of possible dissociation mechanisms and the presence of internal solvation of the reactive base.

30

2.2 Experimental

Mass spectra were obtained using an *ApexII* 47e Fourier-transform ion cyclotron resonance (FT-ICR) mass spectrometer (Bruker, Billerica, MA) equipped with a modified external nanoelectrospray (nanoES) ion source. The oligonucleotides were purchased from ACGT Corp. (Toronto, Canada) and used without further purification. The oligonucleotides were dissolved in 1:1 solutions of H_2O/CH_3CN at a concentration of 200 μM. NanoES tips were pulled from aluminosilicate tubes (1 mm o.d., 0.68 mm i.d.) using a P-97 micropipette puller (Sutter Instruments, Novato, CA). A platinum (Pt) wire, inserted into the open end of the nanoES tip, was used to apply an approximately –800 V potential to the nanoES solution. The tip was positioned 1-2 mm from a stainless steel sampling capillary using a microelectrode holder. The solution flow rate typically ranged from 60 to 100 nL/min, depending on the diameter of the nanoES tip (5 to 10 μm o.d.) and the electrospray voltage.

The droplets and gaseous ions produced by nanoES were introduced into the mass spectrometer through a heated stainless steel capillary (0.43 mm i.d.) maintained at a temperature (external) of approximately 66 °C. Ions were accumulated in the external hexapole for 3 s, subsequently ejected and injected at 2700 V into the bore of the 4.7 tesla superconducting magnet, decelerated and introduced into the ion cell. The temperature of the ion cell, which established the reaction temperature, was controlled by applying a voltage to the two external flexible heating blankets placed around the vacuum tube in the vicinity of the ion cell [19]. The heating blankets, 24 cm in length, were centered around the ion cell (6.5 cm in length). The presence of internal thermocouples in the vicinity of the ion cell resulted in a significant decrease in ion transmission and an increase in

31

electrical noise in the spectra. Therefore, in a separate experiment, the temperature inside the cell, measured by a thermocouple placed temporarily inside the cell, was calibrated against the temperature measured at several points on the outside of the vacuum tube. Because of the unavoidable contact between the end of the vacuum tube and the room temperature shield of the magnet, a temperature gradient existed across the vacuum tube between the cell and the end flange. To properly account for the gradient, the internal cell temperature was calibrated against eight thermocouples on the outside of the vacuum tube. Using this approach, calibration plots were generated for cell temperatures ranging from 25 to 175 °C. The plots were found to be linear, with the cell temperature 10 to 20 °C below that of the external temperature, depending on the external temperature. Mass spectra were acquired by an SGI R5000 computer running the Bruker Daltonics XMASS software, version 5.0. On average 10 scans, containing 128 K data points per scan, were acquired per spectrum.

2.3   Results and Discussion

2.3.1   Dissociation Pathways

NanoES of 1:1 $H_2O:CH_3CN$ solutions containing $\sim 10^{-4}$ M ODN (XT_9, T_5XT_4 or T_9X, where X= A, C or G) produced almost exclusively the doubly deprotonated ion $(M - 2H)^{-2}$ with small amounts of the Na^+ and K^+ adducts, see Figure 2.1. A small amount of the triply deprotonated $(M - 3H)^{-3}$ ion and the nonspecific dimer, $(2M - 3H)^{-3}$, were also frequently observed. BIRD was performed on the $(M - 2H)^{-2}$ ($\equiv M^{-2}$) ions at temperatures ranging from 120 to 190 °C. Representative BIRD spectra for each M^{-2} ion are shown in Figure 2.2. Dissociation of the $(XT_9)^{-2}$ and $(T_5XT_4)^{-2}$ ions, where X = A or

32

G, yielded product ions corresponding to the loss of neutral base, $(M - XH)^{-2}$, and cleavage of the sugar 3' C-O bond, leading to the w_9^{-2} ion for $(XT_9)^{-2}$ and the complementary $(a_6 - XH)^-$ and w_4^- ions for $(T_5XT_4)^{-2}$. Dissociation of the $(T_9X)^{-2}$ ions (X = A or G), resulted in the $(M - XH)^{-2}$ and $(M - XH - H_2O)^{-2}$ (structurally equivalent to $(a_{10} - XH)^{-2}$) ion. The same product ions were observed for the C-containing anions, with the exception of the $(M - XH)^{-2}$ ion, which is believed to have a short lifetime under the experimental conditions used, *vide infra*. There was no indication of the loss of neutral thymine in any of the spectra, consistent with the results reported in the previous BIRD study [16].

There is abundant experimental evidence that the loss of neutral base precedes backbone fragmentation in ODN anions in low charge states. For example, from the absence of product ions in the BIRD spectra of several doubly deprotonated 7-mers, acquired with the continuous ejection of the $(M - XH)^{-2}$ ion (*i.e.* double resonance experiments), Williams and coworkers demonstrated conclusively that the loss of XH (where X = A, C and G) represented the only primary dissociation channel at temperatures < 210 °C, with all other fragment ions originating from the $(M - XH)^{-2}$ ion [16]. Beauchamp and coworkers reported similar results for deprotonated dinucleotide ions [10]. Based on these and related studies it is reasonable to expect the 10-mers investigated here to react in a similar fashion, *i.e.* loss of neutral base, followed by backbone cleavage (eq 2.1a-c). However, the absence of the $(M - CH)^{-2}$ ions in the BIRD spectra of all three C-containing anions was unexpected and raised the possibility of a different dissociation pathway for these ions. To verify that the loss of CH was in fact the only primary dissociation channel, double resonance experiments were performed on the

33

C-containing 10-mers. All of the expected product ions of $(CT_9)^{-2}$, $(T_5CT_4)^{-2}$ and $(T_9C)^{-2}$ were absent in the BIRD spectra acquired for experiments in which continuous rf excitation, at the frequency of the $(M - CH)^{-2}$ ion ($\nu = 50.3$ kHz), was applied throughout the reaction. The product ions were restored when the frequency of the rf excitation was moved slightly off-resonance from the $(M - CH)^{-2}$ ion ($\nu = 49.8$ kHz), indicating that the disappearance of the fragment ions was due to the elimination of the only primary product ion rather than the loss of ions due to off-resonance excitation. These results are illustrated for $(CT_9)^{-2}$ in Figures 2.3a-c. The absence of the $(M - CH)^{-2}$ ions in the BIRD spectra can, therefore, be attributed to the slow dissociation kinetics for the loss of CH, compared with the secondary dissociation processes, such that the lifetimes of the $(M - CH)^{-2}$ ions are short. Double resonance experiments performed on the A- and G-containing ions also confirmed that the loss of neutral base precedes backbone fragmentation.

$$XT_9^{-2} \rightarrow (XT_9 - XH)^{-2} \rightarrow w_9^{-2} \qquad (2.1a)$$

$$T_5XT_4^{-2} \rightarrow (T_5XT_4 - XH)^{-2} \rightarrow (a_6 - XH)^- + w_4^- \qquad (2.1b)$$

$$T_9X^{-2} \rightarrow (T_9X - XH)^{-2} \rightarrow (T_9X - XH - H_2O)^{-2} \equiv (a_{10} - XH)^{-2} \qquad (2.1c)$$

34
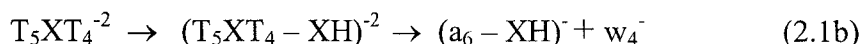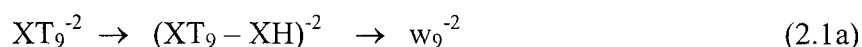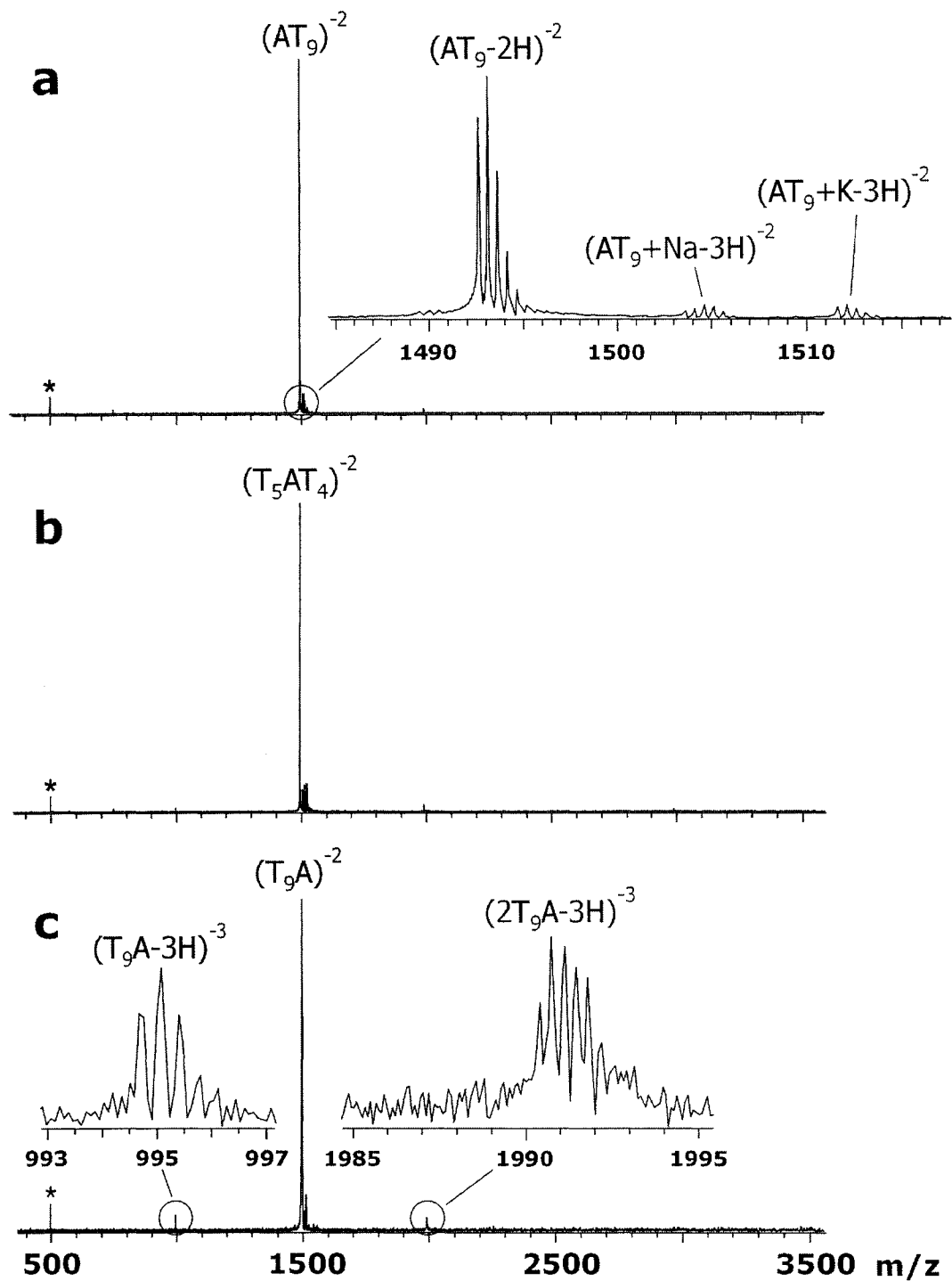
Figure 2.1 NanoES mass spectra of 1:1 $H_2O:CH_3CN$ solutions containing $\sim 10^{-4}$ M (a) AT_9, (b) T_5AT_4, (c) T_9A. The asterisk indicates a harmonic of the precursor ion [20].

35
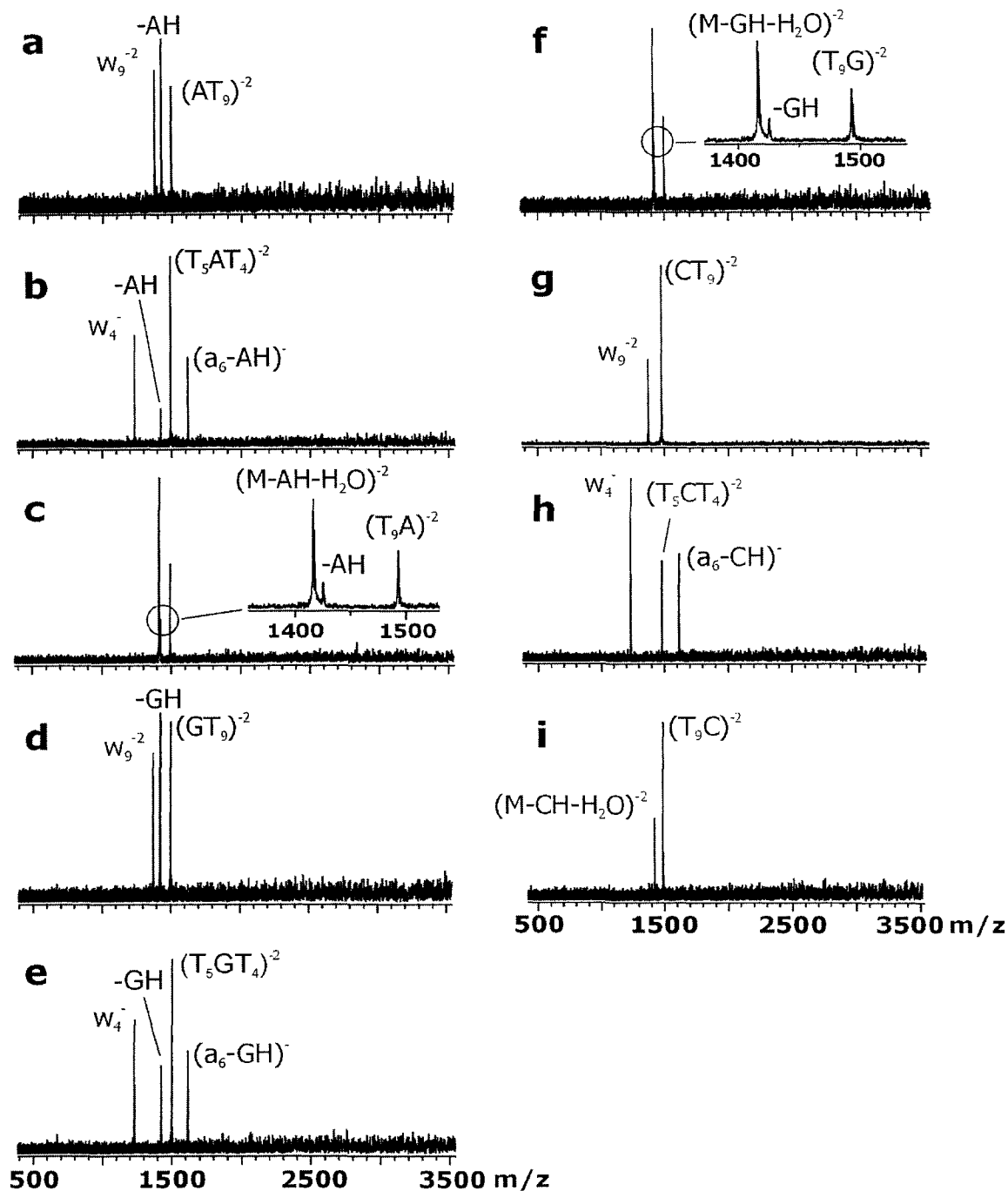
Figure 2.2 Blackbody infrared radiative dissociation spectra of doubly deprotonated DNA anions (a) $(AT_9)^{-2}$ at 152.5 °C and a reaction delay of 18 s, (b) $(T_5AT_4)^{-2}$ (192.3 °C, 3 s), (c) $(T_9A)^{-2}$ (171 °C, 9s), (d) $(GT_9)^{-2}$ (172 °C, 3.75 s), (e) $(T_5GT_4)^{-2}$ (160.5 °C, 15 s), (f) $(T_9G)^{-2}$ (134 °C, 55 s), (g) $(CT_9)^{-2}$ (191.1 °C, 50 s), (h) $(T_5CT_4)^{-2}$ (185.4 °C, 600 s), (i) $(T_9C)^{-2}$ (192.6 °C, 250 s).

36
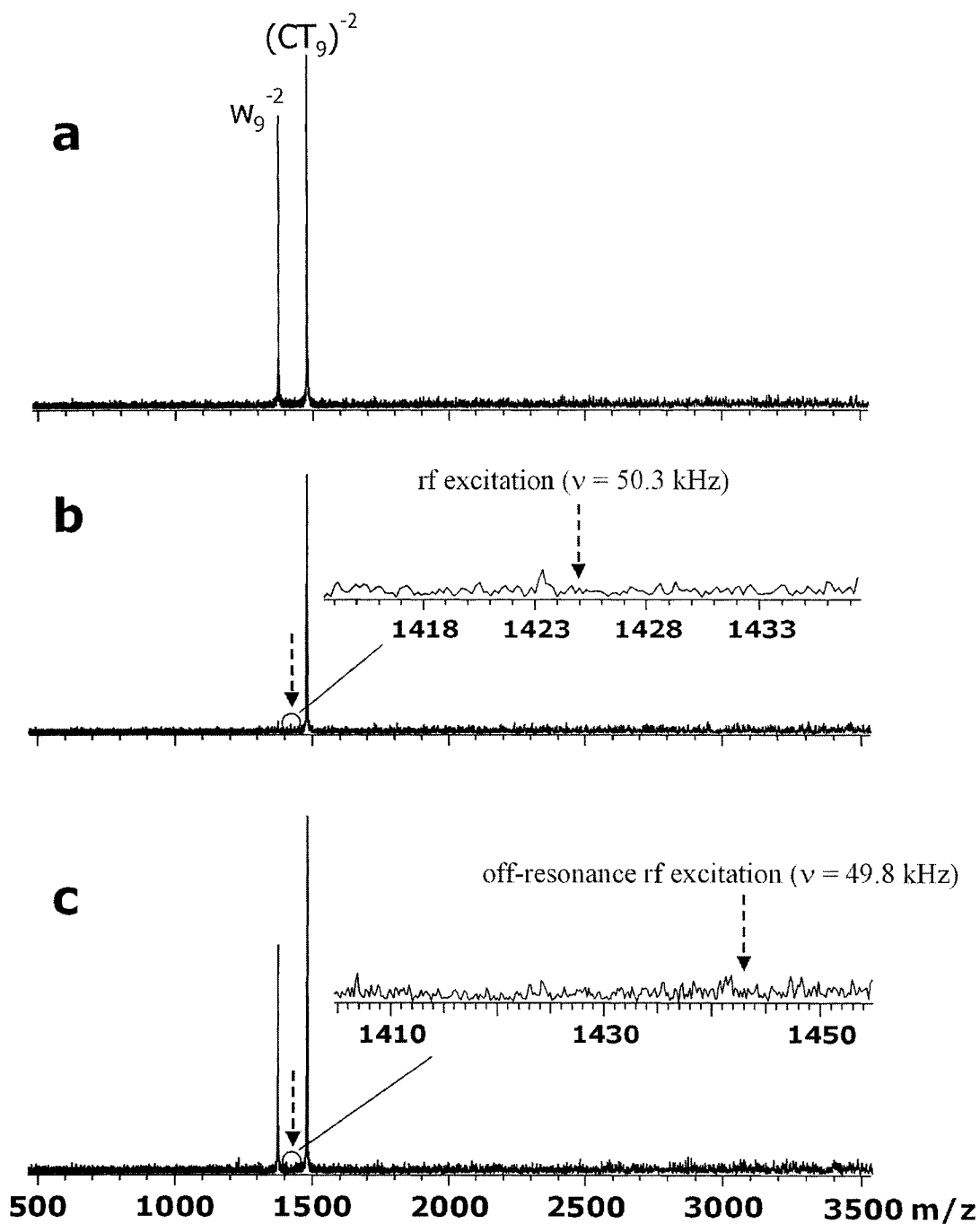
Figure 2.3 Blackbody infrared radiative dissociation spectra of the doubly deprotonated $(CT_9)^{-2}$ anion (a) at 190.2 °C and a reaction time of 100 s, (b) under the same conditions but with a continuous rf excitation at the frequency of the $(M - CH)^{-2}$ ion ($v = 50.3$ kHz), (c) restoration of w_9^{-2} ion when the frequency of the rf excitation was moved slightly off-resonance from the $(M - CH)^{-2}$ ion ($v = 49.8$ kHz).

37

2.3.2 Dissociation Kinetics and Arrhenius Parameters

The temperature dependent first-order rate constant (k) for the loss of neutral nucleobase was determined from the change in the natural log of the normalized intensity (abundance) of the ODN reactant ion ($I_{R,norm}$) with reaction time (eq 2.2). $I_{R,norm}$ was calculated using eq 2.3, where I_R is the abundance of the reactant ion and ΣI_P is the sum of the abundance of all product ions, including those produced by secondary reactions. Since the total charge of the precursor ion is conserved in the reaction products, the measured intensity of the product and reactant ions was not corrected for charge state. In principle, $I_{R,norm}$ should be calculated using the sum of the abundance of all the ions (reactant and products) within each isotope envelope. However, in cases where the BIRD spectra exhibit poor signal-to-noise ratio (S/N) it is difficult to accurately quantify the low abundance isotope peaks. In such cases, $I_{R,norm}$ was calculated using only the most abundant isotopic ion for the reactant and product ions. Shown in Figure 2.4a and b is the distribution of the differences in the normalized parent ion abundance obtained using these two approaches for $(AT_9)^{-2}$ and $(T_5AT_4)^{-2}$, respectively. It can be seen that the two methods yield similar values of $I_{R,norm}$, with differences typically less than $\pm15\%$. Consequently, the dissociation rate constants and activation energies should be independent of the method used to calculate $I_{R,norm}$. Illustrative kinetic plots, obtained for $(AT_9)^{-2}$ and $(T_9A)^{-2}$, at four different temperatures are shown in Figure 2.5. The plots are linear and exhibit near zero intercepts, as expected for simple first-order reactions. Plots of similar quality were obtained for all of the anions investigated. The first-order rate constant was determined from the slope of a linear least squares fit of the kinetic data

38
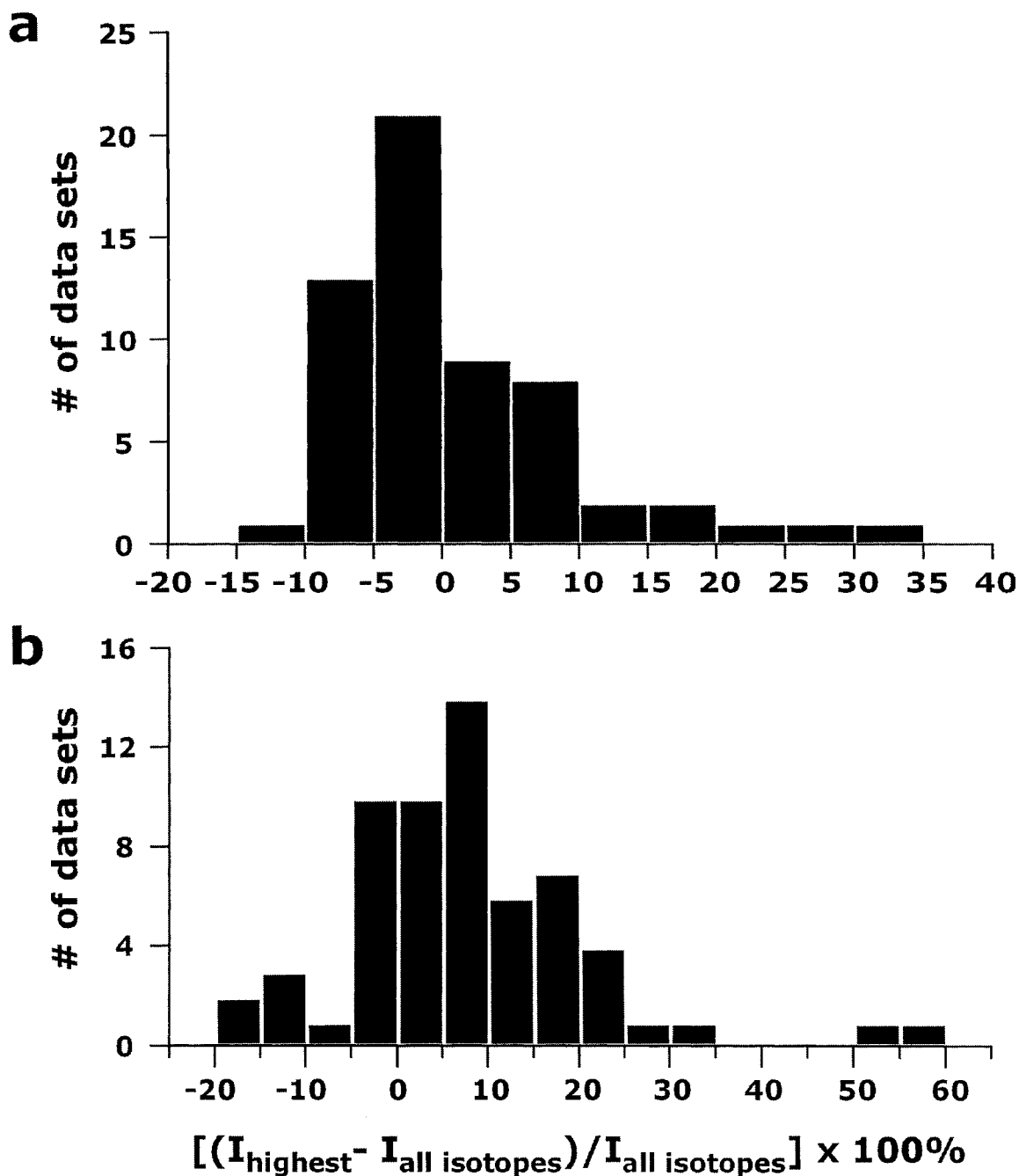
Figure 2.4 Distribution of the difference in $I_{R,norm}$ calculated using (i) the most abundant isotopic ion for the reactant and product ions ($I_{highest}$) and (ii) the sum of the abundance of all the ions within each isotope envelope ($I_{all\ isotopes}$) for (a) $(AT_9)^{-2}$ and (b) $(T_5AT_4)^{-2}$.

39
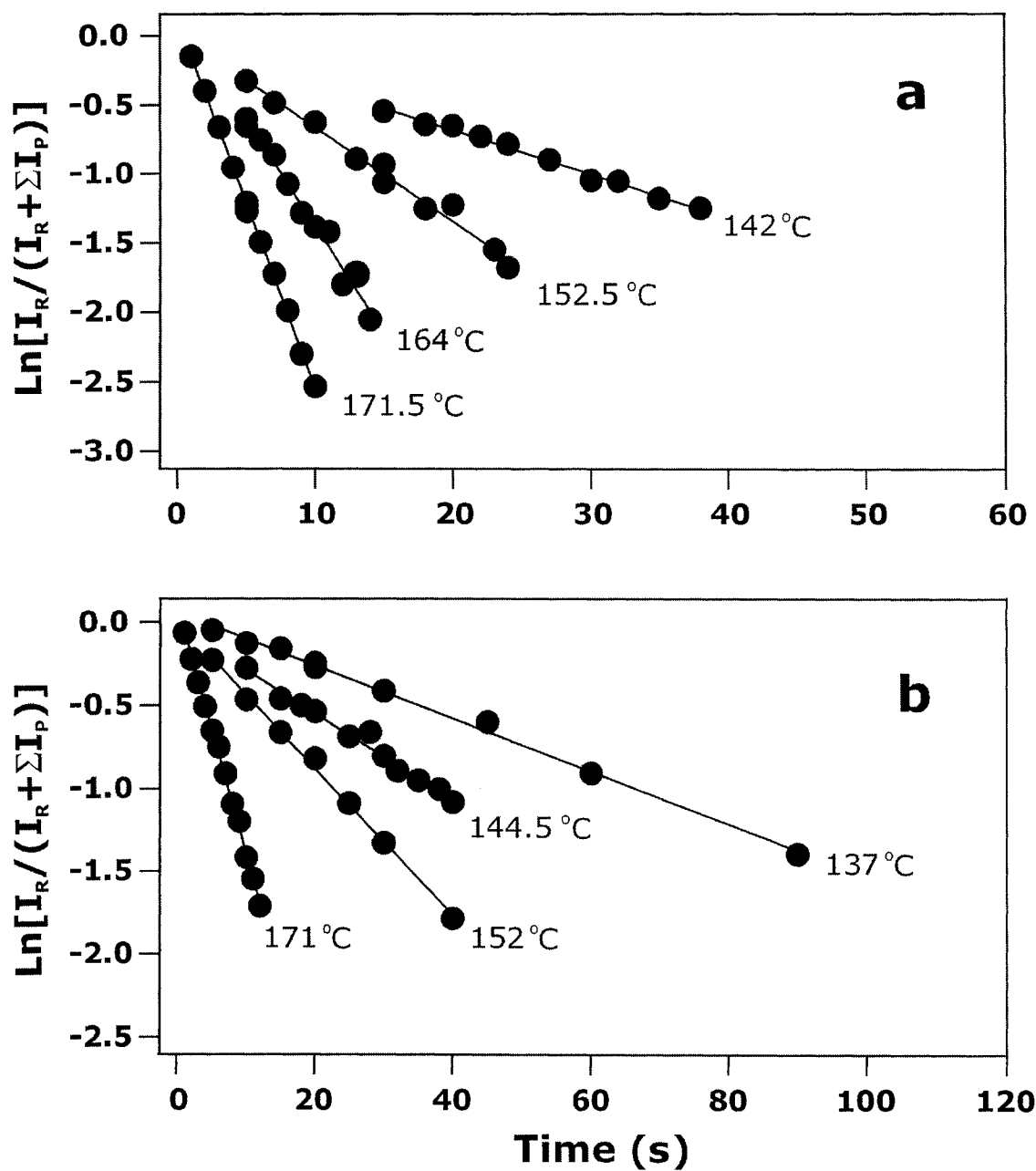
Figure 2.5   Dissociation kinetic data of (a) $(AT_9)^{-2}$, (b) $(T_9A)^{-2}$ obtained at the temperatures indicated.

40

obtained at each temperature investigated.

$$\ln\,(I_{R,norm,t}) = -\,kt \tag{2.2}$$

$$I_{R,norm} = I_R\,/(I_R + \Sigma I_P) \tag{2.3}$$

Arrhenius plots constructed from the temperature dependent rate constants for the loss of nucleobase are shown in Figure 2.6. For all of the ions investigated, linear plots were obtained. The kinetic data for the C-containing ions span a relatively small temperature range due to the very slow dissociation kinetics and an upper temperature limit of ~190 °C for the apparatus used in this work. The Arrhenius activation energy (E_a) and preexponential factor (A) were obtained from the slope and y-intercept, respectively, of a linear least squares fit of the temperature dependent kinetic data and the values are listed in Table 2.1. Also included in Table 2.1 are values for the entropy of activation ($\Delta S^{\ddagger}$), which corresponds to the difference in entropy between the transition state and the reactant, and which can be calculated from the corresponding A-factor using eq 2.4. A negative $\Delta S^{\ddagger}$ indicates a loss of entropy in the transition state (*i.e.* a tight transition state), a positive value indicates a gain in entropy (*i.e.* a loose transition state), and a value close to zero corresponds to a reaction that is entropically neutral. The kinetic reactivity and the Arrhenius parameters are discussed below in terms of the nature and position of the nucleobase.

$$A = (\mathrm{ekT/h})\,\exp(\Delta S^{\ddagger}/\mathrm{R}) \tag{2.4}$$

From an inspection of the Arrhenius plots in Figure 2.6 it is clear that the dissociation kinetics and energetics for the loss of XH are sensitive to the nature of the X and its position within the ODN. Over the temperature range investigated, the kinetics for the loss of the purine bases (A, G) are quite similar, within a factor of 5, but they are a factor of ~100 faster than the kinetics for the loss of CH. For base loss from the 5'

41

terminus, the trend in reactivity is: A ≈ G >> C; while for the 3′ terminus and internal

position the trend is: G > A >> C. The influence of position on reactivity is base

dependent: A, 5′ terminus (≡ 5′) > 3′ > internal; G, 3′ > 5′ > internal; C, 5′ > internal > 3′.

The dissociation E_a values are also sensitive to the nature of the base, with the purine

bases exhibiting lower values of E_a than cytosine (A: 23 - 27, G: 26 - 30, C: 35 - 37 kcal

mol^{-1}) and, to some extent, its position. For the loss of XH from the 5′ and 3′ termini, the

values of E_a have the following order: C > G > A; while for T_5XT_4 the trend is: C > A >

G (although the E_a for G and A differ by only 1 kcal mol^{-1}). It is important to note that

the relative energetics for the loss of neutral A and G could not have been predicted from

the relative reactivity of the bases observed over this temperature range. The A-factors

(and values of $\Delta S^{\ddagger}$) are also sensitive to the nature and position of the nucleobase. For the

loss of AH the A-factor range from 10^{10} to 10^{12} s^{-1} ($\Delta S^{\ddagger}$: –13 to –6 cal mol^{-1} K^{-1}); for the

loss of CH the A-factors are ~ 10^{14} s^{-1} ($\Delta S^{\ddagger}$: 3 to 6 cal mol^{-1} K^{-1}); while for GH, the A-

factors range from 10^{12} to 10^{14} s^{-1} ($\Delta S^{\ddagger}$: –8 to +4 cal mol^{-1} K^{-1}).

As previously noted, Williams and coworkers have reported Arrhenius parameters

for the loss of neutral base from some doubly deprotonated 7-mers and it is of interest to

compare their results [16] with the values obtained in the present work. The Arrhenius

parameters reported for the loss of AH from $d(A_7)^{-2}$, $d(AATTAAT)^{-2}$ and $d(TTAATTA)^{-2}$

in the previous study (E_a = 23 - 26 kcal mol^{-1}, A = 10^{10} - 10^{11} s^{-1}) are in agreement with

the present values. For the loss of CH and GH from $d(CCGGCCG)^{-2}$ similar parameters

were reported (GH: 30.1 kcal mol^{-1}, $10^{12.5}$ s^{-1}; CH: 31.1 kcal mol^{-1}, $10^{13.1}$ s^{-1}). While the

parameters measured for the loss of GH in the two studies are in reasonable agreement,

the results from the loss of CH are not; the parameters measured in the present work are

42
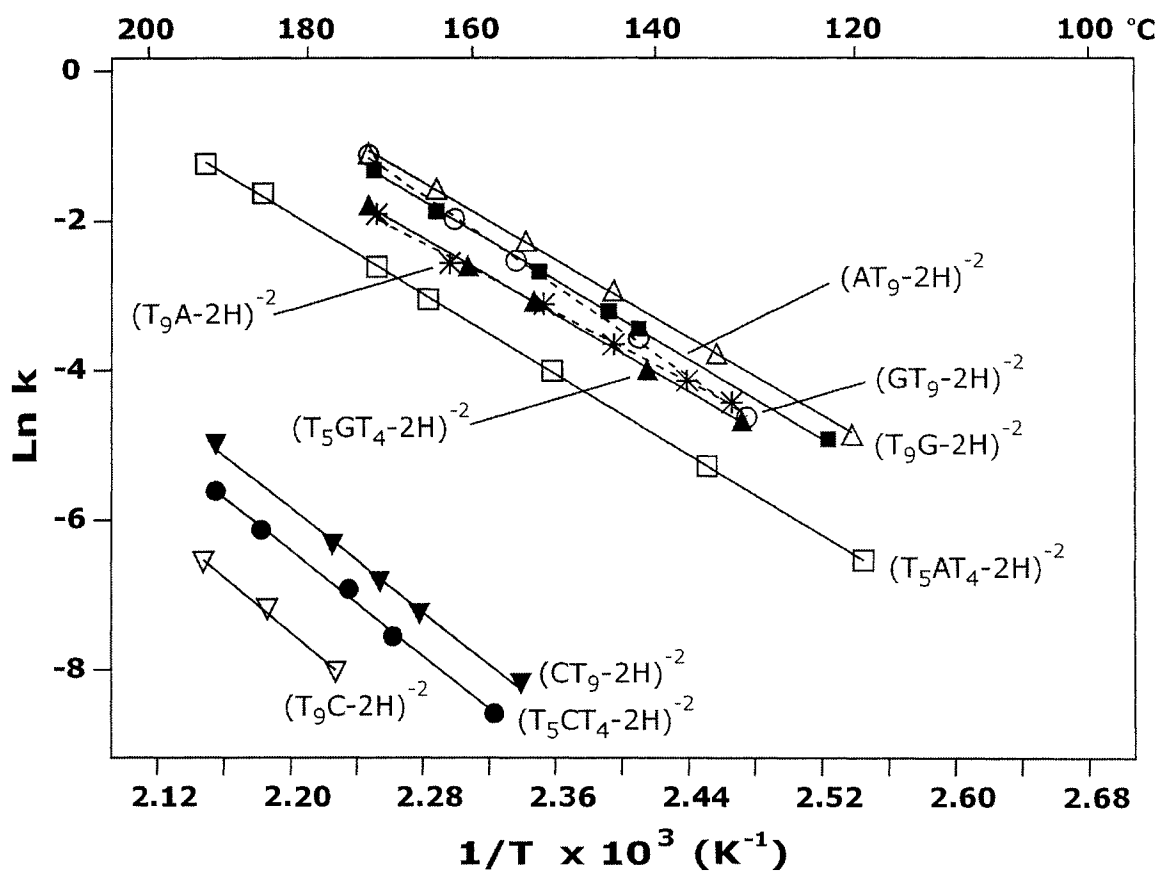
Figure 2.6 Arrhenius plots for the loss of neutral nucleobase from $(AT_9)^{-2}$, ($\blacksquare$); $(T_5AT_4)^{-2}$, ($\square$); $(T_9A)^{-2}$, ($*$); $(GT_9)^{-2}$, ($\circ$); $(T_5GT_4)^{-2}$, ($\blacktriangle$); $(T_9G)^{-2}$, ($\triangle$); $(CT_9)^{-2}$,($\blacktriangledown$); $(T_5CT_4)^{-2}$, ($\bullet$); $(CT_9)^{-2}$, ($\triangledown$).

43

Table 2.1 Arrhenius activation parameters for the loss of neutral nucleobase from some doubly deprotonated oligodeoxynucleotide anions containing a single reactive base.

Oligodeoxynucleotide	E_a (kcal mol^{-1}) [a]	A (s^{-1}) [a]	$\Delta S^{\ddagger}$ (cal mol^{-1} K^{-1}) [b]
$(AT_9 - 2H)^{-2}$	25.9 ± 0.2	$10^{12.1 \pm 0.1}$	-6
$(T_5AT_4 - 2H)^{-2}$	26.7 ± 0.2	$10^{12.0 \pm 0.1}$	-6
$(T_9A - 2H)^{-2}$	23.0 ± 0.6	$10^{10.5 \pm 0.3}$	-13
$(GT_9 - 2H)^{-2}$	30.1 ± 0.5	$10^{14.3 \pm 0.3}$	4
$(T_5GT_4 - 2H)^{-2}$	25.5 ± 0.3	$10^{11.7 \pm 0.2}$	-8
$(T_9G - 2H)^{-2}$	25.7 ± 0.3	$10^{12.2 \pm 0.2}$	-5
$(CT_9 - 2H)^{-2}$	34.6 ± 1.1	$10^{14.1 \pm 0.6}$	3
$(T_5CT_4 - 2H)^{-2}$	35.0 ± 1.1	$10^{14.0 \pm 0.5}$	3
$(T_9C - 2H)^{-2}$	37.2 ± 2.3 [c]	$10^{14.6 \pm 1.1}$ [c]	6

a. Errors correspond to one standard deviation.

b. $\Delta S^{\ddagger}$ values calculated at 423 K using eq 2.4.

c. Arrhenius parameters determined from kinetic data that spanned only 25°C.

44

significantly larger.

The similarities and differences between the Arrhenius parameters measured in these two BIRD studies are noteworthy for two reasons. First, they highlight the influence of the chemical environment (*i.e.* context) on the reactivity of the bases. The similarity in the kinetics and energetics for the loss of AH from these A- and T-rich ODNs indicates that the environments of the reacting base are similar. In contrast, the reactivity of the cytosine bases is sensitive to the sequence of the ODN anions, with decreased reactivity in the T-rich oligomers compared to the $d(CCGGCCG)^{-2}$ ion. The influence of the chemical environment on the Arrhenius parameters is discussed in more detail below. Secondly, an important consideration when performing BIRD experiments on ions with molecular weights (MW) between 1 - 5 kDa is whether the ions are thermalized, such that the Arrhenius parameters correspond to the values that would be obtained from experiments performed in the high pressure limit. The agreement between the Arrhenius parameters for the loss of AH from the 7-mers (MW ~2 kDa) and 10-mers (MW ~3 kDa) strongly suggests that the observed dissociation kinetics are not governed simply by the rate of photon absorption and that the 10-mers are in indeed in thermal equilibrium. This conclusion is reasonable given that Williams and coworkers have found that, within the same temperature window and for similar Arrhenius parameters, the dissociation kinetics of some protonated peptides with MW's of ~2 kDa were in the rapid energy exchange limit [21].

It is also worthwhile commenting on the apparent lack of agreement between the trend in base reactivity established in the present work and previous studies, even for ODNs with similar sequence. For example, the trend in kinetic reactivity observed in a

45

CID study of doubly deprotonated T-rich 8-mers, wherein the reactive base occupied the 4th and 5th position, is G > C ≈ A >> T [11]. In the present work, the trend in *average* kinetic reactivity based on *average* Arrhenius parameters for the loss of each of the nucleobases (A: E_a = 25.2 kcal mol^{-1}, A = $10^{11.5}$ s^{-1}; G: E_a = 27.1 kcal mol^{-1}, A = $10^{12.7}$ s^{-1}; C: E_a = 35.6 kcal mol^{-1}, A = $10^{14.2}$ s^{-1}) is: G ≈ A > C. The lack of agreement can be rationalized by the fact that internal energy distributions of the reacting ions produced with BIRD and CID are different. Unlike with the BIRD technique, wherein the ions adopt a Boltzmann distribution of internal energy at a known temperature, the energy distribution in the typical CID experiment is poorly defined. Furthermore, the fact that the loss of T has been observed with CID, but not with BIRD, indicates that higher internal energies are achieved with CID. Assuming that the Arrhenius parameters measured in the present work accurately describe the dissociation kinetics over a broad temperature range, it is possible to predict the trend in kinetic reactivity at temperatures higher than those studied here. Shown in Figure 2.7 are Arrhenius plots, constructed with the average Arrhenius parameters, spanning temperatures of 100 to 700 °C. Based on these plots, the predicted trend in reactivity at temperatures between 200 and 500 °C is G > A > C. From 500 to 600 °C the trend is G > C ≈ A, which is consistent with the results reported by Gross and coworkers for the 8-mers [11]. Therefore, collisional activation of the 8-mers studied with an ion trap appear to produce an internal energy distribution that is similar to that of thermalized ions with a temperature of 500 to 600 °C. It is worthwhile to point out that at even higher temperatures, >1000 °C, the trend in kinetic reactivity is parallel to the trend in dissociation E_a values: C > G > A. In other words, the most

46

reactive base has the highest dissociation E_a. This observation highlights the need for caution when trying to infer trends in energetics from reactivity.

2.3.3 Dissociation Mechanism and the Influence of Intramolecular Solvation

As described above, the loss of a neutral nucleobase from a deprotonated ODN requires that proton transfer to the base accompany cleavage of the N-glycosidic bond, either before or in concert with bond cleavage, or after the base is lost in its deprotonated form. As the present study represents the first systematic study of the dissociation energies for loss of neutral base from specific positions, it is of interest to compare the measured values of E_a with the PA and ΔH_{acid} of the free nucleobase and nucleoside to establish whether there is any correlation. The PA's of the free nucleobases have been established both experimentally and theoretically. Using the kinetic method, Greco and coworkers determined PA's for the deoxyribose nucleosides (dG 234.4 > dA 233.6 $\approx$ dC 233.2 >> dT 224.9 kcal mol^{-1}) and the corresponding free nucleobases (G 227.4 > C 225.9 > A 224.2 >> T 209.0 kcal mol^{-1}) [22]. A similar trend in PA's was established for the nucleobases from theoretical calculations performed by Russo and coworkers: G 230.3 > C 229.1 > A 225.8 > T 208.8 kcal mol^{-1} [23]. Clearly, the trend in the dissociation E_a's measured in the present work does not parallel the trend in PA's of either the nucleobases or the nucleosides, indicating that, if the base is protonated prior to cleavage of the glycosidic bond, additional factors influence the dissociation energetics. An alternative mechanism envisions the loss of the base initially in its deprotonated form (X$^-$), via a 1,2-elimination mechanism involving H-abstraction at the C-2 of the deoxyribose by the neighbouring deprotonated phosphate group [4, 8, 10, 24], followed by proton abstraction from the modified ODN. If the differences in the strengths of the

47
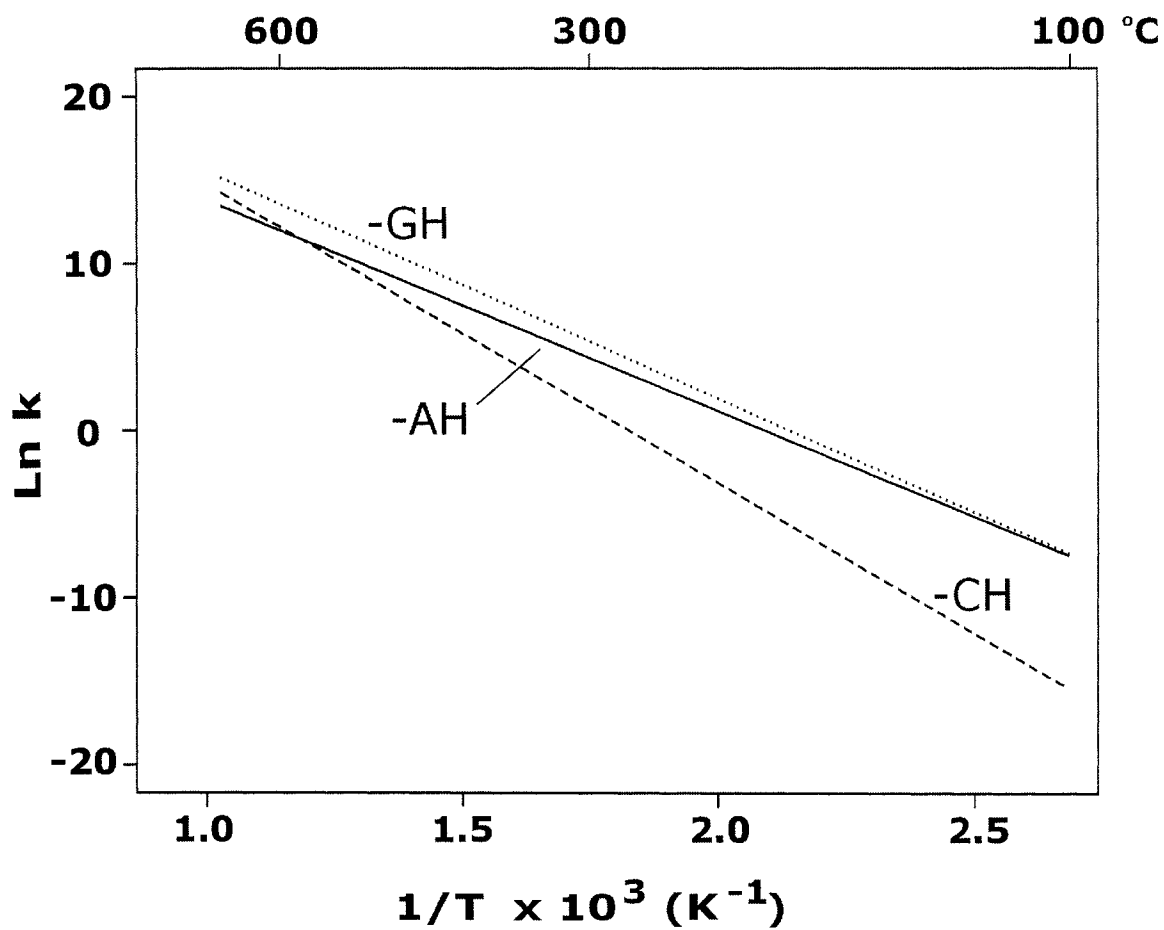
Figure 2.7 Extrapolated Arrhenius plots constructed with the average Arrhenius parameters for the loss of neutral nucleobase, A, (-), G, (...) and C, (---), from the doubly deprotonated 10-mer ODNs.

N-glycosidic bond are similar to the differences in the nucleobase N-H bond energies [25], the energy barrier for the reaction should reflect differences in the ΔH_{acid} of the nucleobases. Marshall and coworkers have recently reported values of ΔH_{acid}, determined from *ab initio* calculations (MP2/6-31+G*//HF/6-31+G*), for the free nucleobases [26]. In all cases, the hydrogen at the linkage nitrogen was found to be the most acidic, with a ΔH_{acid} of ~327 kcal mol^{-1} for A, G and T and 337 kcal mol^{-1} for C. If the base is lost in its deprotonated form, and in the absence of other effects, the dissociation energies for the loss of A, G and T should be similar but significantly higher for C. While it could be argued that the general trend in E_a values for A, G and C are more or less in agreement with the trend in the ΔH_{acid} values, the unusual stability of T cannot be explained by an unusually high ΔH_{acid}. From this analysis it can be concluded that the differences in the dissociation energies for the bases do not arise simply from differences in the acid/base properties of the nucleobases in the gas phase.

The absence of correlation between the dissociation E_a values and the gas phase acid/base properties of the bases, in addition to the influence of sequence and position on the Arrhenius parameters measured for base loss, could be the result of i) different dissociation mechanisms, which depend on the nature and position of the base, and ii) the presence of intramolecular interactions, perhaps hydrogen bonds and stacking interactions between nucleobases or hydrogen bonds (ionic or neutral) between the base and phosphate groups. While the possibility of multiple mechanisms cannot be discounted, it is, in our opinion, unlikely that the influence of sequence and position on the Arrhenius parameters arises simply from operation of different mechanisms. Instead,

49

differential solvation of the reactive base is a more plausible explanation for the variability in the Arrhenius parameters.

At present there are few data available on the conformation of ODN anions in gas phase. Recently, Bowers and coworkers, using ion mobility measurements and molecular modeling identified base-base interactions (stacking and hydrogen bonding) in the deprotonated dinucleotide anions [27]. Evidence of extensive intramolecular interactions in larger ODN anions has also been obtained from collision cross section measurements [28, 29]. Clemmer and coworkers measured collision cross sections and performed molecular dynamics simulations on $d(T_{10})^{-n}$ ions, where $n = 2$ to 6 [28]. It was observed that the collision cross section increased with charge state, a result that was explained by Coulombic repulsion-induced unfolding of the anion. Molecular modeling of anions with different charge states and distributions suggested that the $d(T_{10})^{-n}$ ions favour compact globular structures involving extensive base stacking and hydrogen bonds at low charge states (*i.e.* $n = -2$, -3) and elongated structures at higher charge states. Douglas and coworkers recently reported collision cross sections for some deprotonated 28-, 40- and 55-mers with varying charge states [29]. At lower charge states, the ions were found to have globular or spherical structures, while at higher charge states the ions adopted an extended conformation.

Based on the aforementioned studies, it is reasonable to expect intramolecular interactions to be present in the doubly deprotonated 10-mers investigated in the present work. Although it is impossible to identify specific interactions, some insight into their influence on the dissociation process can be obtained from the magnitude of the Arrhenius parameters. Intramolecular solvation of the reactive nucleobase or the charged

50

groups (assuming base loss proceeds by a charge directed mechanism) will contribute to the dissociation energy since these interactions must be broken for the base to be lost (Figure 2.8). Consequently, the observed E_a (i.e. $E_{a,obs}$) will reflect the contribution of the intrinsic dissociation energy ($E_{a,intrin}$) plus the energy required to overcome the intramolecular interactions ($E_{a,solv}$). Unfortunately, it is not possible to separate the contribution of $E_{a,intrin}$ and $E_{a,solv}$ to the values of E_a measured in the present work. However, cleavage of the intramolecular interactions, in addition to the glycosidic bond, during the dissociation process will also influence the magnitude of the A-factors and $\Delta S^{\ddagger}$. Our laboratory has previously shown that the dissociation kinetics of noncovalent protein complexes, stabilized by an array of intermolecular hydrogen bonds, are characterized by large A-factors (and $\Delta S^{\ddagger}$'s) [19, 30]. These results are general and have been attributed to the cleavage of the noncovalent interactions and concomitant softening of numerous vibrational modes along the reaction coordinate. Therefore, the observed $\Delta S^{\ddagger}$ will reflect the contribution of the intrinsic entropy of activation ($\Delta S^{\ddagger}_{intrin}$) plus the gain in entropy resulting from the cleavage of the intramolecular interactions ($\Delta S^{\ddagger}_{solv}$). If all of the bases are lost via the same mechanism, and in the absence of internal solvation, the magnitude of the $\Delta S^{\ddagger}$ should be similar in all cases. Consequently, differences in $\Delta S^{\ddagger}$ must reflect differences in $\Delta S^{\ddagger}_{solv}$, the extent to which the reactive base is internally solvated. Proceeding from this premise, the negative values of $\Delta S^{\ddagger}$ determined for the A-containing ions suggest that, within the T-rich ODNs, adenine participates in the fewest or the weakest intramolecular interactions. This is perhaps surprising given the propensity of these bases to participate in Watson-Crick intermolecular hydrogen bonding in DNA duplexes. That similar A-factors were measured for the A-rich 7-mer [16] further

51

suggests that adenine-adenine interactions are not prevalent. In contrast, the larger (and positive) $\Delta S^{\ddagger}$ values determined for the loss of CH indicate a greater ability of cytosine to participate in intramolecular interactions with the thymine bases or the backbone. The range of $\Delta S^{\ddagger}$ values (both positive and negative) measured for the loss of GH indicate that extent of intramolecular solvation of guanine depends on its position within the ODN. Beauchamp and coworkers have previously reported that the guanine amino group can form an ionic hydrogen bond with the adjacent 3' deprotonated phosphate group [10]. It is also interesting to note that the larger $\Delta S^{\ddagger}$ (and E_a) measured for the loss of GH from the terminal 5' position is consistent with the previous observation that, in this position, G is stabilized by a hydrogen bond with the C-5 OH group of the deoxyribose group [31].

Our laboratory is currently determining Arrhenius parameters for the dissociation of larger T-rich ODN anions to determine whether the trends in the dissociation E_a and $\Delta S^{\ddagger}$ values measured for the 10-mers are general.
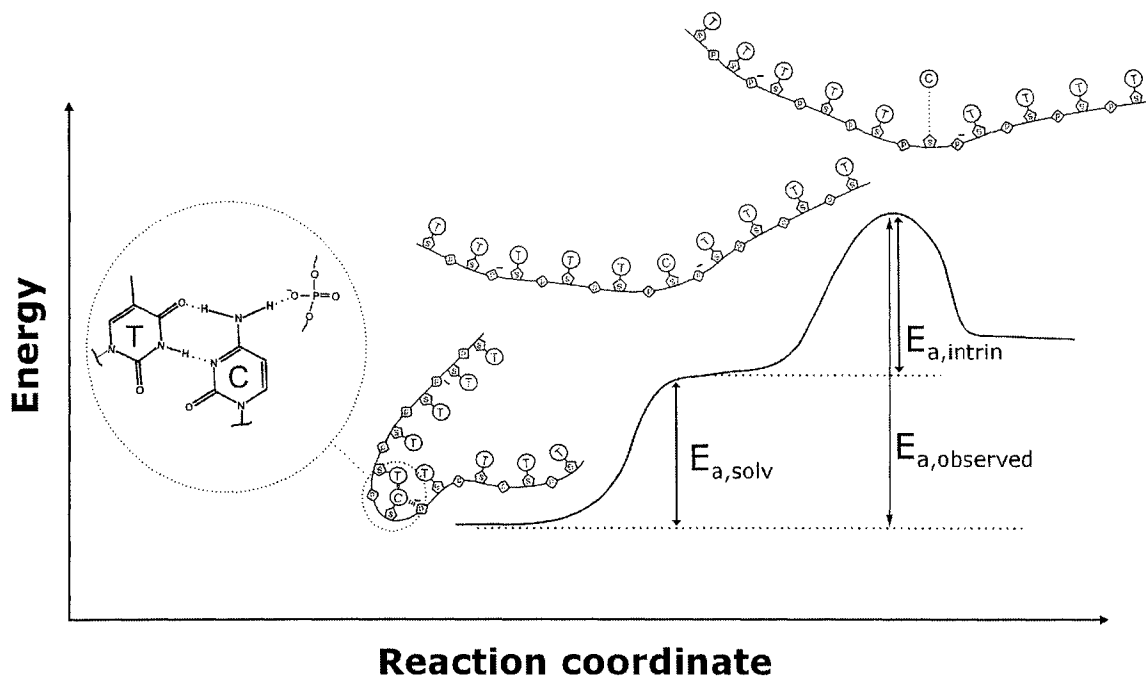
Figure 2.8 Hypothetical energy diagram for the loss of a nucleobase from a doubly deprotonated ODN ion. The observed E_a contains the energy required to break intramolecular solvation of the base ($E_{a,solv}$) and the energy required to cleave the glycosidic bond ($E_{a,intrin}$).

2.4 Conclusions

The thermal decomposition of a series of T-rich doubly deprotonated ODN 10-mers with a single reactive nucleobase has been studied using the BIRD technique. From the temperature dependence of the dissociation kinetics, Arrhenius activation parameters for the loss of specific nucleobases have been obtained for the first time. The dissociation kinetics and energetics for the loss of a nucleobase from a given position within the ODNs are found to be sensitive to the identity of the base. The trend in values of E_a for the loss of base from the 5′ and 3′ termini is: A < G < C, while for loss of base from an internal position the trend is: A ≈ G < C. The E_a for the loss of a given base is sensitive to the location of the base within the ODN. The trend in the energetic data does not provide support for any of the commonly proposed mechanisms for the loss of neutral nucleobase. However, the results do indicate that the differences in dissociation E_a values do not originate solely from differences in acidic or basic character of the bases. Instead, the ability of the nucleobases to participate in intramolecular interactions appears to influence the dissociation energetics and dynamics. These results highlight the complexity of the base loss reaction and the difficulty in devising experiments to elucidate the mechanism(s).

54

2.5 Literature Cited

(1)   Zhu, L.; Parr, G. R.; Fitzgerald, M. C.; Nelson, C. M.; Smith, L. M. *J. Am. Chem. Soc.* **1995**, *117*, 6048-6056.

(2)   McLuckey, S. A.; Vaidyanathan, G.; Habibi-Goudarzi, S. *J. Mass Spectrom.* **1995**, *30*, 1222-1229.

(3)   Phillips, D. R.; McCloskey, J. A. *Int. J. Mass Spectrom. Ion Processes* **1993**, *128*, 61-82.

(4)   Barry, J. P.; Vouros, P.; Schepdael, A. V.; Law, S.-J. *J. Mass Spectrom.* **1995**, *30*, 993-1006.

(5)   Bartlett, M. G.; McCloskey, J. A.; Manalili, S.; Griffey, R. H. *J. Mass Spectrom.* **1996**, *31*, 1277-1283.

(6)   McLuckey, S. A.; Vaidyanathan, G. *Int. J. Mass Spectrom. Ion Processes* **1997**, *162*, 1-16.

(7)   McLuckey, S. A.; Van Berkel, G. J.; Glish, G. L. *J. Am. Soc. Mass Spectrom.* **1992**, *3*, 60-70.

(8)   McLuckey, S. A.; Habibi-Goudarzi, S. *J. Am. Chem. Soc.* **1993**, *115*, 12085-12095.

(9)   Little, D. P.; Aaserud, D. J.; Valaskovic, G. A.; McLafferty, F. W. *J. Am. Chem. Soc.* **1996**, *118*, 9352-9359.

(10)   Rodgers, M. T.; Campell, S.; Marzluff, E. M.; Beauchamp, J. L. *Int. J. Mass Spectrom. Ion Processes* **1994**, *137*, 121-149.

(11)   Wan, K. X.; Gross, M. L. *J. Am. Soc. Mass Spectrom.* **2001**, *12*, 580-589.

55

(12) Luo, H.; Lipton, M. S.; Smith, R. D. *J. Am. Soc. Mass Spectrom.* **2002**, *13*, 195-199.

(13) Wan, K. X.; Gross, J.; Hillenkamp, F.; Gross, M. L. *J. Am. Soc. Mass Spectrom.* **2001**, *12*, 193-205.

(14) Wang, Z.; Wan, K. X.; Ramanathan, R.; Taylor, J. S.; Gross, M. L. *J. Am. Soc. Mass Spectrom.* **1998**, *9*, 683-691.

(15) Gross, J.; Hillenkamp, F.; Wan, K. X.; Gross, M. L. *J. Am. Soc. Mass Spectrom.* **2001**, *12*, 180-192.

(16) Klassen, J. S.; Schnier, P. D.; Williams, E. R. *J. Am. Soc. Mass Spectrom.* **1998**, *9*, 1117-1124.

(17) Ho, Y.; Kebarle, P. *Int. J. Mass Spectrom. Ion Processes* **1997**, *165*, 433-455.

(18) Hannis, J. C.; Muddiman, D. C. *Int. J. Mass Spectrom.* **2002**, *219*, 139-150.

(19) Felitsyn, N.; Kitova, E. N.; Klassen, J. S. *Anal. Chem.* **2001**, *73*, 4647-4661.

(20) Marshall, A. G.; Grosshans, P. B. *Anal. Chem.* **1991**, *63*, 215A-229A.

(21) Price, W. D.; Williams, E. R. *J. Phys. Chem. A* **1997**, *101*, 8844-8852.

(22) Greco, F.; Liguori, A.; Sindona, G.; Uccella, N. *J. Am. Chem. Soc.* **1990**, *112*, 9092-9096.

(23) Russo, N.; Toscano, M.; Grand, A.; Jolibois, F. *J. Comp. Chem.* **1998**, *19*, 989-1000.

(24) Cerny, R. L.; Gross, M. L.; Grotjahn, L. *Anal. Biochem.* **1986**, *156*, 424-435.

(25) Chen, E. S. D.; Chen, E. C. M.; Sane, N. *Biochem. Biophys. Res. Commun.* **1998**, *246*, 228-230.

(26) Freitas, M. A.; Shi, S. D.-H.; Hendrickson, C. L.; Marshall, A. G. *J. Am. Chem. Soc.* **1998**, *120*, 10187-10193.

(27) Gidden, J.; Bowers, M. T. *Eur. Phys. J. D* **2002**, *20*, 409-419.

(28) Hoaglund, C. S.; Liu, Y.; Ellington, A. D.; Pagel, M.; Clemmer, D. E. *J. Am. Chem. Soc.* **1997**, *119*, 9051-9052.

(29) Moradian, A.; Scalf, M.; Westphall, M. S.; Smith, L. M.; Douglas, D. J. *Int. J. Mass Spectrom.* **2002**, *219*, 161-170.

(30) Kitova, E. N.; Bundle, D. R.; Klassen, J. S. *J. Am. Chem. Soc.* **2002**, *124*, 5902-5913.

(31) Nir, E.; Imhof, P.; Kleinermanns, K.; de Vries, M. S. *J. Am. Chem. Soc.* **2000**, *122*, 8091-8092.

Chapter 3

Thermal Decomposition of Multiply Charged T-Rich Oligonucleotide Anions in the Gas Phase. Influence of Internal Solvation on the Arrhenius Parameters for Neutral Base Loss*

3.1 Introduction

Mass spectrometry (MS), combined with electrospray ionization (ES) or matrix-assisted laser desorption/ionization (MALDI), is an important tool for sequencing DNA and RNA oligonucleotides. Direct oligonucleotide sequencing is normally carried out using tandem MS (*i.e.* MS/MS) whereby the gaseous oligonucleotide ion of interest is first isolated using one stage of MS, then subjected to collisional or radiative heating (activation) to induce fragmentation, followed by a second stage of MS to analyze the mass of the fragment ions. Sequence information is deduced from the mass difference for sequential fragment ions which share the same general structure, *vide infra* [1]. Because sequence is determined from mass differences, the tandem MS approach is equally applicable to oligonucleotides containing natural, unnatural or modified residues.

While tandem MS is now routinely used to deduce sequence information for oligonucleotides, the mechanisms of fragmentation of these biopolymers in the gas phase are not fully understood. Studies of the fragmentation of gaseous multiply deprotonated oligodeoxynucleotide (ODN) ions, the focus of the present study, have shown that

* A version of this chapter has been submitted for publication: Daneshfar, R.; Klassen, J. S. *J. Am. Soc. Mass Spectrom.*

dissociation proceeds initially by the loss of a nucleobase, either in its neutral or deprotonated form, with subsequent cleavage of the adjacent 3′ C-O phosphodiester bond of the deoxyribose to produce complementary ions, referred to as [a-Base] and w ions according to the nomenclature proposed by McLuckey *et al.* [2]. The tendency for bases to be lost in their neutral or deprotonated form depends on the charge state of the ODN, with higher charge states favouring the loss of deprotonated base. Several mechanisms have been proposed for the loss of nucleobases from ODN anions and these have been recently reviewed by Gross and coworkers [3, 4]. The different mechanisms fall into two categories, those in which the nucleobase is lost in its deprotonated form, which may be followed by proton abstraction from the ODN to yield the neutral base, and those in which proton transfer from the ODN to the nucleobase occurs prior to or in concert with cleavage of the glycosidic bond, such that the base is lost directly as a neutral. It has been suggested that the different mechanisms might be distinguished based on the relative reactivity of the four DNA bases, adenine (A), guanine (G), cytosine (C) and thymine (T). Specifically, if the base is protonated prior to cleavage of the glycosidic bond, the relative reactivity of the bases might be expected to follow the trend in gas phase basicities or proton affinities of the nucleobase. If the base is initially lost in its deprotonated form, the relative reactivity is expected to follow the trend in gas phase acidities. Underlying these arguments are the important assumptions that the strength of the N-glycosidic bonds for the four bases are similar and that cleavage of the glycosidic bond represents the rate limiting step for base loss. The loss of the nucleobases in their deprotonated form generally follows the trend, $A^- > T^- > G^- \approx C^-$, although somewhat different trends have also been reported [5]. Interestingly, the trend in reactivity does not

59

strictly follow the trend in gas phase acidity or deprotonation enthalpy for the nucleobases, $A \approx G \approx T < C$ [6]. Numerous studies of neutral base loss from ODN anions have been reported [3-5, 7-17]. However, no general trend in the relative kinetic reactivity of the bases has been identified. Instead, the relative reactivity seems to be influenced by a number of factors, notably the size, sequence and charge state of the ODN as well the internal energy of the ions.

The first quantitative study of the kinetics and energetics for the loss of neutral nucleobases from gaseous ODN anions was carried out by Williams and coworkers [14]. Using the blackbody infrared radiative dissociation (BIRD) technique, they determined Arrhenius activation energies (E_a) and preexponential factors (A) for the loss of AH, CH and GH from some doubly deprotonated 7-mers. The loss of TH was not observed at reaction temperatures of up to 210 °C. Because all of the ODNs investigated contained multiple reactive bases, the reported Arrhenius parameters were *average* values, reflecting the loss of base from multiple positions. The first quantitative study of the Arrhenius parameters for the loss of *individual* nucleobases was recently reported by our laboratory [17]. BIRD was performed on a series of doubly deprotonated T-rich ODN anions of the type XT_9, T_9X and T_5XT_4, where $X = A$, G or C. Because the T residues are unreactive, it was possible to quantify the Arrhenius parameters for the loss of the individual AH, GH and CH from the 5′ and 3′ termini, and the internal position of the 10-mers. The trend in the dissociation E_a values was shown to be sensitive to the position of the nucleobase: $C > G > A$ (5′ and 3′ termini), $C > A > G$ (internal position). Importantly, it was noted that the trends in E_a values do not simply follow trends in either gas phase deprotonation enthalpies or proton affinities, and by themselves do not provide

60

insight into whether the reactive nucleobase is initially protonated prior to cleavage of the glycosidic bond or whether the base is initially lost in its deprotonated form. It was suggested that the Arrhenius parameters for base loss were influenced by noncovalent intramolecular interactions involving the reactive nucleobase. Based on the trends in E_a and A values, it was further suggested that, independent of the position within the 10-mer, C participates in greater internal solvation than do A or G.

A recent BIRD study on the loss of neutral nucleobases from T-rich 10-mers revealed the importance of internal solvation on the reactivity of the nucleobases and suggested the possibility that there may be inherent differences in the internal solvation of A, G and C within the T-rich ODN anions [17]. An interesting question, not addressed in this previous study, is how size and charge state of ODN anions influence the degree of internal solvation and, correspondingly, the kinetics and energetics of neutral base loss. The present study seeks to answer this question and to further test the hypothesis that there are inherent differences in the intramolecular solvation of A, G and C within the T-rich ODN anions. Time-resolved BIRD experiments have been performed on doubly and triply deprotonated T-rich 15- and 20-mer anions containing one reactive base (X) at the 5' or 3' termini, XT_{14}, XT_{19}, and $T_{19}X$, where X = A or C. From the temperature dependence of the dissociation rate constants for the loss of neutral A or C, Arrhenius activation parameters have been determined. Insights into the influence of base solvation and N-glycosidic bond cleavage on the reaction dynamics and energetics for base loss were deduced from a comparison of the Arrhenius parameters determined for the 15- and 20-mers, as well as values previously reported for the XT_9 and T_9X 10-mers. To further explore the possible differences in nucleobase solvation within the ODN

61

anions, gas phase hydrogen/deuterium exchange has been performed on the triply deprotonated A- and C-containing 20-mers. Additionally, BIRD experiments were carried out on triply deprotonated noncovalent complexes of T_{20} with neutral AH or CH to establish whether, when bound noncovalently to ODN anions, the nucleobases experience differences in intermolecular solvation.

3.2 Experimental

All experiments were performed on an *ApexII* Fourier-transform ion cyclotron resonance (FT-ICR) mass spectrometer (Bruker, Billerica, MA) equipped with a 4.7 or 9.4 T superconducting magnet and an external nanoelectrospray (nanoES) ion source. The ODNs were purchased from ACGT Corp. (Toronto, Canada) and used without further purification. The free nucleobases, AH and CH, were purchased from Sigma-Aldrich Co. (Oakville, Canada). To produce the gaseous ODN anions, nanoES was performed on 1:1 H_2O/CH_3CN solutions containing 200 μM ODN. To produce the noncovalent complexes of T_{20} with CH or AH, nanoES was performed on 1:1 H_2O/CH_3CN solutions containing 50 μM T_{20} and 50 μM AH or CH. NanoES tips were pulled from aluminosilicate tubes (1 mm o.d., 0.68 mm i.d.) using a P-2000 micropipette puller (Sutter Instruments, Novato, CA). A platinum (Pt) wire, inserted into the open end of the nanoES tip, was used to apply a potential of approximately –800 V to the nanoES solution. The tip was positioned 1 - 2 mm from a stainless steel sampling capillary using a microelectrode holder. The solution flow rate typically ranged from 60 to 100 nL/min depending on the diameter of the nanoES tip and the nanoES potential.

The droplets and gaseous ions produced by nanoES were introduced into the mass spectrometer through a heated stainless steel capillary (i.d. 0.42 mm) maintained at 62 °C. The ion/gas jet sampled by the capillary (-48 V) was transmitted through a skimmer (-1 V) and stored electrodynamically in an rf hexapole. Ions were accumulated in the hexapole for between 1 and 5 s, depending on the ion's size and the desired charge state, subsequently ejected and injected at ~2700 V into the bore of the superconducting magnet, decelerated and introduced into the ion cell. The trapping plates of the cell were maintained at a constant potential of -2 V throughout the experiments. The typical base pressure for the instrument was ~5 x 10^{-10} mbar. For the BIRD experiments, the temperature of the ion cell was controlled with two external flexible heating blankets placed around the vacuum tube in the vicinity of the ion cell [18]. Hydrogen/deuterium (H/D) exchange experiments were performed by introducing D_2O, at a static pressure (uncorrected) of 7 x 10^{-10} mbar, into the vacuum chamber. The ion cell temperature, and correspondingly the temperature of the deuterating agent inside the cell was approximately 22 °C. The H/D exchange experiments were performed exclusively at a magnetic field strength of 9.4 T. Mass spectra were acquired by an SGI R5000 computer running the Bruker Daltonics XMASS software, version 5.0.10. Isolation of the reactant ions for the BIRD and H/D exchange experiments was achieved using rf frequency excitation. The isolated ions were stored inside the heated cell for varying reaction times prior to excitation and detection. For the BIRD experiments the time-domain signal consisted of the sum of 20 transients containing 128 K data points per transient, while for H/D exchange experiments, with 512 K data points, The time domain signal was subjected to one zero-fill prior to Fourier transformation.

63

3.3 Results and Discussion

3.3.1 Dissociation Pathways of ODN Anions

NanoES of 1:1 $H_2O:CH_3CN$ solutions containing ~200 μM ODN (XT_{14}, XT_{19}, or $T_{19}X$, where X= A, C) produced predominantly the doubly and triply deprotonated ODN ions, $(M - 2H)^{-2} \equiv M^{-2}$ and $(M - 3H)^{-3} \equiv M^{-3}$, with the M^{-2} ions generally present at lower abundance, Figure 3.1. In certain cases, the M^{-4} and M^{-5} ions were also present at low abundance. Additionally, adducts corresponding to the attachment of alkali metals or phosphoric or acetic acid to the ODN anions were also sometimes observed.

BIRD was performed on the M^{-n} ions, where n = 2 and 3, at temperatures ranging from 80 to 190 °C. Representative BIRD spectra for each of the M^{-n} ions investigated are shown in Figure 3.2. The dissociation pathways observed for the 15- and 20-mers are consistent with the pathways previously identified for the dissociation of the corresponding XT_9^{-2} and T_9X^{-2} ions. Dissociation of the doubly and triply charged AT_m^{-n} ions, where m = 14 or 19, yielded product ions corresponding to the loss of neutral base, $(AT_m - AH)^{-n}$, and cleavage of the sugar 3' C-O bond, leading to w_{14}^{-n} and w_{19}^{-n} ions for AT_{14}^{-n} and AT_{19}^{-n}, respectively (eq 3.1a). Dissociation of the doubly and triply charged $T_{19}A^{-n}$ ions resulted in the formation of $(T_{19}A - AH)^{-n}$ and $(T_{19}A - AH - H_2O)^{-n}$ ions (eq 3.1b). For the C-containing ions, only the secondary fragment ions, w_m^{-n} and $(T_mC - CH - H_2O)^{-n}$, were present in the BIRD spectra. It was shown previously by double resonance experiments that the loss of neutral CH is the only primary dissociation channel for the C-containing T-rich 10-mers and that the absence of the $(XT_m - XH)^{-n}$ and $(T_mX - XH)^{-n}$ ions in the BIRD spectra is attributed to the slow dissociation kinetics for the loss of CH compared to the secondary dissociation processes [17]. There was no evidence for the

64

loss of neutral T in any of the BIRD spectra, consistent with previous BIRD studies of deprotonated ODN anions [14, 17].

$$XT_m^{-n} \rightarrow (XT_m - XH)^{-n} \rightarrow W_m^{-n} \qquad (3.1a)$$

$$T_mX^{-n} \rightarrow (T_mX - XH)^{-n} \rightarrow (T_mX - XH - H_2O)^{-n} \qquad (3.1b)$$
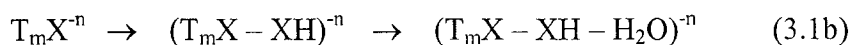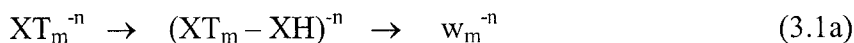
3.3.2   Dissociation Kinetics and Arrhenius Parameters for ODN Anions

The temperature dependent first-order rate constants (k) for the loss of neutral nucleobase were determined from the change in the natural log of the normalized intensity (abundance) of the ODN reactant ions ($I_{R,norm}$) with reaction time (eq 3.2). $I_{R,norm}$ was calculated using eq 3.3, where I_R is the abundance of the reactant ion and ΣI_P is the sum of the abundance of all product ions, including those produced by secondary reactions. Because of difficulties in accurately quantifying the low abundance isotopic peaks, within their respective isotope envelope for the reactant and product ions, due to poor signal-to-noise ratios, $I_{R,norm}$ was calculated using only the most abundant isotopic ion for the reactant and product ions. As noted previously [17], this approach leads to $I_{R,norm}$ values that are within 15% of the values obtained when all isotope peaks are considered. Illustrative kinetic plots obtained for $(CT_{14})^{-3}$, $(CT_{19})^{-3}$, and $(AT_{19})^{-3}$, at five different temperatures are shown in Figure 3.3. The plots are linear and exhibit near zero intercepts, as expected for simple first-order reactions. Plots of similar quality were obtained for all of the ODN anions investigated. The dissociation rate constant was determined from the slope of a linear least squares fit of the kinetic data obtained at each temperature investigated.

$$\ln (I_{R,norm,t}) = -kt \qquad (3.2)$$

$$I_{R,norm} = I_R / (I_R + \Sigma I_P) \qquad (3.3)$$
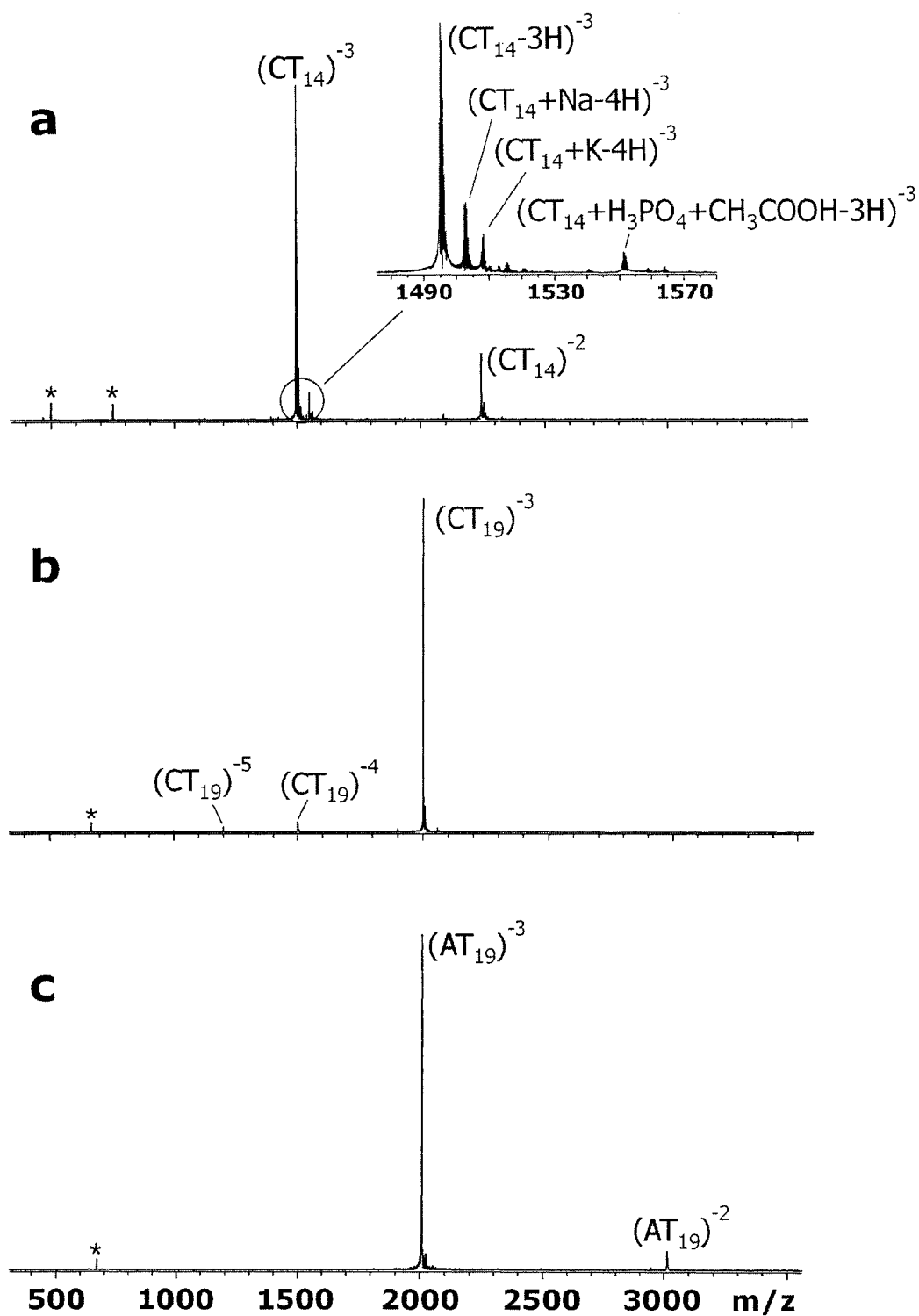
Figure 3.1 NanoES mass spectra of 1:1 $H_2O:CH_3CN$ solutions containing 200 μM (a) CT_{14}, (b) CT_{19}, (c) AT_{19}. The asterisk indicates a harmonic of the precursor ion [19].

66

67
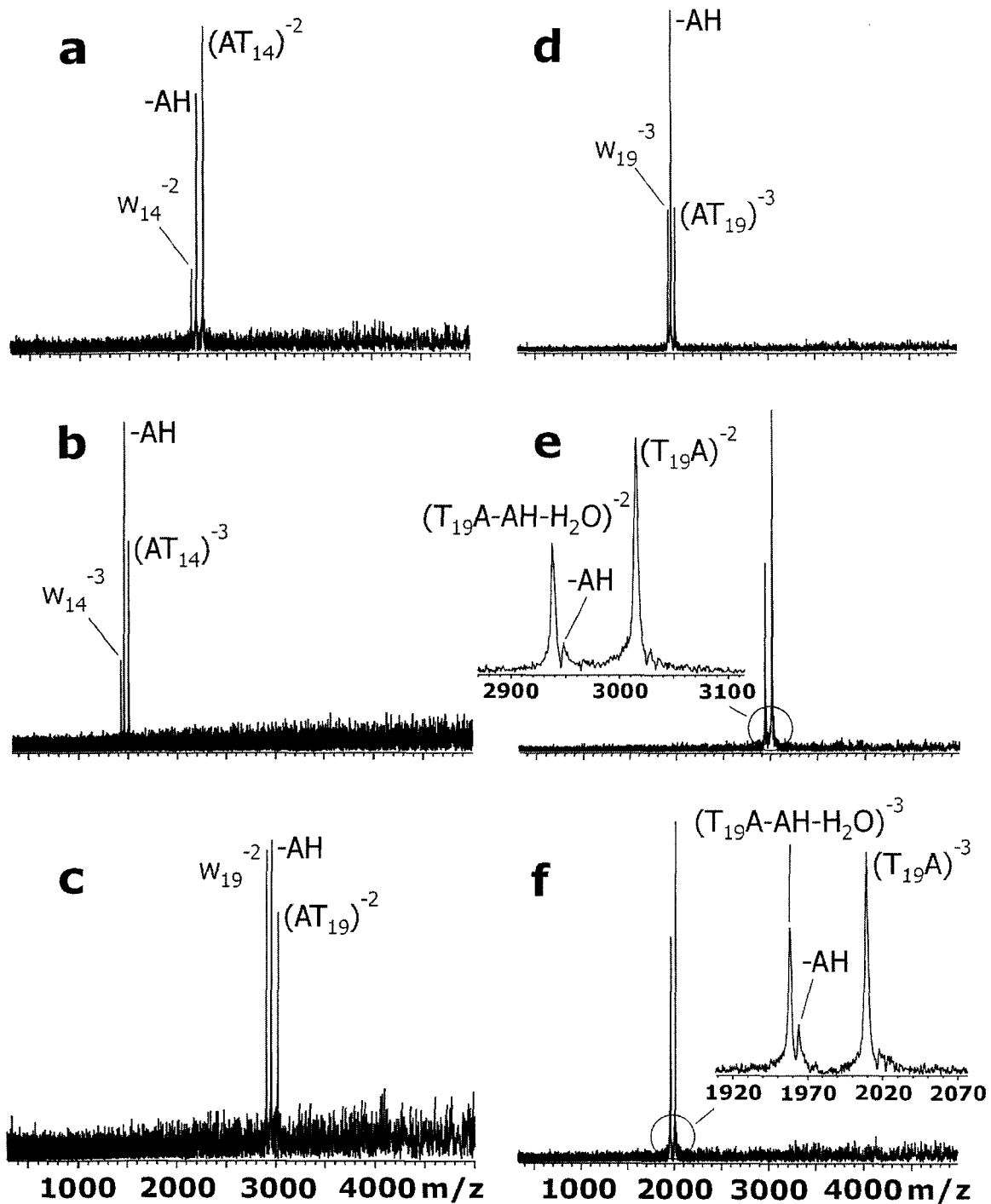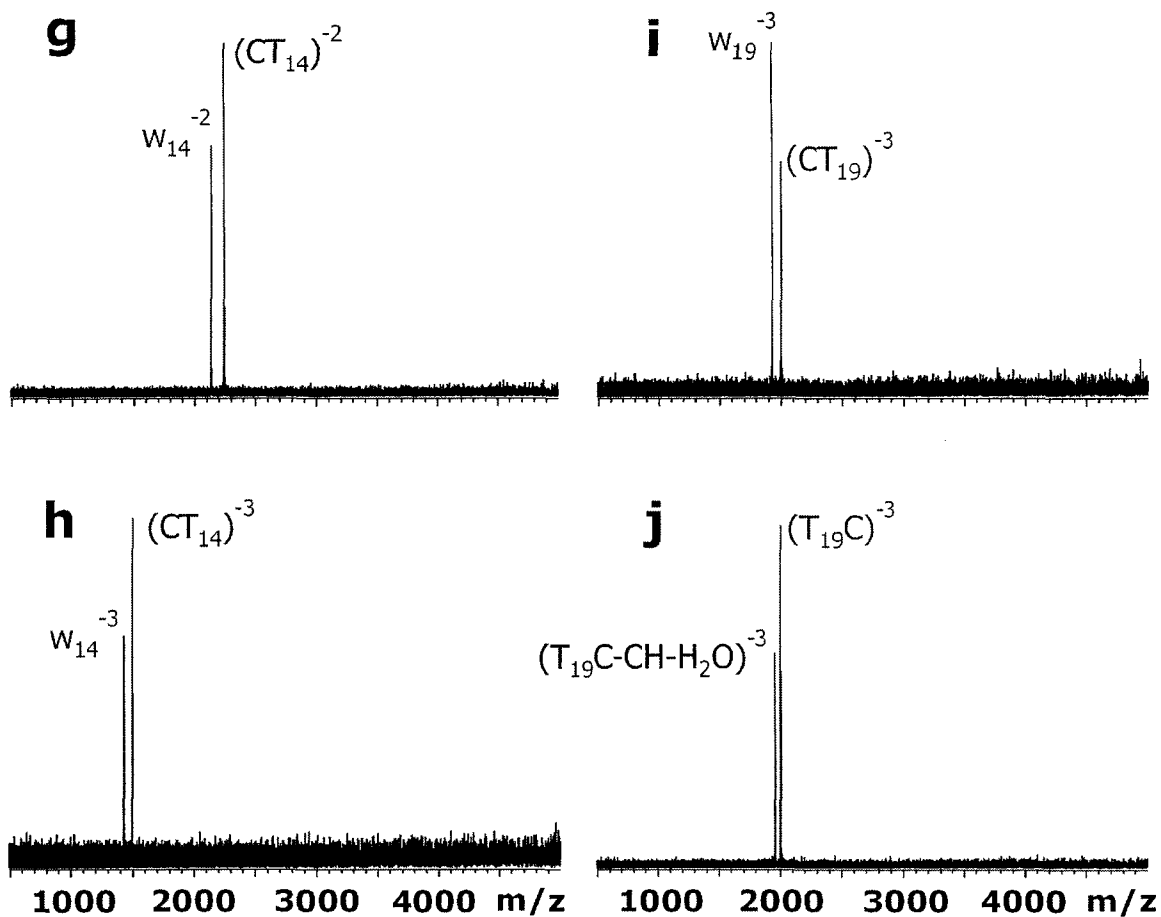
Figure 3.2 Blackbody infrared radiative dissociation spectra of doubly and triply deprotonated ODN anions (a) $(AT_{14})^{-2}$ at 98 °C and a reaction delay of 30 s, (b) $(AT_{14})^{-3}$ (100 °C, 20 s), (c) $(AT_{19})^{-2}$ (121.5 °C, 18 s), (d) $(AT_{19})^{-3}$ (135.5 °C, 2 s), (e) $(T_{19}A)^{-2}$ (121 °C, 6 s), (f) $(T_{19}A)^{-3}$ (134 °C, 1.25 s), (g) $(CT_{14})^{-2}$ (164.5 °C, 100 s), (h) $(CT_{14})^{-3}$ (164.5 °C, 100 s), (i) $(CT_{19})^{-3}$ (167.5 °C, 110 s), (j) $(T_{19}C)^{-3}$ (166 °C, 75 s).

68
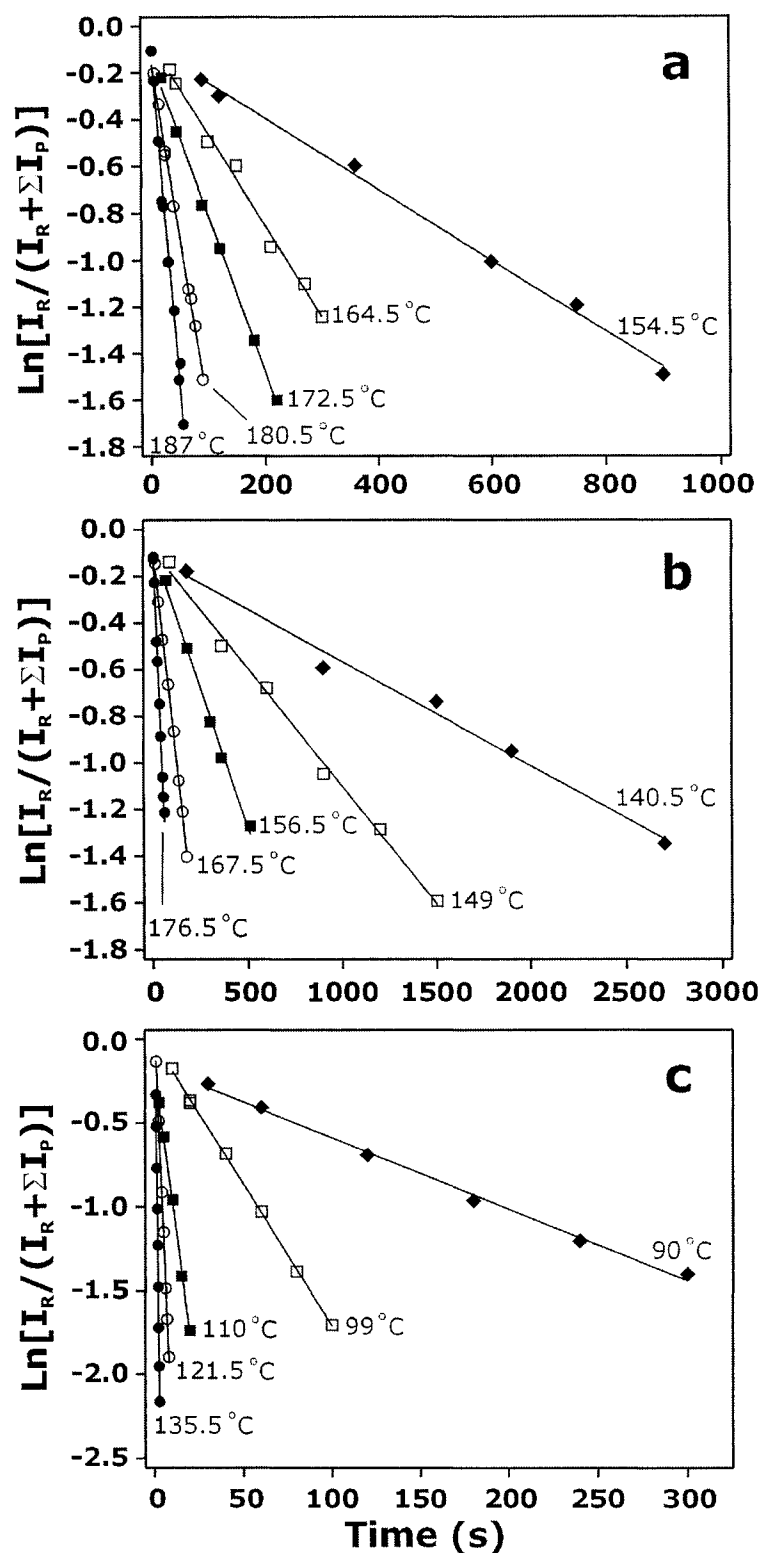
Figure 3.3 Dissociation kinetic data of (a) $(CT_{14})^{-3}$, (b) $(CT_{19})^{-3}$, (c) $(AT_{19})^{-3}$ obtained at the temperatures indicated.

69

Arrhenius plots constructed from the temperature dependent rate constants for the loss of nucleobase are shown in Figure 3.4. Reasonably linear Arrhenius plots were obtained for all of the ODN anions. The Arrhenius E_a and A-factor were obtained from the slopes and y-intercepts, respectively, of a linear least squares fit of the temperature dependent kinetic data and the values are listed in Table 3.1. Arrhenius parameters previously determined for T-rich 10-mer anions with a single reactive base are included for comparison purposes. Also included in Table 3.1 are values for the entropy of activation ($\Delta S^{\ddagger}$), calculated at a temperature of 150 °C from the corresponding A-factor using eq 3.4.

$$A = (ekT/h)\exp(\Delta S^{\ddagger}/R) \tag{3.4}$$

Inspection of Figure 3.4 reveals that, over the temperature range investigated, the C- containing compounds exhibit very similar dissociation kinetics while the A-containing ions exhibit a much broader range of reactivity. It can also be seen that loss of AH from the 15- and 20-mers is significantly faster that the loss of CH; ≥ 3000 times faster at 144 °C. The enhanced reactivity of the A-containing ions, compared to C-containing ions, is even more striking given the similarity in E_a values for their 20-mers, Table 3.1. It is also worth noting that the 15- and 20-mers all react faster than their corresponding 10-mers, i.e. the XT_9^{-2} and T_9X^{-2} ions [17]. The enhancement in reactivity is most pronounced for the A-containing ions, despite the larger E_a values for their 15- and 20-mers, compared with the 10-mers.

Inspection of the Arrhenius parameters in Table 3.1 reveals a striking difference in the dependence of the A and C base loss reactions on the size and charge state of the ODN anions. For the A-containing ions, the E_a values are very sensitive to the size of the

70
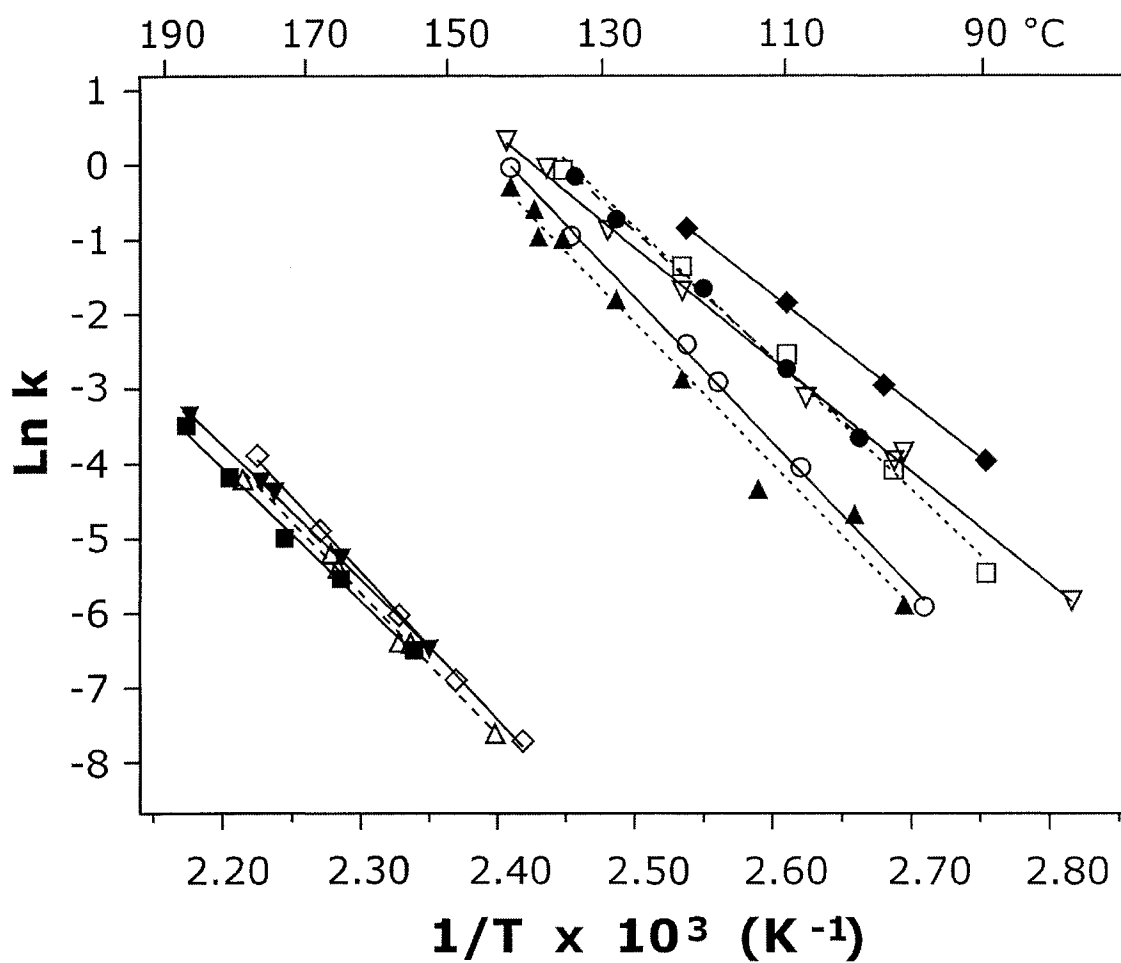
Figure 3.4 Arrhenius plots for the loss of neutral nucleobase from $(AT_{14})^{-2}$, (∇); $(AT_{14})^{-3}$, ($\blacklozenge$); $(AT_{19})^{-2}$, ($\blacktriangle$); $(AT_{19})^{-3}$, ($\square$); $(T_{19}A)^{-2}$, ($\circ$); $(T_{19}A)^{-3}$, ($\bullet$); $(CT_{14})^{-2}$, ($\blacktriangledown$); $(CT_{14})^{-3}$, ($\blacksquare$); $(CT_{19})^{-3}$, ($\lozenge$); $(T_{19}C)^{-3}$, ($\triangle$).

71

Table 3.1 Arrhenius activation parameters for the loss of neutral nucleobase from some doubly and triply deprotonated oligodeoxynucleotide anions containing a single reactive base.

Oligodeoxynucleotide	E_a (kcal mol^{-1}) [a]	A (s^{-1}) [a]	$\Delta S^{\ddagger}$ (cal mol^{-1} K^{-1}) [b]
$(AT_9\text{-}2H)^{-2}$	25.9 ± 0.2 [c]	$10^{12.1 \pm 0.1}$ [c]	-6
$(AT_{14}\text{-}2H)^{-2}$	29.7 ± 0.6	$10^{15.8 \pm 0.3}$	11
$(AT_{14}\text{-}3H)^{-3}$	28.8 ± 0.5	$10^{15.6 \pm 0.3}$	10
$(AT_{19}\text{-}2H)^{-2}$	37.8 ± 1.9	$10^{19.8 \pm 1.0}$	29
$(AT_{19}\text{-}3H)^{-3}$	34.9 ± 1.6	$10^{18.7 \pm 0.9}$	24
$(T_9A\text{-}2H)^{-2}$	23.0 ± 0.6 [c]	$10^{10.5 \pm 0.3}$ [c]	-13
$(T_{19}A\text{-}2H)^{-2}$	38.5 ± 0.6	$10^{20.2 \pm 0.4}$	31
$(T_{19}A\text{-}3H)^{-3}$	33.4 ± 0.7	$10^{17.9 \pm 0.4}$	21
$(CT_9\text{-}2H)^{-2}$	34.6 ± 1.1 [c]	$10^{14.1 \pm 0.6}$ [c]	3
$(CT_{14}\text{-}2H)^{-2}$	35.7 ± 0.6	$10^{15.5 \pm 0.3}$	10
$(CT_{14}\text{-}3H)^{-3}$	35.3 ± 1.7	$10^{15.2 \pm 0.8}$	8
$(CT_{19}\text{-}3H)^{-3}$	39.4 ± 1.0	$10^{17.4 \pm 0.5}$	18
$(T_9C\text{-}2H)^{-2}$	37.2 ± 2.3 [c]	$10^{14.6 \pm 1.1}$ [c]	6
$(T_{19}C\text{-}3H)^{-3}$	37.8 ± 1.3	$10^{16.5 \pm 0.7}$	14

a. Errors correspond to one standard deviation. b. $\Delta S^{\ddagger}$ values calculated at 423 K using eq 3.4. c. Arrhenius parameters taken from ref 17.

72

ODN. For example, for the AT_m^{-2} series, the E_a values increase from 25.9 (m = 9) to 29.7 (m = 14) to 37.8 kcal mol^{-1} (m = 19). A similar increase in E_a is found for T_mA^{-2} ions, from 23.0 (m = 9) to 38.5 kcal mol^{-1} (m = 19). An increase in charge state from, n = 2 to 3, for the AT_{19}^{-n} and $T_{19}A^{-n}$ ions results in a 5 kcal mol^{-1} decrease in E_a values. However, no such charge effect is found for the AT_{14}^{-n} anions, which exhibit similar E_a values. In contrast to the results obtained for the A-containing ODN anions, the E_a values for the C-containing ODN are relatively insensitive to size and charge state, with the exception of the CT_{19}^{-3} ion, which has an E_a value of 39 kcal mol^{-1}, the E_a values for the C-containing ODN fall within a 2 kcal mol^{-1} range, 35 to 37 kcal mol^{-1}. Interestingly, the position (5′ or 3′) of either the A or C nucleobase has only a small effect on the E_a values. This is an intriguing result given that it has been reported that fragmentation of ODN anions on the 3′ side of a T is generally enhanced compared to the 5′ side [1].

For the A-containing ODN ions, the A-factors fall in a broad range of values, 10^{10} - 10^{20} s^{-1}, which correspond to $\Delta S^{\ddagger}$ values of −13 to 31 cal mol^{-1} K^{-1}. For the C-containing ions, the A-factors and $\Delta S^{\ddagger}$ values span a smaller range, 10^{14} - 10^{17} s^{-1} and 6 - 18 cal mol^{-1} K^{-1}, respectively. To put these values into perspective it is useful to compare them with values reported for covalent bond cleavage reactions. For simple homolytic bond fission in small molecules, A-factors of 10^{14} to 10^{17} s^{-1} are typical, while values of $<10^{13}$ s^{-1} are generally associated with complex bond cleavage reactions involving cyclic transition states [20]. The A-factors for the loss of CH are similar to values expected for simple bond fission, which is consistent with cleavage of the N-glycosidic bond as the rate limiting step for neutral base loss. For the A-containing 10-mers, the relatively small A-factors suggest that the rate limiting step for the base loss reaction involves simultaneous

73

bond cleavage and bond formation (*i.e.* a relatively tight transition state), while for the 15-mers, the A-factors are more consistent with simple bond fission. The large A-factors determined for the 20-mers cannot be explained simply in terms of covalent bond cleavage. Large A-factors, $>10^{18}$ s^{-1}, have previously only been reported for the dissociation of noncovalent biological complexes such as protein-carbohydrate and multiprotein complexes [18, 21, 22]. It has been suggested that these large A-factors arise from the softening of numerous vibrational modes upon cleavage of the stabilizing noncovalent intermolecular interactions [21]. The large A-factors determined for the 20-mers suggest, therefore, that the loss of AH is accompanied by the cleavage of multiple noncovalent interactions, likely involving solvation of the nucleobase. As described below, there is also evidence that internal solvation of the reactive nucleobase influences the Arrhenius parameters for the smaller A-containing ODN anions.

It is interesting to note that, for both the A- and C-containing ODN ions, the E_a and A values are highly correlated. However, the relationship between the E_a and A values is different for the two sets of ODN ions. For the A-containing ions, the average $E_a/\log A$ ratio is 1.9 ± 0.1, while for the C ions, the average ratio is 2.3 ± 0.1. The difference in $E_a/\log A$ ratios determined for the loss of AH and CH indicates that, for a given E_a, the base loss reaction is inherently more favourable entropically for AH. Notably, the ratios determined for the A-containing ions are similar to those found for the dissociation of noncovalent protein-carbohydrate and multiprotein complexes in the gas phase. From an analysis of the Arrhenius parameters reported for the dissociation of protein complexes, the average $E_a/\log A$ value is found to be 2.0 ± 0.1 [23]. The origin of the correlation of E_a and A values for the protein complexes remains a matter of debate

74

[18, 24]. Although artifacts arising from the statistical treatment of the kinetic data may obscure the true nature of the correlation, such energy-entropy correlation is thought to be an inherent characteristic of complexes stabilized by multiple, weak interactions (*e.g.* hydrogen bonds) [25]. The similarity in E_a/log$A$ ratios for the A-containing ODN anions and the protein complexes further suggests that loss of AH requires the cleavage of noncovalent interactions. In contrast, the larger E_a/log$A$ ratios found for the C-containing ions are more consistent with a reaction involving simple covalent bond cleavage (*i.e.* cleavage of the glycosidic linkage), than with noncovalent bond cleavage. That is not to say that C is not internally solvated, rather that covalent bond cleavage represents the dominant energetic and entropic contributions to the Arrhenius parameters. It should be noted that this conclusion is at odds with the suggestion made in our previous study of the dissociation of the T-rich 10-mers that C enjoys greater internal solvation that A or G [17].

The differential internal solvation of A and C within the T-rich ODN anions provides a reasonable explanation for the observed dependence of the E_a and A values with ODN size and charge state. As the A-containing ions get bigger and, presumably, conformationally more flexible, the intramolecular solvation of A might be expected to be enhanced and lead to larger Arrhenius parameters. Furthermore, the smaller E_a and A values for the triply charged AT_{19} and $T_{19}A$ ions, compared to the doubly charged ions, is consistent with reduced base solvation with increasing charge state due to Coulombic repulsion, which is expected to cause the ions to adopt more extended conformations [26]. In contrast, the limited sensitivity of the Arrhenius parameters for the loss of CH to size and charge state of the ODN is consistent with a simple covalent bond cleavage

75

reaction (*i.e.* heterolytic cleavage of the glycosidic linkage) with little or no contribution from intramolecular interactions.

The above interpretation of the Arrhenius parameters, if correct, may provide new insight into the relative strength of the N-glycosidic linkages for A and C. If the Arrhenius parameters for the loss of AH correspond predominantly to the cleavage of noncovalent interactions stabilizing the nucleobase and that the extent of base solvation decreases with decreasing length of the ODN, then for sufficiently small strands, the dissociation E_a value should reflect the N-glycosidic bond cleavage process, with little or no contribution from solvation effects. In the absence of parameters for A-containing ODN anions shorter than 10-mers, the values obtained for the 10-mers in the previous BIRD study, ~23 kcal mol^{-1}, may be taken as the upper limit for the E_a for glycosidic bond cleavage for A. In contrast, the E_a values determined for the loss of CH, ~35 kcal mol^{-1}, do not appear to be significantly influenced by internal solvation of nucleobase and may reflect the energy required to cleave the glycosidic bond.

While the above analysis of the Arrhenius parameters does not provide any direct insight into the mechanism of base loss from gaseous ODN anions, it is interesting to note the similarities between the relative reactivity and E_a values of A and C in the gas phase and in solution. It is well established that depurination (loss of AH or GH) of DNA is kinetically more facile that depyrimidination (loss of TH or CH) in aqueous solution [27]. The differential reactivity of A and C reflects, at least in part, a difference in the E_a for glycosidic bond cleavage, 31 kcal mol^{-1} for A [28] and 35 kcal mol^{-1} for C [29]. In solution, the base loss reaction is believed to be acid catalyzed, with protonation of the nucleobase resulting in a weakening of the glycosidic bond. Interestingly, an analogous

76

acid catalysis mechanism has been proposed for the base loss reactions in the gas phase by Gross and coworkers [16]. According to this mechanism, the nucleobase is charged by proton transfer from an adjacent phosphate group prior to cleavage of the glycosidic bond. The similarities between the relative reactivity and E_a values in solution and gas phase are consistent with this acid catalyzed base loss mechanism.

3.3.3 Hydrogen/Deuterium Exchange

Gas phase H/D exchange is a promising technique for identifying differences in the higher order structure of biopolymers [30-32]. For example, differences in H/D exchange rates have been measured for protein ions generated by ES from native and denaturing conditions [30]. H/D exchange has also been used to monitor time-dependent structural changes in ODN anions in the gas phase [33, 34]. Studies of H/D exchange of mono- and oligonucleotides anions have suggested that exchange involves inter- and intramolecular proton transfer involving the phosphate groups [35]. It has also been shown that the presence of internal hydrogen bonds within the ODN anions slows down the rate of exchange [33, 35]. Therefore, differences in base solvation in the T-rich ODN ions investigated in the present study may lead to differences in the rate of exchange. In addition to possible base stacking, the intramolecular solvation of the nucleobases within the ODN anions is expected to involve neutral and ionic hydrogen bonds with other nucleobases, phosphate groups and deoxyribose OH groups [35, 36]. As such, the differential solvation of A and C in the larger T-rich ODN anions (in particular the 20-mers) predicted by the BIRD experiments might be revealed by gas phase H/D exchange experiments.

77

To investigate whether conformational differences among the A- and C-containing 20-mers could be identified using gas phase H/D exchange, experiments were carried out on the triply deprotonated AT_{19}^{-3}, $T_{19}A^{-3}$, CT_{19}^{-3}, and $T_{19}C^{-3}$ anions using D_2O as the deuterating agent. The number of the exchangeable hydrogens within the neutral 20-mers, associated with different functional groups, is listed in Table 3.2. It can be seen that each triply deprotonated ion possesses 39 possible exchangeable hydrogens, belonging to the imino, amino, hydroxyl and phosphate groups, with A and C each possessing 2 amino hydrogens. After isolating their naturally occurring isotopes, each of the four ions were allowed to react with D_2O for 300, 600 and 900 s. Shown in Figure 3.5 are mass spectra obtained for each of the four ions at each time interval. Reported in Table 3.3 is the change in average mass of the ODN anions due to the incorporation of deuterons in each exchange-time interval. The weighted average mass, m_{ave}, at each time interval was calculated using eq 3.5:

$$m_{ave} = \sum f_i m_i \tag{3.5}$$

where m_i and f_i are the mass and fractional abundance, respectively, of the ODN isotopes. The change in average mass, Δm, is given by eq 3.6:

$$\Delta m(t) = m_{ave}(t) - m_{ave}(0) \tag{3.6}$$

where $m_{ave}(0)$ is the average mass at time zero, i.e. the average mass of the naturally occurring isotopes of the ODN, and $m_{ave}(t)$ is the average mass measured at time t.

From a comparison of the mass spectra in Figure 3.5, it can be seen that the extent of exchange for the XT_{19}^{-3} and $T_{19}X^{-3}$ anions is sensitive to the nature of X. Although, the mass spectra for the AT_{19}^{-3} and $T_{19}C^{-3}$ ions are qualitatively similar in appearance, as are the spectra for CT_{19}^{-3} and $T_{19}A^{-3}$. Inspection of the average change in mass of the ODN

78

Table 3.2 Number and type of exchangeable hydrogens found within the 20-mers: AT_{19}, $T_{19}A$, CT_{19}, $T_{19}C$.

ODN	$-PO_3H$	$-OH$	$-NH$	$-NH_2$	Total
AT_{19}	19	2	19	2	42
$T_{19}A$	19	2	19	2	42
CT_{19}	19	2	19	2	42
$T_{19}C$	19	2	19	2	42

79
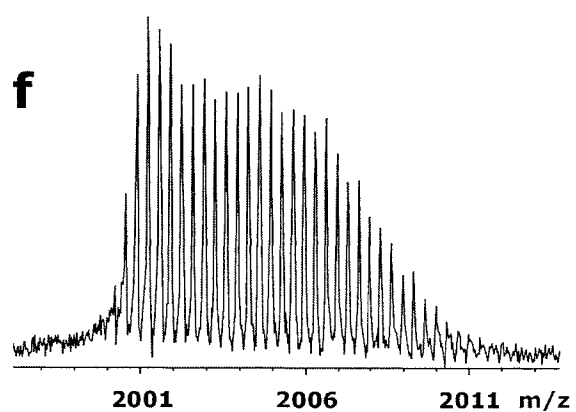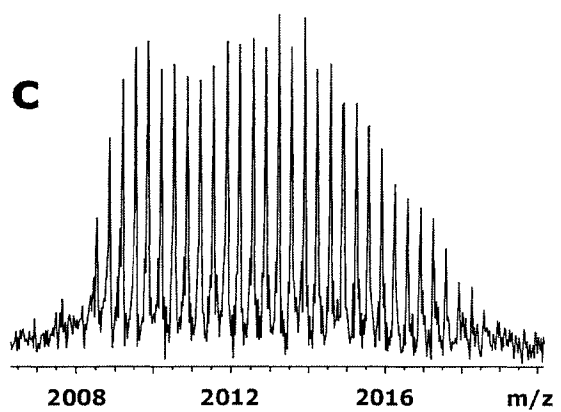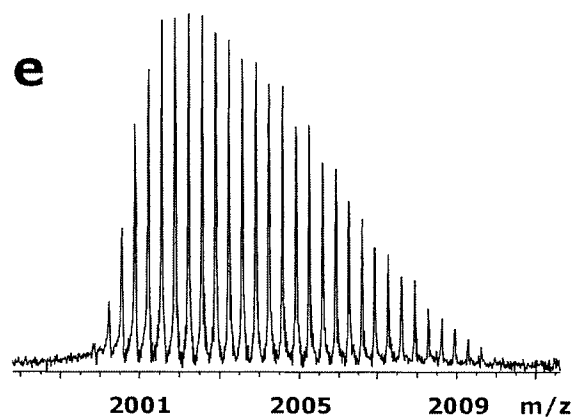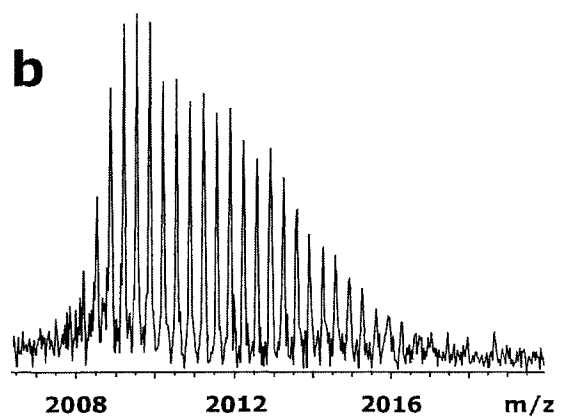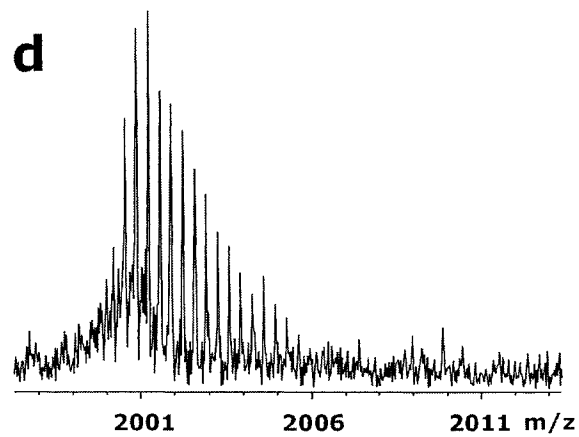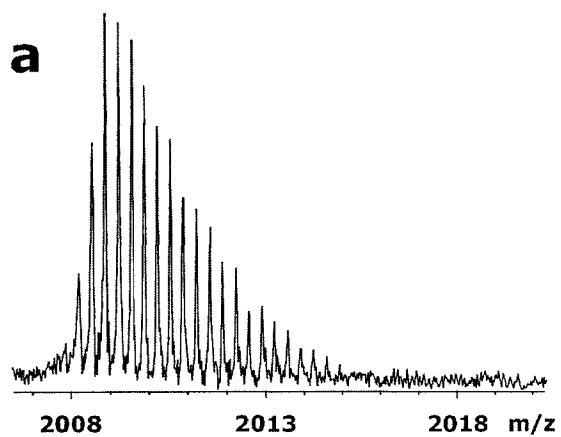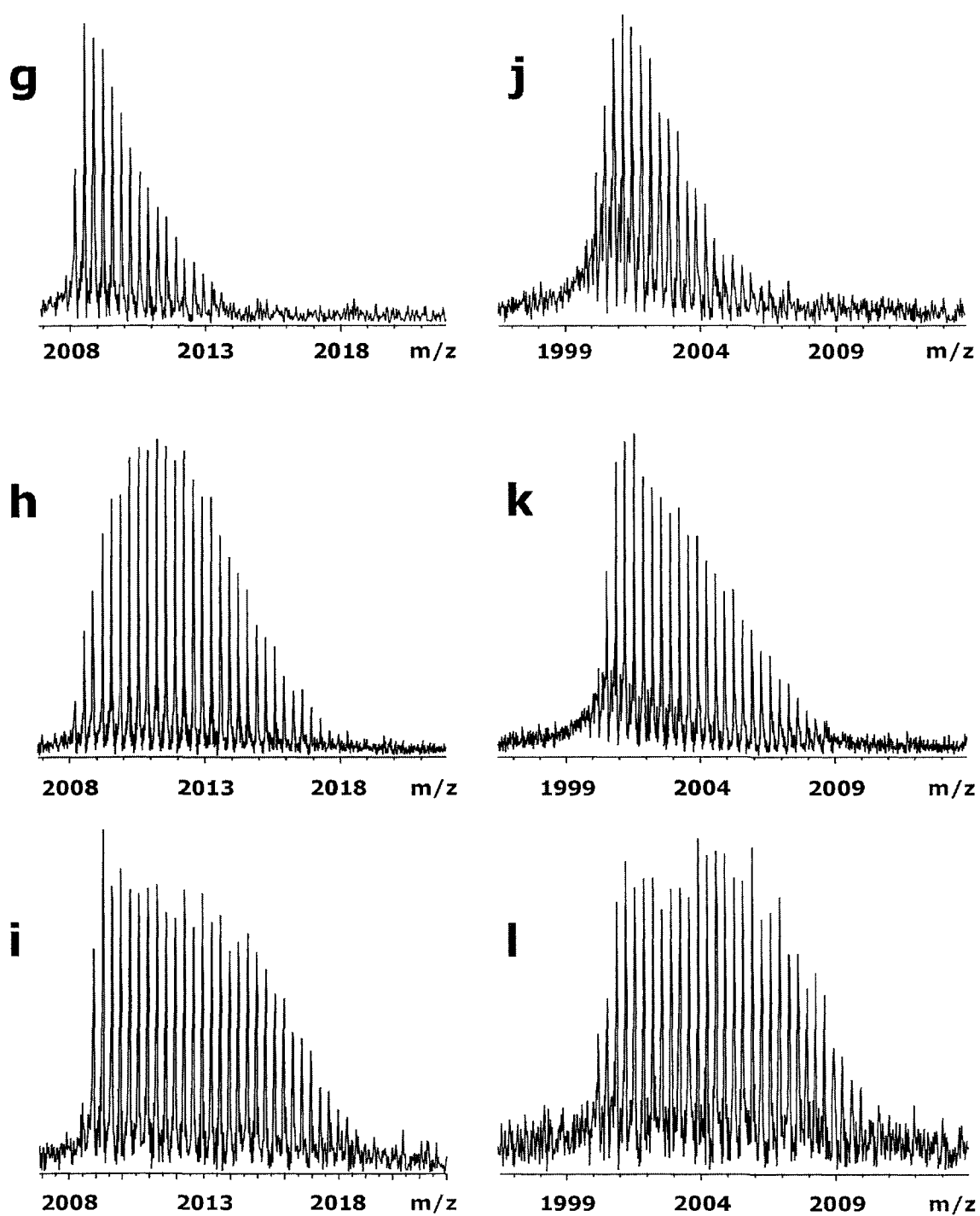
Figure 3.5 H/D exchange mass spectra of $(AT_{19})^{-3}$ at (a) 300 s, (b) 600s, (c) 900s, $(CT_{19})^{-3}$ at (d) 300 s, (e) 600 s, (f) 900s, $(T_{19}A)^{-3}$ at (g) 300 s, (h) 600 s, (i) 900, and $(T_{19}C)^{-3}$ at (j) 300 s, (k) 600s, (l) 900 s.

81

Table 3.3 Average number of exchanged hydrogen as a function of exchange time.[a,b]

ODN anion	300 s	600 s	900 s
$(AT_{19})^{-3}$	4.7	7.7	10.1
$(CT_{19})^{-3}$	4.1	9.0	11.2
$(T_{19}A)^{-3}$	3.5	9.8	11.7
$(T_{19}C)^{-3}$	5.2	8.4	12.2

a. Calculated from eq 3.5 and 3.6. b. D_2O was used as exchange reagent at a static pressure of 7.0×10^{-10} mbar (uncorrected).

ions reveals that the differences in exchange rates are, overall, small, and that the trend in the Δm values are sensitive to the time interval. At 300 s, the Δm values range from 3.5 $(T_{19}A^{-3})$ to 5.2 $(T_{19}C^{-3})$, at 600 s the values range from 7.7 (AT_{19}^{-3}) to 9.8 $(T_{19}A^{-3})$ while at 900 s the values range from 10.1 (AT_{19}^{-3}) to 12.2 $(T_{19}C^{-3})$. Importantly, the trend in the Δm values are not consistent with inherent differences in the degree of internal solvation within the A- and C-containing ODN anions, as suggested by the BIRD experiments. The time dependence on the relative rate of exchange observed for the different ODN anions is consistent with results reported by Hofstadler and coworkers [34].

The H/D exchange experiments performed on the AT_{19}^{-3}, $T_{19}A^{-3}$, CT_{19}^{-3}, and $T_{19}C^{-3}$ anions revealed that the nature and position of the nucleobase do influence the rate of exchange, at a given time interval. However, the results, by themselves, do not provide evidence of greater internal solvation within the A-containing ODN ions compared to the C-containing ions.

3.3.4 BIRD of Noncovalent $(T_{20} + XH)^{-3}$ Complexes

The BIRD experiments, if not the H/D exchange experiments, suggest that there are differences in the higher order structures of A- and C-containing T-rich ODN anions. These structural differences are attributed, at least in part, to inherent differences in the internal solvation of the covalently bound A and C bases within the anions. It was also of interest to establish whether the A and C bases, when bound noncovalently to T-rich ODN anions, exhibit differences in intermolecular solvation. To address this question, BIRD was performed on the complexes of triply deprotonated T_{20} and AH or CH, *i.e.* $(T_{20} + XH)^{-3}$. The noncovalent complexes were produced by performing nanoES on solutions containing T_{20} and the nucleobase AH or CH at relatively high concentration

83

($\sim$50 μM). Dissociation of the $(T_{20} + XH)^{-3}$ complexes proceeds exclusively by the loss of the neutral base (XH), eq 3.7.

$$(T_{20} + XH)^{-3} \rightarrow T_{20}^{-3} + XH \qquad (3.7)$$

Shown in Figure 3.6 are kinetic plots obtained at several temperatures for the dissociation of the $(T_{20} + AH)^{-3}$ and $(T_{20} + CH)^{-3}$ ions. The plots are linear and, except at the lowest temperatures investigated, exhibit near zero intercepts. Shown in Figure 3.7 are the Arrhenius plots constructed from the temperature dependent dissociation rate constants.

It can be seen that the kinetic and energetic stabilities of the $(T_{20} + AH)^{-3}$ and $(T_{20} + CH)^{-3}$ ions are very different. Over the range of temperatures investigated, $(T_{20} + AH)^{-3}$ is at least 7 times more reactive than $(T_{20} + CH)^{-3}$. The lower kinetic stability of $(T_{20} + AH)^{-3}$ coincides with significantly smaller E_a and A values, 19.8 $\pm$ 1.0 kcal mol^{-1} and $10^{11.3 \pm 0.6}$ s^{-1}, compared to $(T_{20} + CH)^{-3}$, 34.9 $\pm$ 1.3 kcal mol^{-1} and $10^{18.4 \pm 0.7}$ s^{-1}. Taken on their own, the Arrhenius parameters suggest that there are significant differences in how the two bases interact with T_{20}^{-3}. While these structural differences can not be positively identified from the dissociation data, it is possible to speculate on the nature of the interactions. Primary sites of interaction of the free base with the T_{20}^{-3} ion may include one of the deprotonated phosphate groups or one (or more) of the neutral thymine bases. Given that the nucleobases are relatively acidic in the gas phase (ΔH_{acid}(AH) = 327 kcal mol^{-1}, ΔH_{acid}(CH) = 337 kcal mol^{-1} [6]), the energetically preferred site of interaction might be one of the charged phosphate groups (ΔH_{acid}((CH$_3$)$_2$PO$_4$H) = 321 kcal mol^{-1} [37]). Because the difference in acidity between the phosphate group and AH is less than the difference for CH, AH would be expected to form the strongest ionic hydrogen bond.

84
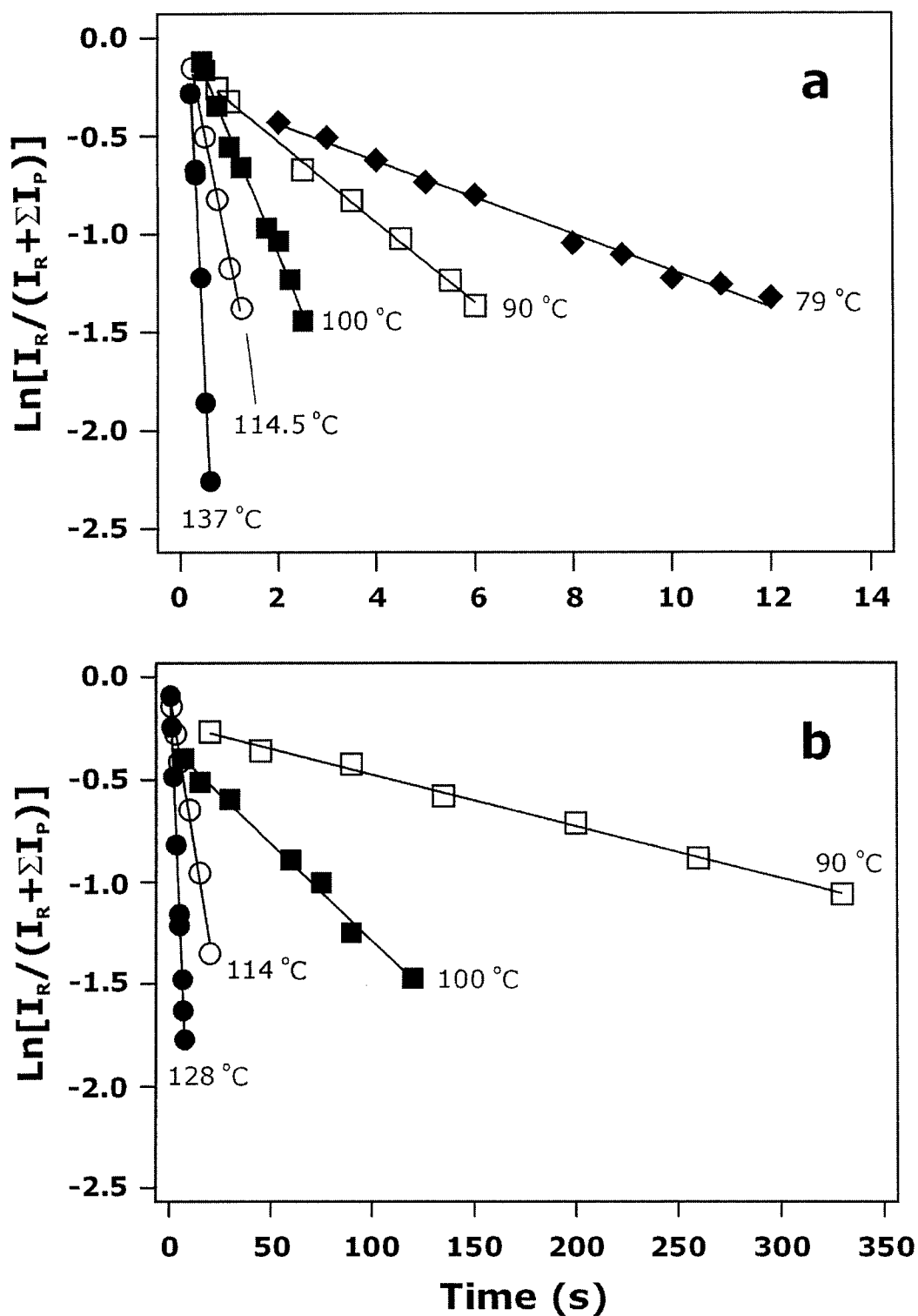
Figure 3.6 Kinetic data, obtained at the temperatures indicated, for the dissociation of the $(T_{20} + XH)^{-3}$ complexes into T_{20}^{-3} and XH; (a) $(T_{20} + AH)^{-3}$ and (b) $(T_{20} + CH)^{-3}$.

85
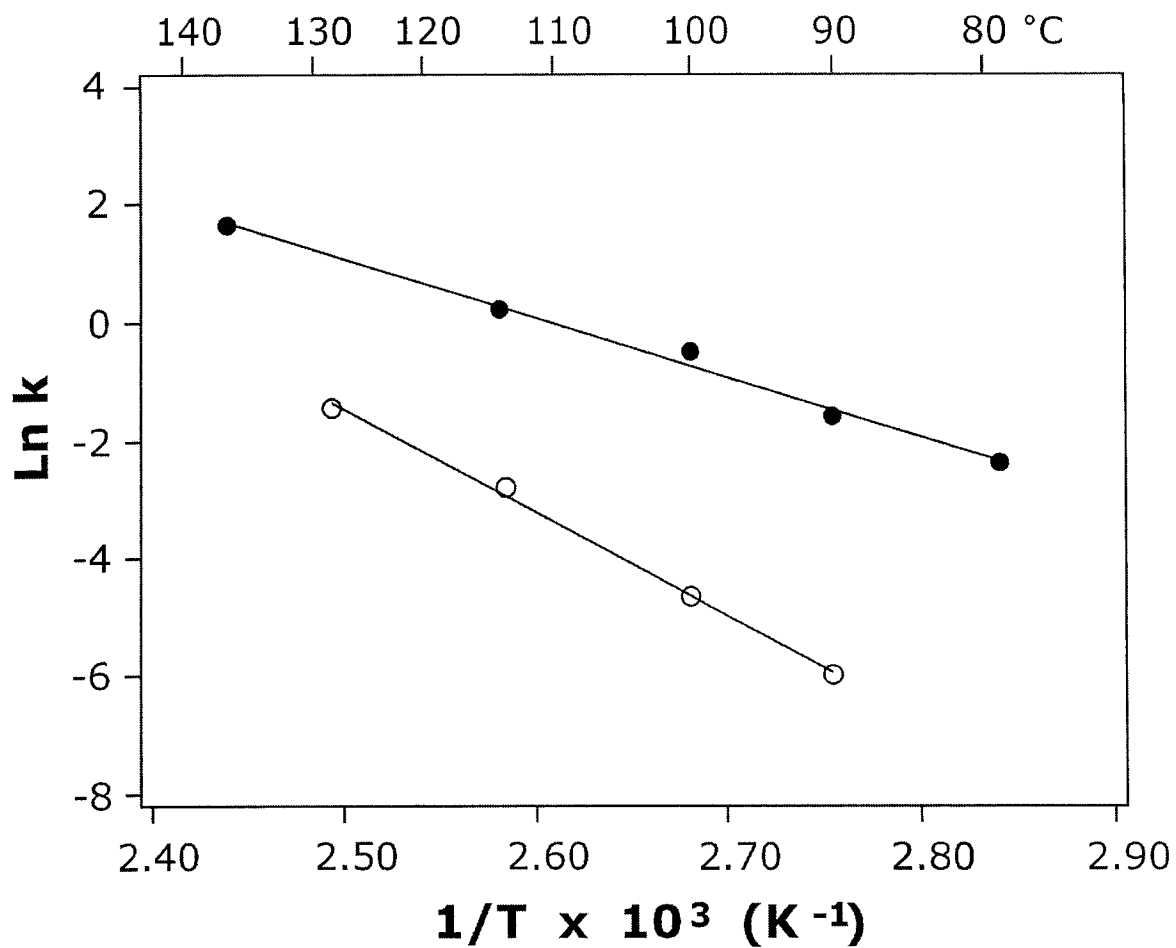
Figure 3.7 Arrhenius plots for the dissociation of the $(T_{20} + XH)^{-3}$ complexes into T_{20}^{-3} and XH; $(T_{20} + AH)^{-3}$, ($\bullet$) and $(T_{20} + CH)^{-3}$, ($\circ$).

86

However, this is not consistent with the experimental results. One possible explanation for this is that CH participates in additional hydrogen bonds with the same phosphate group or with adjacent phosphate groups. To our knowledge, Arrhenius parameters for the dissociation of noncovalent complexes of deprotonated phosphate groups and small neutral molecules have not been reported. Williams and coworkers have estimated the dissociation threshold energy for the $H_3PO_4 \bullet H_2PO_4^-$ complex to be approximately 30 kcal mol^{-1} [38]. However, it is difficult to compare this value directly with the present E_a values because H_3PO_4 is more acidic than AH or CH and can, in principle, form a stronger ionic hydrogen bond than either of the nucleobases. Furthermore, the $H_3PO_4 \bullet H_2PO_4^-$ complex is likely stabilized by multiple intermolecular hydrogen bonds, which may not be the case for AH or CH. A second possible site of interaction of the free bases is one of the neutral T bases. According to theoretical calculations of the hydrogen bond energy for DNA base pairs in the gas phase, the interaction of TH with AH is energetically more favourable, by several kcal mol^{-1}, than is the interaction with CH. This is true even when considering only the hydrogen bonds that are possible within the $(T_{20} + XH)^{-3}$ complexes. According to the most recent DFT calculations, the A-T interaction energy may be as large as 17 kcal mol^{-1} [39]. Based on the similarity between the theoretical A-T interaction energy value and the experimental dissociation E_a for the $(T_{20} + AH)^{-3}$ complex, ~20 kcal mol^{-1}, the possibility of neutral A-T interactions in the $(T_{20} + AH)^{-3}$ complex cannot be ruled out. However, for the $(T_{20} + CH)^{-3}$ complex, the large E_a is inconsistent with simple C-T interaction. More likely, CH interacts at a charged phosphate group with, perhaps, additional hydrogen bonding interactions contributing to the stability of the complex.

87

The present results suggest different interaction sites for AH and CH within the $(T_{20} + XH)^{-3}$ complexes. Given that solvation of a deprotonated phosphate group would be expected to be, energetically, the most favourable intermolecular interaction for both AH and CH, this result is intriguing. A possible explanation for the alternative binding site in the case of the $(T_{20} + AH)^{-3}$ complex would be that the base-base (A-T) interactions were present in solution and were nominally preserved upon transfer to the gas phase. In other words, the A and T bases engage in specific H-bonding in solution and the interactions become "kinetically" trapped in the gas phase. Some support for this explanation can be found in a study reported by Gokel and coworkers [40]. Using ES/MS, the interactions between diaza-18-crown 6 derivatives with two sidearms terminating in either adenine (referred to as AOA) or thymine (TOT) in a solution of CH_3Cl/CH_3OH were investigated. The authors observed the preferential formation of the protonated complex TOT-AOA, a result that suggests specific base-base interactions in solution. In contrast, the $(T_{20} + CH)^{-3}$ complex is likely produced from nonspecific interactions during the nanoES process. With no pre-organization of the structure of the complex, the base is likely able to migrate to the preferred site of interaction, *i.e.* the deprotonated phosphate group, in the gas phase.

3.4 Conclusions

The present work details the application of the BIRD technique to study thermal decomposition of a series of T-rich doubly and triply deprotonated 15- and 20-mer ODN anions containing a single reactive nucleobase (A or C). From the temperature dependence of the dissociation kinetics, Arrhenius activation parameters for the loss of

88

neutral nucleobase from the ODN anions have been determined. In agreement with an earlier study of doubly deprotonated 10-mer ODN anions, the A-containing ODN anions are significantly more reactive ($\geq$3000 times at 144 °C) than the C-containing ions. Interestingly, the Arrhenius activation parameters for the loss of base from the C-containing ions are relatively insensitive to the size and charge state of the ODN. In contrast, the parameters for the loss of base from the A-containing ions exhibit a strong dependence on size and, to some extent, charge state, with the parameters increasing with size and charge state. The A-factors for the loss of CH, which are in the range of 10^{15} - 10^{17} s^{-1}, are consistent with simple bond cleavage as the rate limiting step. The A-factors for the loss of AH increase with increasing size, 10^{11} - 10^{12} s^{-1} (10-mers), 10^{15} - 10^{16} s^{-1} (15-mers) and 10^{18} - 10^{20} s^{-1} (20-mers), suggesting increased internal solvation of the reactive base with increasing size of the ODN anions.

The inherent differences in intramolecular solvation of A and C within the ODN anions was further probed with gas phase H/D exchange experiments, which were performed on AT_{19}^{-3}, $T_{19}A^{-3}$, CT_{19}^{-3}, and $T_{19}C^{-3}$ anions using D_2O as the deuterating agent. The extent of exchange for the four ions exhibited a subtle dependence on the sequence of the ODN anions. However, the exchange results by themselves did not provide evidence for inherent differences in the internal solvation of A and C within the T-rich ODN anions.

BIRD was also performed on noncovalent complexes formed between T_{20}^{-3} and AH or CH, *i.e.* $(T_{20} + XH)^{-3}$. Dissociation of complexes was found to proceed exclusively by the loss of XH. Interestingly, the nature of the noncovalently bound nucleobase had a significant influence on the magnitude of the Arrhenius parameters, 20 kcal mol^{-1} and

89

10^{11} s^{-1} for $(T_{20} + AH)^{-3}$ compared with 35 kcal mol^{-1} and 10^{18} s^{-1} for $(T_{20} + CH)^{-3}$. The difference in the Arrhenius parameters indicates significant differences in the nature of the intermolecular interactions. It is speculated that in the $(T_{20} + CH)^{-3}$ complex, which is likely formed via nonspecific interactions during the nanoES process, the CH interacts at a charged phosphate group with, perhaps, additional hydrogen bonding interactions contributing to the stability of the complex. In contrast, specific A-T hydrogen bonding in solution may lead to a gaseous $(T_{20} + AH)^{-3}$ complex in which the AH interacts with T residues, instead of a charged phosphate group.

90

3.5 Literature Cited

(1)   Hofstadler, S. A.; Sannes-Lowry, K. A.; Hannis J. C. *Mass Spectrom. Rev.* **2005**, *24*, 265-285.

(2)   McLuckey, S. A.; Van Berkel, G. J.; Glish, G. L. *J. Am. Soc. Mass Spectrom.* **1992**, *3*, 60-70.

(3)   Wan, K. X.; Gross, M. L. *J. Am. Soc. Mass Spectrom.* **2001**, *12*, 580-589.

(4)   Wan, K. X.; Gross, J.; Hillenkamp, F.; Gross, M. L. *J. Am. Soc. Mass Spectrom.* **2001**, *12*, 193-205.

(5)   McLuckey, S. A.; Habibi-Goudarzi, S. *J. Am. Chem. Soc.* **1993**, *115*, 12085-12095.

(6)   Freitas, M. A.; Shi, S. D.-H.; Hendrickson, C. L.; Marshall, A. G. *J. Am. Chem. Soc.* **1998**, *120*, 10187-10193.

(7)   McLuckey, S. A.; Vaidyanathan, G. *Int. J. Mass Spectrom. Ion Processes* **1997**, *162*, 1-16.

(8)   Little, D. P.; Aaserud, D. J.; Valaskovic, G. A.; McLafferty, F. W. *J. Am. Chem. Soc.* **1996**, *118*, 9352-9359.

(9)   Luo, H.; Lipton, M. S.; Smith, R. D. *J. Am. Soc. Mass Spectrom.* **2002**, *13*, 195-199.

(10) Hannis, J. C.; Muddiman, D. C. *Int. J. Mass Spectrom.* **2002**, *219*, 139-150.

(11) Zhu, L.; Parr, G. R.; Fitzgerald, M. C.; Nelson, C. M.; Smith, L. M. *J. Am. Chem. Soc.* **1995**, *117*, 6048-6056.

(12) McLuckey, S. A.; Vaidyanathan, G.; Habibi-Goudarzi, S. *J. Mass Spectrom.* **1995**, *30*, 1222-1229.

(13)   Aaserud, D. J.; Guan, Z.; Little, D. P.; McLafferty, F. W. *Int. J. Mass Spectrom. Ion Processes* **1997**, *167/168*, 705-7012.

(14)   Klassen, J. S.; Schnier, P. D.; Williams, E. R. *J. Am. Soc. Mass Spectrom.* **1998**, *9*, 1117 – 1124.

(15)   Lotz, R.; Gerster, M.; Bayer, E. *Rapid Commun. Mass Spectrom.* **1998**, *12*, 389-397.

(16)   Wang, Z.; Wan, K. X.; Ramanathan, R.; Taylor, J. S.; Gross, M. L. *J. Am. Soc. Mass Spectrom.* **1998**, *9*, 683-691.

(17)   Daneshfar, R.; Klassen, J. S. *J. Am. Soc. Mass Spectrom.* **2004**, *15*, 55-64.

(18)   Felitsyn, N.; Kitova, E. N.; Klassen, J. S. *Anal. Chem.* **2001**, *73*, 4647-4661.

(19)   Marshall, A. G.; Grosshans, P. B. *Anal. Chem.* **1991**, *63*, 215A-229A.

(20)   Benson, S. W. *Thermochemical Kinetics. Methods for the Estimation of Thermochemical data and Rate Parameters*; Wiley: New York, 1968.

(21)   Kitova, E. N.; Bundle, D. R.; Klassen, J. S. *J. Am. Chem. Soc.* **2002**, *124*, 5902-5913.

(22)   Wang, W.; Kitova, E. N.; Klassen, J. S. *J. Am. Chem. Soc.* **2003**, *125*, 13630-13631.

(23)   Kitova, E. N.; Klassen, J. S. *Proceedings of the 53rd ASMS Conference on Mass Spectrometry and Allied Topics*; San Antonio, Texas, June, 2005.

(24)   Laskin, J.; Futrell, J. H. *J. Phys. Chem. A* **2003**, *107*, 5836-5839.

(25)   Dunitz, J. D. *Chem. Biol.* **1995**, *2*, 709-712.

(26)   Hoaglund, C. S.; Liu, Y.; Ellington, A. D.; Pagel, M.; Clemmer, D. E. *J. Am. Chem. Soc.* **1997**, *119*, 9051-9052.

(27) Lindahl, T.; Karlstrom, O. *Biochemistry* **1973**, *12*, 5151-5154.

(28) Lindahl, T.; Nyberg, B. *Biochemistry* **1972**, *11*, 3610-3618.

(29) Shapiro, R.; Danzig M. *Biochemistry* **1972**, *11*, 23-29.

(30) Winger, B. E.; Light-Wahl, K. J.; Rockwood, A. L.; Smith, R. D. *J. Am. Chem. Soc.* **1992**, *114*, 5897-5898.

(31) Suckau, D.; Shi, Y.; Beu, S. C.; Senko, M. W.; Quinn, J. P.; Wampler, F. M.; McLafferty, F. W. *J. Proc. Natl. Acad. Sci. USA* **1993**, *90*, 790-793.

(32) Campbell, S.; Rodgers, M. T.; Marzulff, E. M.; Beauchamp, J. L. *J. Am. Chem. Soc.* **1995**, *117*, 12840-12854.

(33) Griffey, R. H.; Greig, M. J.; Robinson, J. M.; Laude D. A. *Rapid Commun. Mass Spectrom.* **1999**, *13*, 113-117.

(34) Hofstadler, S. A.; Sannes-Lowery, K. A.; Griffey R. H. *J. Mass Spectrom.* **2000**, *35*, 62-70.

(35) Robinson, J. M.; Greig, M. J.; Griffey, R. H.; Mohan, V.; Laude D. A. *Anal Chem.* **1998**, *70*, 3566-3571.

(36) Habibi-Goudarzi, S.; McLuckey, S. A. *J. Am. Soc. Mass Spectrom.* **1995**, *6*, 102-113.

(37) Lias, S. G.; Bartmess, J. E.; Liebman, J. F.; Holmes, J. L.; Levin, R. D.; Mallard, W. G. *J. Phys. Chem. Ref. Data* **1988**, *17* (Suppl. 1).

(38) Strittmatter, E. F.; Schnier, P. D.; Klassen, J. S.; Williams, E. R. *J. Am. Soc. Mass Spectrom.* **1999**, *10*, 1095-1104.

(39) Monajjemi, M.; Chahkandi, B. *THEOCHEM J. Mol. Struct.* **2005**, *714*, 43-60.

(40) Wang, K.; Schall, O. F.; Gokel, G. W. *Supramol. Chem.* **1996**, *9*, 85-90.

Chapter 4

Determination of Protein-Ligand Association Thermochemistry Using

Variable-Temperature Nanoelectrospray Mass Spectrometry*

4.1 Introduction

The association of molecules to form specific noncovalent complexes is central to

many normal and pathological biological processes, such as cellular growth,

inflammation, adhesion, and bacterial and viral infections [1-4]. The physical basis of

molecular recognition is the formation of selective interactions between the binding

partners and by the concomitant displacement of solvent from the binding surfaces [5-

11]. Detailed information regarding the strength and specificity of interactions between

biological molecules is of great importance to achieve a more complete understanding of

biological processes. There are a number of analytical techniques available to quantify

the thermodynamic parameters for the association of biological molecules. These include

surface plasmon resonance (SPR) [12, 13], atomic force microscopy (AFM) [14], frontal

affinity chromatography-mass spectrometry (FAC/MS) [15-17], isothermal titration

microcalorimetry (ITC) [18-20], fluorescence spectroscopy [21-25] and circular

dichroism (CD) [26]. Each of these methods has its own strengths and weaknesses. ITC is

arguably the most reliable method for the determination of thermodynamic parameters

for association reactions. ITC is the only method to provide a direct measure of the

association enthalpy (ΔH_{assoc}); ITC also permits the determination of the association free

94

energy (ΔG_{assoc}) and, indirectly, the association entropy (ΔS_{assoc}). However, ITC requires fairly large quantities (~mg) of material (e.g. protein, ligand) for each analysis and is unable to provide direct information on binding stoichiometry. SPR offers good sensitivity and has the ability to determine on and off rate constants for biological complexes. In addition, van't Hoff analysis of the temperature dependence of the K_{assoc} can provide an estimate of the ΔH_{assoc} and ΔS_{assoc} values [27]. FAC/MS also affords high sensitivity and can be used to rapidly estimate binding constants for libraries of ligands, present as a mixture, for a given protein target. A common disadvantage of both SPR and FAC/MS techniques is that either the protein or the ligand must be immobilized on a solid phase which may alter the nature of protein-ligand interactions, leading to incorrect binding affinities. Spectroscopic methods have been extensively used in characterizing macromolecular interactions. For example, changes in intrinsic fluorescence followed by kinetic measurements, has been used to evaluate the affinity of human placental ribonuclease for placental ribonuclease inhibitor [23]. Thermodynamic parameters of the self-association of human glucagon have been evaluated by studying the temperature and concentration dependence of CD spectra [26]. However, the disadvantage with fluorescence and CD spectroscopy is that spectral interference from other species present in the sample solution can influence the final spectral response. In fluorescence spectroscopy, the covalently attached chromophores should not change the wild-type macromolecular behaviour.

Electrospray ionization mass spectrometry (ES/MS) is a powerful tool for studying noncovalent biological complexes such as multiprotein assemblies and protein-ligand complexes. In addition to providing a rapid and sensitive method for detecting

biomolecular complexes and directly establishing their binding stoichiometry, ES/MS-based methods hold tremendous promise for quantifying noncovalent interactions. There are a number of reported examples where it has been shown that the relative abundance of unbound and bound species (*e.g.* protein/protein-ligand complex) measured by ES/MS reflects, quantitatively, their relative concentrations in solution at equilibrium [28-30]. From a "snapshot" of the solution composition and known initial concentrations, it is possible to evaluate the K_{assoc}, *vide infra*.

Although most ES/MS affinity measurements reported to date have been performed at ambient temperatures, several studies have shown ES/MS to be suitable for studying the influence of temperature on association processes [31-38]. In the first MS-based study of the thermal stability of protein complexes in solution, Smith and coworkers evaluated association enthalpy (ΔH_{assoc}) of the RNase-S complex by heating the continuous infusion capillary [32]. However, it was found that the MS-derived value differed significantly from the literature value. This difference was attributed to the different pH and ionic strength of the ES solution. Robinson and coworkers recently demonstrated the application of a temperature-controlled nanoES device for the determination of the thermal stabilities of protein assemblies [37, 38].

The present work describes the design of a novel temperature-controlled nanoES device and its application to determine thermodynamic parameters for protein-ligand association reactions, ΔH_{assoc} and ΔS_{assoc}, which can be evaluated from the MS-derived K_{assoc} values. The device was applied to two carbohydrate-binding proteins to determine binding affinities over a range of solution temperatures performed with Fourier transform ion cyclotron resonance mass spectrometry (FT-ICR/MS). Measurements were

96

performed on the complex of a genetically engineered single chain variable fragment (scFv) of the monoclonal antibody Se155-4 with its native trisaccharide receptor, α-D-Gal$(1 \rightarrow 2)$[α-D-Abe$(1 \rightarrow 3)\alpha$-D-Man$p \rightarrow$OMe $\equiv \alpha$Gal[αAbe]αMan [39]. The complexes of αGal[αAbe]αMan with the Se155-4 antibody (IgG), the antigen-binding fragment (Fab) and the scFv have been the focus of extensive investigation in solution as part of a comprehensive study of carbohydrate recognition by proteins. Due to molecular weight considerations, the scFv•carbohydrate complexes were chosen for this study instead of the corresponding complexes of IgG and Fab proteins. Subjecting the MS-derived K_{assoc} values obtained at variable solution temperatures to a nonlinear least-squares analysis using the integrated form of van't Hoff equation, the ΔH_{assoc} and ΔS_{assoc} at 298 K were determined and compared with the values obtained by ITC for the IgG•αGal[αAbe]αMan [40]. To demonstrate that experimental conditions were generally suitable for protein-carbohydrate ligands, K_{assoc} for the scFv and four other oligosaccharide ligands, structural analogues of the native ligand, have been measured and compared with values obtained by ITC. The second system investigated was the complex of the homopentameric binding subunit of Shiga-like toxin 1 (Stx1 $B_5 \equiv B_5$) with the P^k trisaccharide, the carbohydrate portion of the natural cell-surface receptor, the glycolipid Gb3 [41]. From the temperature dependence of K_{assoc}, values of ΔH_{assoc} and ΔS_{assoc} were determined and compared to values obtained by ITC. The application of temperature-controlled device in competitive binding experiments, wherein binding affinities of several carbohydrate ligands were determined simultaneously, is also described.

97

4.2 Experimental

4.2.1 Protein and Carbohydrate Ligands

The carbohydrate-binding antibody single chain fragment, scFv (MW 26539 Da), was produced using recombinant technology [39]. The scFv was concentrated and dialyzed against deionized water using MICROSEP microconcentrators, with a molecular weight cut-off of 10 kDa, and lyophilized prior to MS analysis. The scFv was weighed immediately after removing it from the lyophilizer, dissolved in a known volume of aqueous 50 mM ammonium acetate and stored at −20 °C if not used immediately. A stock solution (~100 μM) of the homopentamer of Shiga-like toxin 1 (Stx1 $B_5 \equiv B_5$; MW 38429 Da) was prepared by D. R. Bundle (Univ. of Alberta) and used without further purification. The synthetic oligosaccharide ligands used in this work, αGal[αAbe]αMan (1), αAbe(2-OCH$_3$-αMan) (2), αTal[αAbe]αMan (3), αAbe(2-OCH$_3$-αMan)αGlcβGlc (4), αGlcβGlcαGal[αAbe]αMan (5), and globotrioside p^k (6), were provided by D. R. Bundle (Univ. of Alberta). The structures of these carbohydrates are shown in Figure 4.1. Any adsorbed water was removed from the ligand prior to the preparation of stock solution by drying the ligand in a vacuum chamber maintained at ~5 torr and 56 °C. Each nanoES solution was prepared from stock solution of protein and ligand with known concentrations.

98

αGal[αAbe]αMan (1)   αAbe(2-OCH₃-αMan) (2)   αTal[αAbe]αMan (3)

αAbe(2-OCH₃-αMan)αGlcβGlc (4)   αGlcβGlcαGal[αAbe]αMan (5)

Pᵏ trisaccharide (6)
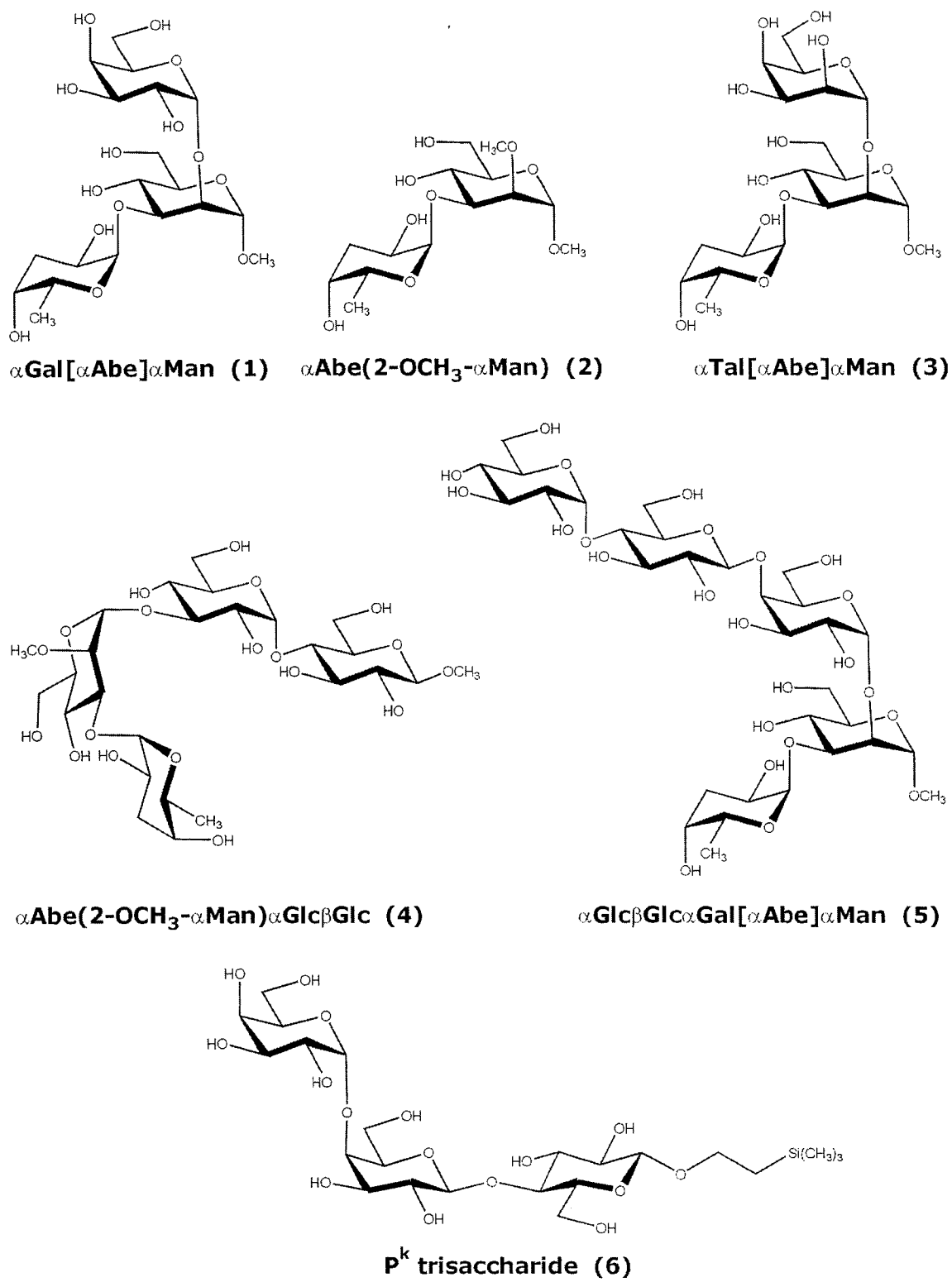
Figure 4.1 Structure of the oligosaccharide ligands.

99

4.2.2 Temperature-Controlled NanoES Device

The temperature of the nanoES solution was regulated using a specially constructed nanoES device, which was attached to the front of the mass spectrometer. The device consists of a Plexiglas chamber with one end attached to the front of the ion source of the mass spectrometer, surrounding the heated metal sampling capillary, a Plexiglas disc was also attached to the other end to seal the chamber. A schematic diagram of the chamber is shown in Figure 4.2. A Cu sleeve lined the inside of the Plexiglas chamber (45 mm in length, 38 mm i.d. and 41 mm o.d.). The total volume inside the chamber is approximately 60 mL. The nanoES tip was inserted into the chamber through a small aperture in the Plexiglas disc. The temperature of the air inside the chamber was regulated by passing heated or cooled air through wound Cu tubing which was in thermal contact with the Cu sleeve. A portion of the temperature regulated air (~700 mL/min) was introduced into the chamber through the Plexiglas disc to satisfy the gas intake requirement of the ion source, ~ 600 mL/min. The temperature of the nanoES solution was determined by attaching a thermocouple, TC_1, to the end of the nanoES tip positioned at 1-2 mm of the heated sampling inlet capillary. The temperature gradient inside the chamber were measured by two thermocouples, TC_2 positioned at 1 cm from the front of the mass spectrometer and TC_3 at 1 cm after the Plexiglas disc. Both of the thermocouples were also positioned at 1 cm above the Cu liner. Using this dual temperature control approach, the temperature inside the chamber can be controlled to within ±1.5 °C over the range of temperature used in this study, 5-40 °C (Figure 4.3).
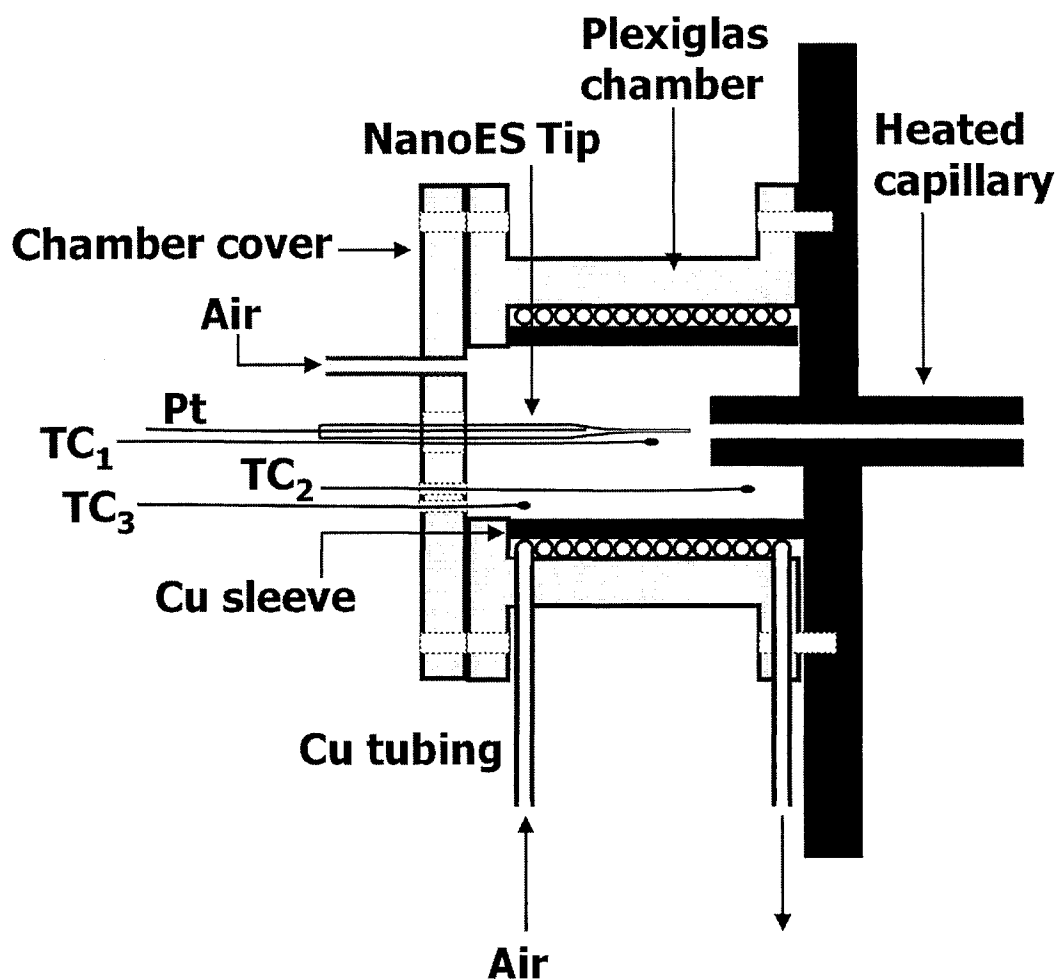
Figure 4.2 Schematic diagram of the temperature-controlled nanoES device. The sample droplets are sprayed using a nanoES tip inserted through a small aperture in the Plexiglas cover of the chamber, chamber cover. The temperature of the nanoES solution is controlled by regulating of the air passing through the wound Cu tubing which is in thermal contact with the Cu sleeve. The temperature of the nanoES solution is determined by thermocouple, TC_1, attached to the nanoES tip and positioned 1-2 mm from the heated sampling inlet capillary. Thermocouples TC_2 and TC_3 are used to measure the temperature gradient inside the chamber. These thermocouples are positioned approximately 1 cm from the front end of the mass spectrometer and Plexiglas chamber cover, respectively. The distance between these thermocouples and Cu liner is also 1 cm. To satisfy the gas intake requirement of the ion source, a portion of the regulated air (~700 mL/min) is introduced into the chamber through the Plexiglas disc. The total volume inside the chamber is approximately 60 mL.

101
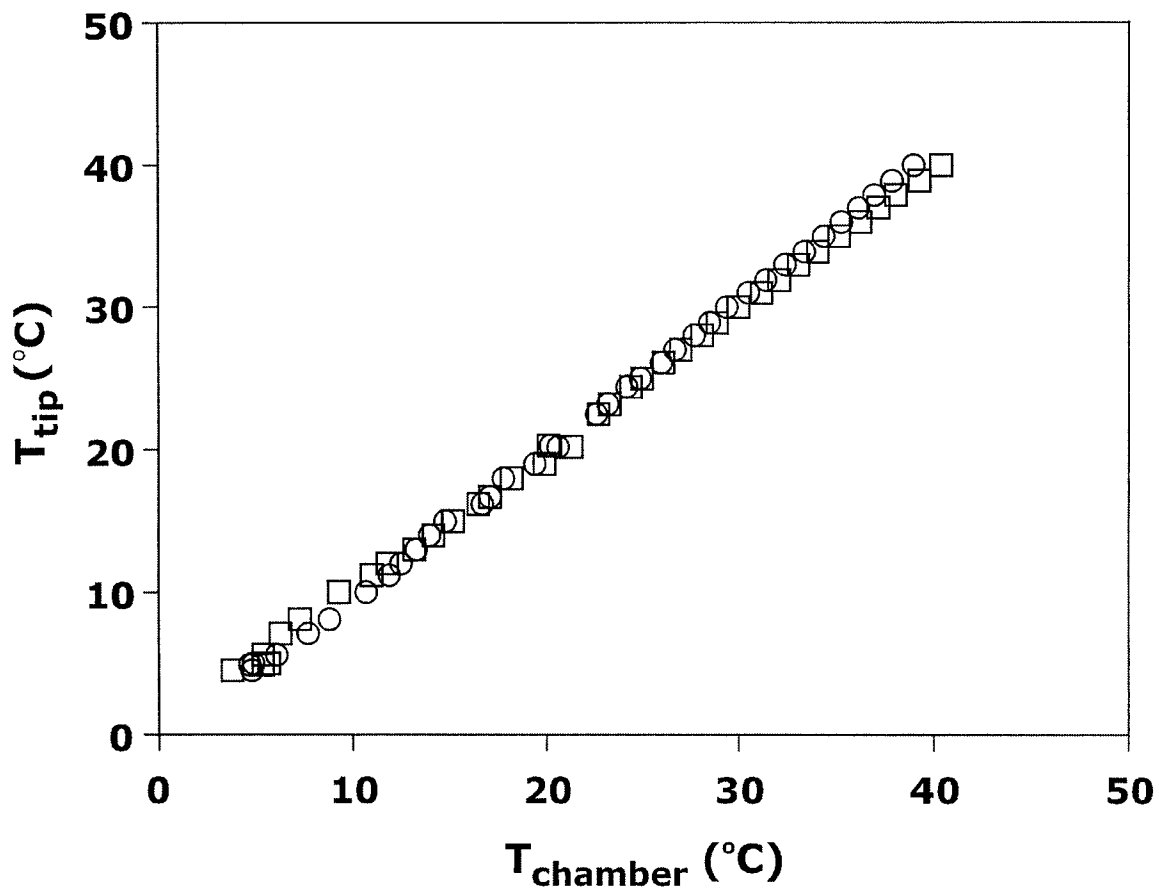
Figure 4.3 Temperature recorded at the nanoES tip, TC_1, versus the temperatures at the two ends of the chamber, TC_2 ($\square$) and TC_3 ($\bigcirc$), over the temperature range of this study 5-40 °C.

4.2.3 Mass Spectrometry

All experiments were performed using an Apex II 47e Fourier-transform ion cyclotron resonance (FT-ICR) mass spectrometer (Bruker, Billerica, MA) equipped with a modified external nanoelectrospray source. This instrument has been described previously [42] and only a brief description is given here. NanoES tips were pulled from aluminosilicate tubes (1 mm o.d., 0.68 mm i.d.) using a P-2000 puller (Sutter Instruments, Novato, CA). The shape of the tips was found to be quite reproducible, with an outer diameter of 4 to 7 µm. The wall thickness at the end of the tips was determined to be approximately 75 nm such that the i.d. and o.d. at the end of the nanoES tips are similar. A platinum (Pt) wire, inserted into the other end of the nanoES tip, was used to establish electrical contact with the nanoES solution. A potential of 800 to 1100 V was applied to the Pt wire in the nanoES tip in order to spray the solution. The tip was positioned inside the temperature-controlled chamber, 1-2 mm from a stainless steel sampling inlet capillary using a microelectrode holder. The solution flow rate ranged from 50 to 100 nL/min, depending on the outer diameter of the nanoES tip and the voltage. Typically, a stable nanoES ion current of ~0.1 µA was achieved.

The droplets and gaseous ions produced by nanoES were introduced into the vacuum chamber of the mass spectrometer through a heated stainless steel sampling capillary (0.43 mm i.d.) maintained at an external temperature of 34 °C. The gaseous ions sampled by the capillary (52 V) were transmitted through a skimmer (-2 V) and accumulated in a hexapole (600 V p-p). Unless otherwise noted, an accumulation time of 1 s was used. The ions were subsequently ejected from the hexapole and injected at approximately -2700 V into the bore of a 4.7 tesla superconducting magnet, decelerated

103

and introduced into the ion cell. The trapping plates of the cell were maintained at a constant potential of 1.5 V throughout the experiment. The typical base pressure for the instrument was ~5 x 10^{-10} mbar. Data acquisition was performed using the Bruker Daltonics XMASS software (version 5.0). The time-domain spectra, consisting of the sum of 20-50 transients containing 128 K data points per transient, were subjected to one zero-fill prior to Fourier-transformation.

4.3   Results and Discussion

4.3.1   Determining Thermodynamic Parameters (K_{assoc}, ΔH_{assoc}, ΔS_{assoc}) for Protein-Ligand Binding by ES/MS

The equilibrium constant, K_{assoc}, for an association reaction involving a protein (P) and a ligand (L) (eq 4.1), at given temperature, is given by eq 4.2:

$$P + L \leftrightarrow P\bullet L \tag{4.1}$$

$$K_{assoc} = \frac{[PL]_{equil}}{[P]_{equil}[L]_{equil}} \tag{4.2}$$

The equilibrium concentrations, $[PL]_{equil}$, $[P]_{equil}$, and $[L]_{equil}$, can be deduced from the initial concentration of protein and ligand in solution, $[P]_o$ and $[L]_o$, and the relative abundance of the protein ions, PL^{+n} and P^{+n}, from the ES mass spectrum. To determine K_{assoc}, the ratio (R) of the ion intensities (I) of the bound to unbound protein ions from the mass spectrum should be equivalent to concentrations in solution at equilibrium (eq 4.3).

$$R = \frac{I(PL^{+n})}{I(P^{+n})} = \frac{[PL]_{equil}}{[P]_{equil}} \tag{4.3}$$

104

The spray and detection efficiencies are expected to be similar when the solvent exposed

surface and the molecular weight of the protein and complex are comparable.

The equilibrium concentration, $[PL]_{equil}$, can be expressed based upon R and $[P]_o$

as shown in eq 4.4.

$$[PL]_{equil} = \frac{R[P]_o}{1+R} \tag{4.4}$$

The equilibrium concentration, $[L]_{equil}$, can be found from eq 4.5 and accordingly K_{assoc}

can be expressed as eq 4.6.

$$[L]_{equil} = [L]_o - [PL]_{equil} \tag{4.5}$$

$$K_{assoc} = \frac{[PL]_{equil}}{[P]_{equil}([L]_o - [PL]_{equil})} \tag{4.6a}$$

$$K_{assoc} = \frac{R}{[L]_o - \dfrac{R[P]_o}{1+R}} \tag{4.6b}$$

Using initial concentration of protein and ligand, with R value obtained from ES-mass

spectrum, K_{assoc} can be determined at a given temperature.

The magnitude of ΔH_{assoc} and ΔS_{assoc} for protein-ligand binding can be assessed

from a van't Hoff analysis of the temperature dependent binding affinity data. Typically,

this is done by subjecting the K_{assoc} data are to a non-linear least squares analysis using

the integrated form of the van't Hoff equation, which includes a temperature independent

heat capacity change (ΔC_p) (eq 4.7). T_o in eq 4.7 is an arbitrarily chosen reference

temperature (taken to be 298 K in the present work) and K_o and ΔH_o are the association

constant and enthalpy change, respectively, at that temperature. The magnitude of ΔS_{assoc}

at T_o can then be calculated from the ΔH_o and ΔG_o (determined from K_o) values.

105

$$\ln \frac{K}{K_o} = \frac{\Delta H_o - T_o \Delta C_p}{R} \left(\frac{1}{T_o} - \frac{1}{T} \right) + \frac{\Delta C_p}{R} \ln \frac{T}{T_o} \qquad (4.7)$$

4.3.2 Determining K_{assoc} for Protein-Ligand Binding by NanoES/MS. Some Experimental Considerations

To establish an accurate measurement of binding affinities, the relative abundance of unbound to bound species (*e.g.* the ratio of free protein/protein-ligand) determined by ES/MS should reflect, quantitatively, the relative ratio of ion concentrations in solution at equilibrium. Our laboratory has recently investigated the influence of solution and gas phase processes on protein-carbohydrate binding affinity measurements performed using the direct ES/MS approach in an attempt to identify the optimal experimental conditions for such measurements at ambient temperatures [30]. The scFv•1 complex served as a model system for this study. It was found that the use of short spray durations (< 10 min) was necessary to minimize the changes in solution pH due to the oxidation of solvent (eq 4.8). The use of near-equimolar concentrations of protein and ligand minimized the formation of nonspecific protein-ligand complexes; the formation of nonspecific complexes leads to artificially large K_{assoc} values. It was also found that short accumulation times (< 2 s) in the rf hexapole of the ion source was necessary to avoid collision-induced dissociation of the gaseous complex. In addition, due to differences in the charge state distribution of the gaseous, bound and unbound protein ions produced by nanoES, R should be calculated as from the ratio of the sum of complex to protein, taken over all charge states. (eq 4.9). Since the ion signal in FT-ICR/MS is proportional to the

106

abundance and the charge-state of the ion, chare normalized ion intensities were used to calculate R.

$$2H_2O \leftrightarrow O_2 + 4H^+ + 4e^- \tag{4.8}$$

$$R = \frac{[PL]_{equil}}{[P]_{equil}} = \frac{\sum_n [I(PL^{+n})/n]}{\sum_n [I(P^{+n})/n]} \tag{4.9}$$

In the present work, to minimize the error introduced by pH changes each nanotip was used once and for a short spray duration (< 5 min). In addition, the accumulation time of the ions in the hexapole was set to 1 s to minimize dissociation of protein-ligand complexes. Each MS-derived K_{assoc} value is, as well, an average of four replicate measurements. Also, R, which is determined from the mass spectrum, is an average of charge distributions observed for gaseous ions generated by nanoES.

4.3.3 Variable-Temperature Binding Study of Protein-Carbohydrate Complexes

Shown in Figure 4.4 are nanoES mass spectra acquired for a solution of scFv and 1 at 15, 25 and 35 °C. The ion abundance ratio of complex (scFv•1) to protein (scFv) is clearly seen to decrease with increasing solution temperature, which is the expected behaviour because the association reaction is exothermic [40]. At a given solution temperature, K_{assoc} was calculated from the ion abundance ratio measured by nanoES-MS using a procedure described previously [30].

The MS-derived values of K_{assoc} obtained for the scFv•1 complex at temperatures ranging from 10 to 35 °C are shown in Figure 4.5 in the form of a van't Hoff plot. Each value of K_{assoc} represents the average of four measurements. Also shown in Figure 4.5 are the values of K_{assoc} determined by ITC for the Se155-4 IgG•1 complex [40]. Because the

107

mass of the IgG•1 complex exceeds the capabilities of the mass spectrometer used in this work, MS-derived values of K_{assoc} could not be determined. However, given the uniform mode of binding for the IgG and scFv proteins, values of K_{assoc} for the IgG complex should closely resemble those of the corresponding scFv complex. The MS-derived K_{assoc} values are found to be in reasonable agreement with the ITC values over the temperature range investigated. This result indicates that any change in the temperature of the nanoES droplets, compared to that of the bulk solution, resulting from the evaporation process or sampling into the MS does not influence the original equilibrium distribution of scFv and scFv•1. This observation is consistent with Klassen's and coworkers' analysis of the kinetics of gas phase ion formation, compared with the association/dissociation kinetics of the scFv•1 complex, which suggested that the lifetime of the droplet is sufficiently short (< 40 µs) that the original distribution of protein and complex is not altered by the nanoES process [30].

The magnitude of ΔH_{assoc} and ΔS_{assoc} for the association of scFv and 1 was evaluated by subjecting the binding affinity data to a non-linear least squares analysis using the integrated form of the van't Hoff equation, which includes a temperature independent heat capacity change (ΔC_p) (eq 4.7). Fitting eq 4.7 to the MS data yielded a ΔH_{assoc} of 7.0 ± 0.3 kcal/mol at 25 °C. This agrees well with the value of 6.8 ± 0.4 kcal mol^{-1} established by ITC for the IgG•1 complex [40]. It is worth noting that, despite a non-negligible ΔC_p for this reaction, determined to be -114 cal mol^{-1} K^{-1} by ITC [40], neglect of ΔC_p in the fitting procedure results in a ΔH_{assoc} of 7.4 ± 0.3 kcal mol^{-1}, which is indistinguishable from the value determined from the non-linear fitting, within the experimental error.

108

To demonstrate that the nanoES/MS-based method is generally suitable for the determination of thermochemical parameters for protein-carbohydrate binding, values of K_{assoc} for five additional complexes were measured at temperatures of 5 to 40 °C. Van't Hoff plots obtained by MS for the association of the scFv and the ligands **2** - **5**, which are structural analogs of **1**, are shown in Figure 4.6. Also shown is the van't Hoff plot for the formation of the $B_5 \bullet 6$ complex. The thermochemical data obtained by nanoES-MS and ITC at 25 °C are listed in Table 4.1. Shown in Figure 4.7 are nanoES mass spectra acquired for a solution of B_5 and P^k at 10, 25, and 40 °C. The B_5 protein complex possesses five equivalent P^k binding sites, one per subunit. As a result, the *apparent* K_{assoc} includes a statistical factor, which reflects the number of binding sites of the receptor [43]. The values of K_{assoc} (Figure 4.6) were adjusted to represent the P^k interaction at a single binding site. For all of the complexes investigated, the MS-derived ΔH_{assoc} values agree with the ITC results within 1 kcal mol^{-1}. Similarly, the MS-derived ΔS_{assoc} values are in reasonable agreement with the ITC results, within 4 cal mol^{-1} K^{-1}.

109

Figure 4.4 NanoES mass spectra obtained in positive mode for an aqueous solution of scFv (4 µM) and **1** (7 µM) with 6 mM CH_3COONH_4 at (a) 15 °C, (b) 25 °C, (c) 35 °C.

110

Figure 4.5 Temperature dependence of K_{assoc} for the reaction, scFv + 1 ↔ scFv•1, determined by nanoES/MS (●), and the reaction IgG + 1 ↔ IgG•1, determined by ITC (○), ref 40. The dashed line corresponds to the nonlinear fit of the vant't Hoff equation (eq 4.7) to the MS-derived values of K_{assoc}. The error bars correspond to one standard deviation.

111

Figure 4.6 Van't Hoff plots, constructed from K_{assoc} values measured by nanoES-MS, for the formation of the complexes: scFv•L, where L = **2** (▲), **3** (○), **4** (□), **5** (◆) and B$_5$•6 (●). Each value of K_{assoc} corresponds to the average of four measurements. The solid lines correspond to the non-linear fit (eq 4.7) of the experimental K_{assoc} values for each complex.

112

Table 4.1 Thermochemical parameters for the association reaction: P + L ↔ (P•L), where P = protein (scFv, B_5) and L = oligosaccharide ligand (**1** - **6**), determined at 25 °C by nanoES-FT-ICR/MS and ITC.[a]

P	L	$-\Delta H_{assoc}$ (kcal mol^{-1}) MS	$-\Delta H_{assoc}$ (kcal mol^{-1}) ITC	$-\Delta S_{assoc}$ (cal mol^{-1} K^{-1}) MS	$-\Delta S_{assoc}$ (cal mol^{-1} K^{-1}) ITC
scFv	**1**	7.0 ± 0.3	6.8 ± 0.4 [b]	-0.2 ± 0.2	-1.2 ± 1.6 [b]
scFv	**2**	9.7 ± 0.4	9.3 ± 0.2 [b]	8.7 ± 0.4	7.6 ± 0.6 [b]
scFv	**3**	9.9 ± 0.8	9.1 ± 0.1 [b]	10.0 ± 1.0	7.5 ± 0.2 [b]
scFv	**4**	11.5 ± 0.5	11.2 ± 0.1 [b]	12.3 ± 0.6	11.2 ± 0.3 [b]
scFv	**5**	8.7 ± 0.8	8.0 ± 0.1 [b]	3.7 ± 0.4	1.2 ± 0.1 [b]
B_5	**6**	10.9 ± 1.1	12 ± 1 [c]	23.0 ± 2.2	27 ± 1 [c]

a. The reported errors are one standard deviation.

b. Values taken from ref 40 and correspond to ligand binding to Se155-4 IgG.

c. Values taken from ref 41.
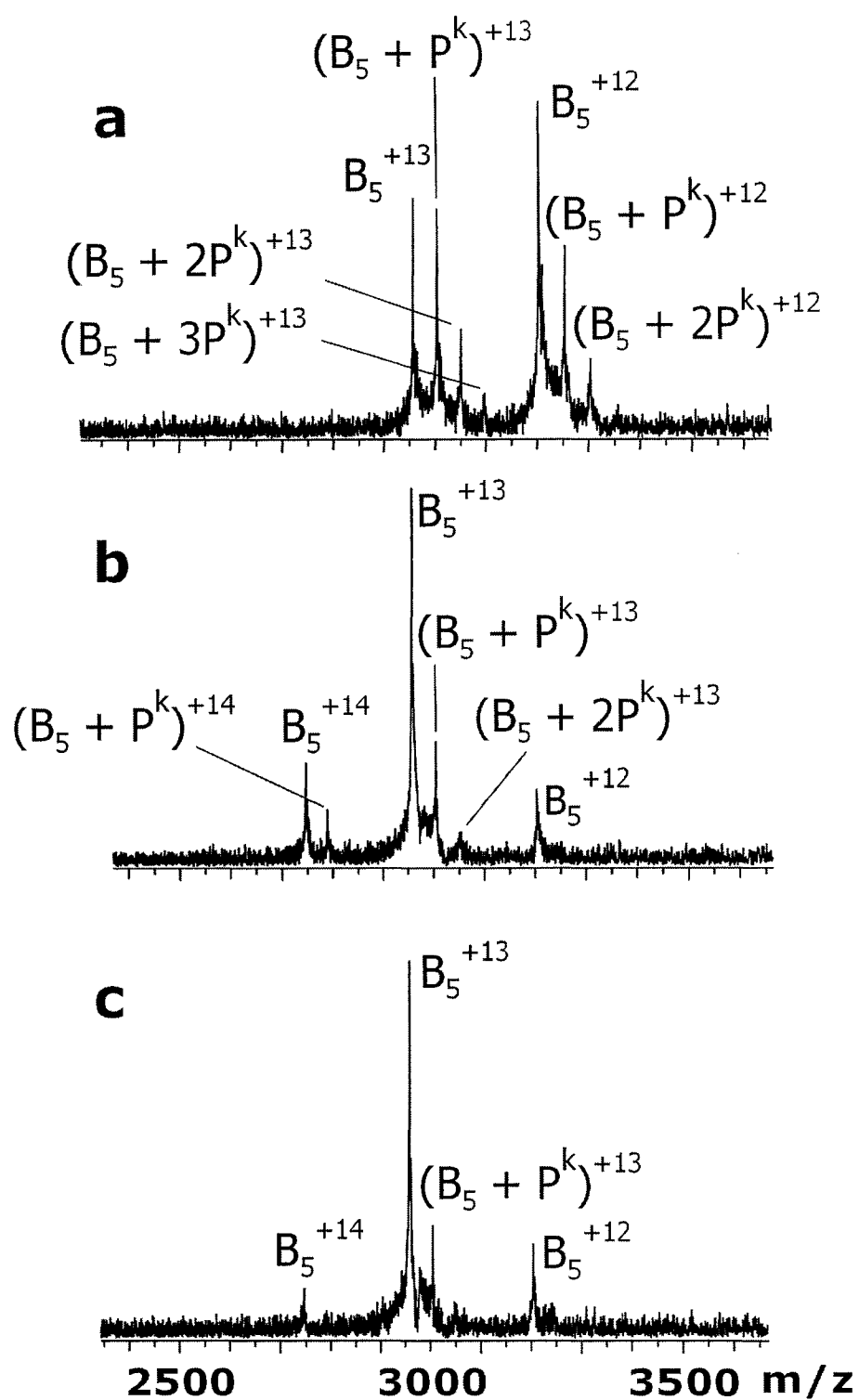
113

Figure 4.7 NanoES mass spectra obtained for an aqueous solution of Stx1 B_5 (22 µM), P^k (46 µM) and CH_3COONH_4 (9 mM) at (a) 10 °C, (b) 25 °C and (c) 40 °C.

114

4.3.4 Variable-Temperature Competitive Binding Experiments

It is well known that mass spectrometry can be used for simultaneous measurements of protein-ligand binding affinities. This can be accomplished with a competition type experiment, performed with solutions containing a single protein and a mixture of ligands with different molecular weights [44, 45]. A protein-ligand complex with known K_{assoc} is used as an internal reference and the binding affinities of the other complexes evaluated relative to it. The competition experiment can be performed with solutions contain a single protein and a mixture of ligands, where the total concentration of protein is equal to or less than the total concentration of ligand [46, 47]. Alternatively, to simplify the calculation, the experiment can be performed using an equimolar solution of protein and ligands [48]. The unknown association constant is determined from the following expression:

$$K_x = K_r \, \frac{I_{(PL_x)}}{I_{(PL_r)}} \left(\frac{I_p + \sum\limits_{i \neq r}^{j} I_{(PL_i)}}{I_p + \sum\limits_{i \neq x}^{j} I_{(PL_i)}} \right) \tag{4.10}$$

where K_x and K_r are the unknown and known (reference) binding affinities, respectively. Likewise, $I_{(PLx)}$, $I_{(PLr)}$, and I_P are the intensities of the complexes of interest (unkown), reference and unbound protein measured by MS, respectively. Shown in Figure 4.8 are nanoES mass spectra obtained for an aqueous equimolar solution containing scFv, **1**, **2**, and **4** over the temperature range 10 - 35 °C. To evaluate ΔH_{assoc} values, van't Hoff plots were constructed from temperature dependence of K_{assoc}, obtained for complexes between scFv and carbohydrate ligands, determined by nanoES-MS and competition experiments using equations 4.7 and 4.10. The (scFv + **1**) complex was chosen as reference complex,

115

with a MS-derived K_{assoc} of 1.5×10^5 M^{-1} at 25 °C, where n = 9 - 12 (Figure 4.9). We, also, performed a second temperature-dependent solution binding experiment on solutions containing scFv and **1** with **4**, the ligand with 5 times bigger K_{assoc} value in compare with **2** at 25 °C. Figure 4.10 shows related van't Hoff plots where corresponding ΔH_{assoc} value for (scFv•**4**) complex is listed in Table 4.2. Table 4.2 summarizes ΔH_{assoc} values determined at 25 °C by nanoES-MS and ITC techniques. Interestingly, ΔH_{assoc} values determined by the competition experiments agree less well with ITC values than those from single binding experiments. However, the order of enthalpies is in agreement with the order determined by ITC. As of Table 4.2, MS-derived ΔH_{assoc} value and its associated error for (scFv + **4**)$^{+n}$ complex have not changed. Since aforementioned results obtained from experiments which were performed based on equimolarity assumption, any error in solution preparation, like analyte concentration, will serve as a source for error. Also, the difference between recorded sample spray temperature, measured by a thermocouple next to nanoES tip and real temperature of the solution in the glass capillary inside the temperature-controlled device, or the precision level of regulating temperature especially at lower temperatures can be considered as other sources of error. Currently our group is working on improving the temperature-controlled device and elevating the precision associated with temperature reading by making changes in the regulating temperature method.

Figure 4.8 NanoES mass spectra obtained in positive ion mode for equimolar aqueous solutions (6 μM) containing scFv, **1**, **2**, and **4**, and CH_3COOH (6 mM) at (a) 15 °C, (b) 25 °C, and (c) 35 °C.

117
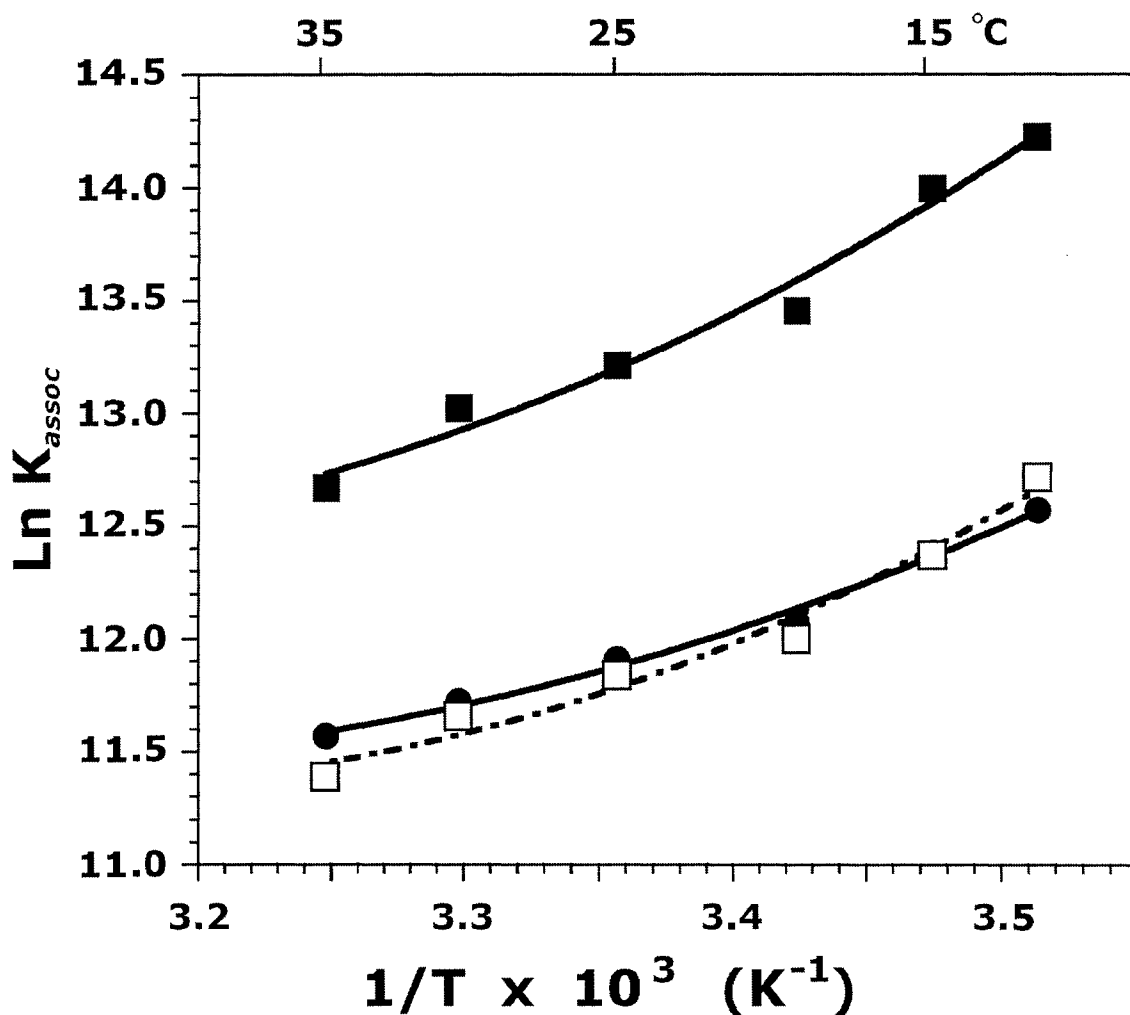
Figure 4.9 Van't Hoff plots, constructed from K_{assoc} values measured by nanoES-MS and competition experiment, for the formation of the complexes: scFv•L, where L = 1 (●), 2 (□), and 4 (■). NanoES mass spectra obtained in positive ion mode for equimolar aqueous solutions (6.0 μM) containing scFv, 1, 2, and 4. (scFv•1)$^{+n}$ complex served as internal reference. The dashed and solid lines correspond to the non-linear fit (eq 4.7) of the experimental K_{assoc} values for each complex.

118

Table 4.2 Enthalpies of association for the reaction: scFv + L ↔ (scFv•L), where L = oligosaccharide ligand (**2**, **4**), determined at 25 °C by nanoES-FT-ICR/MS using competition experiment and ITC.[a]

P	L	$-\Delta H_{assoc}$ (kcal mol^{-1})	
		MS[b]	ITC
scFv	**2**	8.1 ± 1.0	9.3 ± 0.2 [c]
scFv	**4**	10.4 ± 1.1	11.2 ± 0.1 [c]
scFv	**4**	10.5 ± 0.6^d	11.2 ± 0.1 [c]

a. The reported errors are one standard deviation.

b. (scFv•**1**) complex with a MS-derived K_{assoc} of 1.5 x 10^{-5} M^{-1} at 25 °C was used as the internal reference for the competition experiment.

c. Values taken from ref 40 and correspond to ligand binding to Se155-4 IgG.

d. Data obtained from solutions containing ligands **1** and **4**.

119
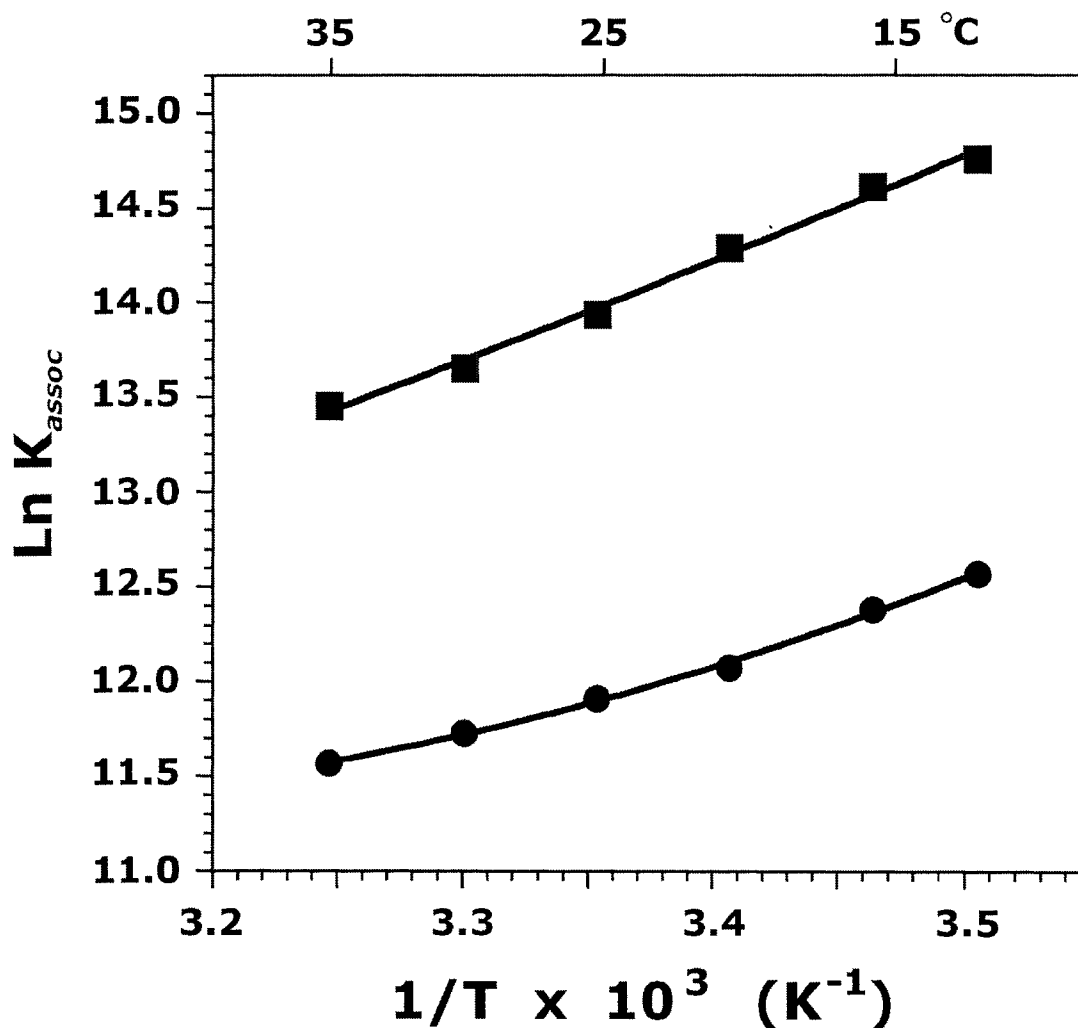
Figure 4.10 Van't Hoff plots, constructed from K_{assoc} values measured by nanoES-MS and competition experiment, for the formation of the complexes: scFv•L, where L = 1 (●), and 4 (■)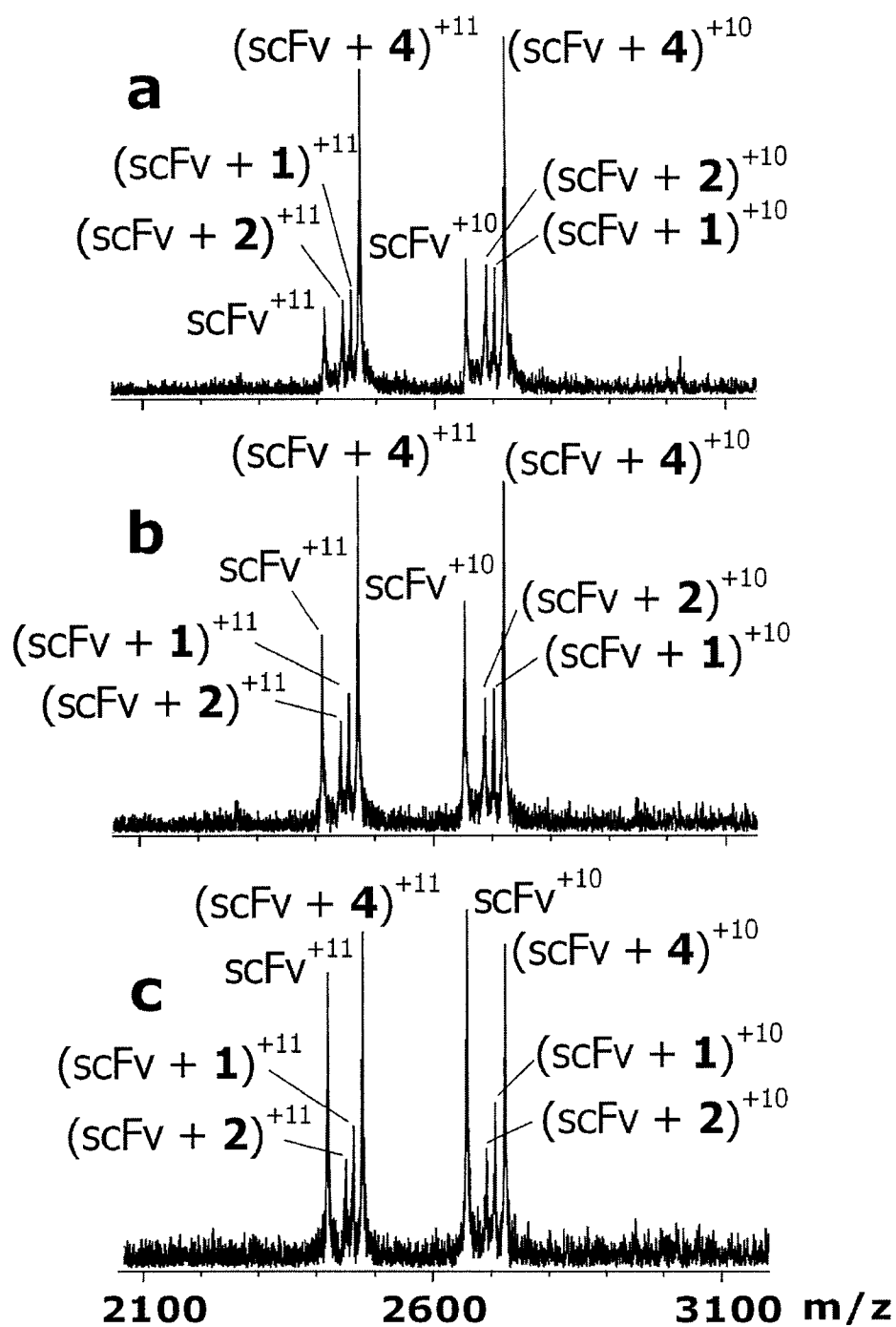. NanoES mass spectra obtained in positive ion mode for equimolar aqueous solutions (6 μM) containing scFv, 1, and 4. (scFv•1)$^{+n}$ complex served as internal reference. The solid lines correspond to the non-linear fit (eq 4.7) of the experimental K_{assoc} values for each complex.

120

4.4   Conclusions

In summary, we have developed a novel temperature-controlled nanoES device and applied it in a variable temperature nanoES/MS study of protein-carbohydrate binding. Values of K_{assoc} were measured for the binding of scFv with its native trisaccharide ligand and structural analogues, and Stx1 B_5 with P^k trisaccharide solutions in the temperature range 5 to 40 °C. From the temperature dependence of K_{assoc}, values of ΔH_{assoc} and ΔS_{assoc} (at 25 °C) were determined. The thermochemical data are found to be in good agreement with values determined previously by ITC. Competitive binding experiments were also performed on protein-carbohydrate complexes over temperature range 10 - 35 °C. The evaluated ΔH_{assoc} values trend was in consistent with the trend obtained by ITC. The results of this study demonstrate that variable temperature nanoES-MS can be used to quantify the thermochemistry for protein-ligand binding. This technique is expected to find wide application in the areas of drug design and high throughput target screening.

As described in Chapter 5, this device can also be used to study the influence of temperature on the structure and stability of multiprotein complexes in solution.

121

4.5 Literature Cited

(1) Varki, A. *Glycobiology* **1993**, *3*, 97-130.

(2) Lis, H.; Sharon, N. *Chem. Rev.* **1998**, *98*, 637-674.

(3) Rudd, P. M.; Elliott, T.; Cresswell, P.; Wilson, I. A.; Dwek, R. A. *Science* **2001**, *291*, 2370-2376.

(4) Di Tullio, A.; Reale, S.; De Angelis, F. *J. Mass Spectrom.* **2005**, *40*, 845-865.

(5) Rand, R. P. *Science* **1992**, *256*, 618.

(6) Colombo, M. F.; Rau, D. C.; Parsegian, V. A. *Science* **1992**, *256*, 655-659.

(7) Israelachvili, J.; wennerström, H. *Nature* **1996**, *379*, 219-225.

(8) Gohlke, H.; Klebe, G. *Angew. Chem. Int. Ed.* **2002**, *41*, 2645-2676.

(9) Lemieux, R. U. *Acc. Chem. Res.* **1996**, *29*, 373-380.

(10) Chervenac, M. C.; Toone, E. J. *J. Am. Chem. Soc.* **1994**, *116*, 10533-10539.

(11) Kitova, E. N.; Bundle, D. R.; Klassen, J. S. *Angew. Chem. Int. Ed.* **2004**, *43*, 4183-4186.

(12) MacKenzie, C. R.; Hirama, T.; Deng, S.-J.; Bundle D. R.; Narang, S. A.; Young, N. M. *J. Biol. Chem.* **1996**, *271*, 1527-1533.

(13) Lundquist, J. J.; Toone, E. J. *Chem. Rev.* **2002**, *102*, 555-578.

(14) Ratcliff, G. C.; Erie, D. A. *J. Am. Chem. Soc.* **2001**, *123*, 5632-5635.

(15) Schriemer, D. C.; Bundle, D. R.; Li, L.; Hindsgaul, O. *Angew. Chem. Int. Ed. Engl.* **1998**, *37*, 3383-3387.

(16) Schriemer, D. C.; Hindsgaul, O. *Comb. Chem. High Throughput Screening* **1998**, *1*, 155-170.

(17) Zhang, B. Y.; Chan, N.; Schriemer, D. C.; Palcic, M. M.; Hindsgaul, O. *Glycobiology* **1999**, *9*, 1103.

(18) Wiseman, T.; Williston, S.; Brandts, J. F. Lin, L.-N. *Anal. Biochem.* **1998**, *179*, 131-137.

(19) Freire, E.; Mayorga, O. L.; Straume, M. *Anal. Chem.* **1990**, *62*, 950A-959A.

(20) Bundle, D. R.; Sigurskjold, B. W. *Methods Enzymol.* **1994**, *247*, 288-305.

(21) Otto-Bruc, A.; Antonny, B.; Vuong, T. M.; Chardin, P.; Chamber, M. *Biochemistry* **1993**, *32*, 8636-8645.

(22) Wensel, T. G.; Stryer, L. *Biochemistry* **1990**, *29*, 2155-2161.

(23) Shapiro, R.; Vallee, B. L. *Biochemistry* **1991**, *30*, 2246-2255.

(24) Auer, M.; Moore, K. J.; Meyer-Almes, F. J.; Guenther, R.; Pope, A. J.; Stoeckli, K. A. *Drug Discov. Today* **1998**, *3*, 457-465.

(25) Zemanova, L.; Schenk, A.; Hunt, N.; Nienhaus, G. U.; Heilker, R. *Biochemistry* **2004**, *43*, 9021-9028.

(26) Formisano, S.; Johnson, M. L.; Edelhoch, H. *Proc. Natl. Acad. Sci. U.S.A.* **1977**, *74*, 3340-3344.

(27) Day, Y. S. N.; Baird, C. L.; Rich, R. L.; Myszka, D. G. *Protein Science* **2002**, *11*, 1017-1025.

(28) Daniel, J. M.; Friess, S. D.; Rajagopalan, S.; Wendt, S.; Zenobi, R. *Int. J. Mass Spectrom.* **2002**, *216*, 1-27.

(29) Zhang, S.; Van Pelt, C. K.; Wilson, D. B. *Anal. Chem.* **2003**, *75*, 3010-3018.

(30) Wang, W.; Kitova, E. N.; Klassen, J. S. *Anal. Chem.* **2003**, *75*, 4945-4955.

(31) Goodlett, D. R.; Ogorzalek Loo, R. R.; Loo, J. A.; Wahl, J. H.; Udseth, H. R.; Smith, R. D. *J. Am. Soc. Mass Spectrom.* **1994**, *5*, 614-622.

(32) Ogorzalek Loo, R. R.; Goodlet, D. R.; Smith, R. D.; Loo, J. A. *J. Am. Chem. Soc.* **1993**, *115*, 4391-4392.

(33) Robinson, C. V.; Chung, E. W.; Kragelund, B. B.; Knudsen, J.; Aplin, R. T.; Poulsen, F. M.; Dobson, C. M. *J. Am. Chem. Soc.* **1996**, *118*, 8646-8653.

(34) Veenstra, T. D.; Tomlinson, A. J.; Benson, L.; Kumar, R.; Naylor, S. *J. Am. Soc. Mass Spectrom.* **1998**, *9*, 580-584.

(35) Fändrich, M.; Tito, M. A.; Leroux, M. R.; Rostom, A. A.; Hartl, F. U.; Dobson, C. M.; Robinson, C. V. *Proc. Natl. Acad. Sci. U.S.A.* **2000**, *97*, 14151-14155.

(36) Mangrum, J. B.; Flora, J. W.; Muddiman, D. C. *J. Am. Soc. Mass Spectrom.* **2002**, *13*, 232-240.

(37) Benesch, J. L. P.; Sobott, F.; Robinson, C. V. *Anal. Chem.* **2003**, *75*, 2208-2214.

(38) Lentze, N.; Aquilina, J. A.; Lindbauer, M.; Robinson, C. V.; Narberhaus, F. *Eur. J. Biochem.* **2004**, *271*, 2494-2503.

(39) Zdanov, A.; Li, Y.; Bundle, D. R.; Deng, S.-J.; MacKenzie, C. R.; Narang, S. A.; Young, N. M.; Cygler, M. *Proc. Natl. Acad. Sci. U.S.A.* **1994**, *91*, 6423-6427.

(40) Bundle D. R. Unpublished data.

(41) St. Hilaire, P. M.; Boyd, M. K.; Toone, E. J. *Biochemistry* **1994**, *33*, 14452-14463.

(42) Felitsyn, N.; Kitova, E. N.; Klassen, J. S. *Anal. Chem.* **2001**, *73*, 4647-4661.

(43) Wang, W.; Kitova, E. N.; Klassen, J. S. *Methods in Enzymology*; Lee, Y. C.; Lee. R. T. Eds.; Academic Press: San Diego, 2003, Vol. 362, 376-398.

(44)   Cheng, X.; Chen, R.; Bruce J. E.; Schwartz, B. L.; Anderson, G. A.; Hofstadler, S. A.; Gale, D. C.; Smith, R. D.; Gao, J.; Sigal, G. B.; Mammen, M.; Whitesides, G. M. *J. Am. Chem. Soc.* **1995**, *117*, 8859-8860.

(45)   Höfner, G.; Wanner, K. T. *Angew. Chem. Int. Ed. Engl.* **2003**, *42*, 5235-5237.

(46)   Li, Y.-T.; Hsieh, Y.-L.; Henion, J. D.; Ocain, T. D., Schiehser, G. A.; Ganem, B. *J. Am. Chem. Soc.* **1994**, *116*, 7487-7493.

(47)   Loo, J. A.; Hu, P.; McConnell, P.; Mueller, W. T.; Sawyer, T. K.; Thanabal, V. *J. Am. Soc. Mass Spectrom.* **1997**, *8*, 234-243.

(48)   Jørgensen, T. J. D.; Roepstorff, P.; Heck, A. J. R. *Anal. Chem.* **1998**, *70*, 4427-4432.

125

Chapter 5

Stability of the Homopentameric B Subunits of Shiga Toxins 1 and 2 in Solution as Revealed by NanoES-FT-ICR/MS*

5.1 Introduction

The Shiga toxins (Stx's) 1 and 2 are bacterial enterotoxins produced by the enterohemorrhagic group of enterovirulant *Escherichia coli* (EHEC) [1]. These organisms represent a sub-group of the Shigatoxigenic *E. coli* and are isolated from human subjects experiencing hemorrhagic colitis and, occasionally, the hemolytic-uremic syndrome (HUS). Although numerous EHEC serotypes have been isolated from subjects experiencing hemorrhagic colitis, *E. coli* O157:H7 represents the predominant serotype in North America, Japan and Europe. EHEC infection most commonly occurs from the consumption of contaminated undercooked ground beef, unprocessed contaminated drinking water or other products which have been exposed to a source of contaminated unprocessed water [1].

The clinical signs associated with hemorrhagic colitis are mainly due to the ability of EHEC to colonize human gastrointestinal epithelial cells by a characteristic attaching and effacing mechanism involving numerous virulence-associated factors [2]. Stx1 and Stx2 also contribute to the hemorrhagic colitis phase of the illness by exacerbating the host inflammatory response to the infection. In approximately 10 to 15 % of subjects,

---

mostly young children and the elderly, EHEC infections can progress to HUS, which may be life threatening. HUS occurs when the Shiga toxins spread systemically throughout the body and attack endothelial cells, predominantly those forming the glomerular capillaries in the kidney [1]. This precipitates a cascade of pathological events leading to a decline in circulating platelets (thrombocytopenia), hemolytic anemia and acute renal failure. In very severe cases, blood vessels nourishing the central nervous system can also be effected and this results in neurological complications as well as the renal involvement.

The Shiga toxins display classical AB_5 structures, in which a single A subunit (32 kDa) is associated with five identical B subunits (8 kDa) [3, 4]. The A subunit is responsible for toxicity and acts by shutting down protein biosynthesis in target cells. The five B subunits assemble into a doughnut-shaped structure in which the central pore created by the B subunits hosts the C terminus of the A subunit [3, 4]. The B_5 homopentamers contain multiple binding sites for a glycolipid ($Gal\alpha 1$-$4Gal\beta 1$-4glucosyl-ceramide, Gb3), the natural cell surface receptor that is located on the surface of target cells [5].

The amino acid sequences of the A and B subunits of Stx1 and Stx2 are 52% and 60% identical, respectively [6, 7]. The theoretical pI values of Stx1 and Stx2, calculated from their amino acid sequences, are 6.5 and 5.2, respectively. The pI values for the A subunits are 8.7 (Stx1) and 8.0 (Stx2) and for the B subunits the values are 5.6 (Stx1) and 4.7 (Stx2). Both toxins possess similar numbers of basic (Stx1 A subunit: 24 x Arg, 3 x Lys, 8 x His; Stx1 B subunit: 2 x Arg, 6 x Lys, 1 x His; Stx2 A subunit: 24 x Arg, 3 x Lys, 7 x His; Stx2 B subunit: 1 x Arg, 6 x Lys) and acidic residues (Stx1 A subunit: 18 x Asp, 7 x Glu; Stx1 B subunit: 5 x Asp, 3 x Glu; Stx2 A subunit: 11 x Asp, 15 x Glu; Stx2

127

B subunit: 5 x Asp, 5 x Glu). X-ray crystal structures of both the Stx1 and Stx2 holotoxins and the Stx1 B_5 homopentamer complexed with the P^k trisaccharide, a structural analog of the carbohydrate component of Gb3, have been solved [3-5, 8]. A comparative analysis of the two holotoxin structures reveals that the B subunits of both toxins exhibit similar secondary, tertiary and quaternary structure. Each subunit within the homopentamer forms two three-stranded antiparallel β sheets and an α helix. The second β-strand of each B subunit monomer interacts with the sixth β-strand of the neighboring monomer. Putative inter-subunit interactions were identified from the X-ray crystal structures for Stx1 and Stx2. In this analysis, each of the neighboring pairs of subunits can form two inter-subunit hydrogen bonds (Tyr14 - Asn35 and Phe68 - Thr12), while three salt-bridges were identified for the Stx1 B subunit (Glu10 - Arg69, Glu65 - Lys13 and Arg33 - Asp18) and two for the Stx2 B subunit (Glu64 - Lys12, Arg32 - Asp17). The tertiary structure of each subunit is also stabilized by a disulfide bond between two Cys amino acids located in the first and the fifth β-strands. As well, the quaternary structure of the pentamer is likely stabilized by hydrophobic interactions between the α helices that line the pore of the complex. A solution structure obtained by NMR has also been reported for the Stx1 B_5 homopentamer [9] and found to be in agreement with X-ray data. To our knowledge, the structure and stability of Stx2 or the Stx2 B_5 homopentamer in solution have not been previously investigated.

Despite their similar crystal structures [3, 4] and sequences [6, 7], the two Shiga toxins exhibit differences in biological activity, with Stx2 being more potent than Stx1 *in vitro* and *in vivo* and more closely associated with the most severe consequences of *E. coli* infections in humans [10-17]. The origin of the differential toxicities of Stx1 and

128

Stx2 is not fully known but may arise from differences in receptor recognition or differences in the structure and stability of the Stx B subunits [18] which are not apparent in the X-ray crystal structures.

The assembly of Stx1 and the Stx1 B pentamers in aqueous solution has been previously studied by nanoelectrospray (nanoES) mass spectrometry (MS) [19]. It was shown that the B_5 homopentamer of the Stx1 B subunit is readily observed in spectra produced from aqueous solutions with a pH of 3.5 to 7. The intact holotoxin was also observed, albeit from an acidified solution (pH 3.5). MS has not previously been used to investigate the assembly of Stx2 or the Stx2 B pentamer. In the present work we have applied temperature-controlled nanoES and Fourier-transform ion cyclotron resonance mass spectrometry (FT-ICR/MS) to compare the influence of solution conditions (concentration, temperature, pH and ionic strength) on the assembly of the B subunits of Stx1 and Stx2. The main objective was to assess the relative stabilities of the two homopentamers under the different solution conditions investigated.

5.2 Experimental

5.2.1 Proteins

Stx1 B and Stx2 B were expressed in *E. coli* using a procedure described previously [23]. Both proteins were purified to > 95% purity by affinity chromatography as described in article [24], dialyzed against 50 mM or 100 mM ammonium acetate (pH 7) and stored at -20°C. A stock solution of the Stx1 B subunit at a concentration 1.15 mg/ml (150 μM) in 50 mM ammonium acetate and three stock solutions of the Stx2 B subunit, at concentrations of 1 mg/ml (130 μM - Stock 1) in 50 mM ammonium acetate

129

(pH 7), and 4.3 mg/ml (550 μM - Stock 2) and 1.5 mg/ml (190 μM - Stock 3), in 100 mM ammonium acetate (pH 7), were prepared. The nanoES solutions were prepared by thawing the stock solutions at room temperature and diluting an aliquot to a concentration of between 5 and 85 μM with aqueous ammonium acetate. The stock solutions were subjected to several freeze-thaw cycles without any observable influence on binding in solution. Unless otherwise specified, all of the nanoES solutions were allowed to stand for at least 10 min prior to acquiring mass spectra in order to establish an equilibrium distribution of the different oligomeric states of the B subunits.

5.2.2 Mass Spectrometry

All experimental measurements were performed using a modified Apex II 4.7 tesla FT-ICR/MS (Bruker, Billerica, MA) equipped with a temperature-controlled nanoES device developed in our laboratory [25]. The nanoES device consists of a Plexiglass chamber that surrounds the sampling capillary of the ion source. The chamber is lined with a copper sleeve that is in thermal contact with copper tubing that can be regulated to temperatures ranging from 0 to 60 °C by circulating heated or cooled air. A portion of the circulating air is also introduced directly into the chamber to satisfy the air intake requirement of the ion source. Using this dual approach, the temperature inside the chamber can be regulated to within ±1.5 °C. NanoES tips, with an outer diameter of 4 to 7 μm, were pulled from aluminosilicate tubes (1 mm o.d., 0.68 mm i.d.) using a P-2000 micropipette puller (Sutter Instruments, Novato, CA). A platinum wire, inserted into the other end of the nanoES tip, was used to establish electrical contact with the nanoES solution. A potential of ±600 to 800 V was applied to the platinum wire in the nanoES tip

in order to spray the solution. The tip was positioned 1 - 2 mm from a stainless steel sampling capillary using a microelectrode holder. Typical solution flow rates were 20 to 50 nL/min, depending on the outer diameter of the nanoES tip and the voltage used. Charged droplets and solvated ions emitted by the nanoES tip were introduced into the vacuum chamber of the mass spectrometer through a heated stainless steel sampling capillary (0.43 mm i.d.) maintained at an external temperature of 66 °C. The gaseous ions sampled by the capillary ($\pm$48 V) were transmitted through a skimmer ($\pm$4 V) and accumulated for 2 - 5 s in an rf hexapole (600 V p-p). The ions were subsequently ejected from the hexapole and injected at $\pm$2700 V into the bore of the superconducting magnet, decelerated and introduced into the ion cell. Two flexible heating blankets placed around the portion of the vacuum tube that surrounds the ion cell controlled the temperature of the ion cell for the BIRD experiments. The typical base pressure for the instrument was ~5 x 10^{-10} mbar. Data acquisition was performed using the XMASS software (version 5.0). The time-domain signal consisted of the sum of 30 transients containing 128 K data points per transient.

5.3 Results and Discussion

5.3.1 Influence of Solution Conditions on the Assembly of the Stx1 and Stx2 B Subunits

To establish whether the structural homologies observed in their X-ray crystal structures translate to comparable thermodynamic stability in solution, we investigated the influence of subunit concentration, temperature, ionic strength and pH on the assembly of the Stx1 and Stx2 B subunits in aqueous solution.

131

5.3.1.1 Influence of B Subunit Concentration

NanoES mass spectra were recorded in positive and negative ion modes for aqueous solutions of Stx1 B or Stx2 B subunits at concentrations ranging from 5 - 85 μM, with 25 mM ammonium acetate at pH 7 and 25 °C (Figures 5.1, 5.2). Under the solution conditions investigated, only ions corresponding to the B_5 homopentamer of Stx1 were observed in the mass spectra. No ions corresponding to monomers, dimers, trimers or tetramers were detected in these experiments. In positive ion mode, the Stx1 B pentamer was observed predominantly as the protonated ion, $(B_5 + nH)^{+n} \equiv B_5^{+n}$ where n = 12 - 14 (Figure 5.1a), although small amounts of alkali metal ion adducts were observed at the lower subunit concentrations investigated (Figure 5.1b). In negative ion mode, the Stx1 B pentamer was observed almost exclusively as the deprotonated ion, $(B_5 - nH)^{-z} \equiv B_5^{-z}$ ions where z = 12 - 14 (Figure 5.1c). These data suggest that the Stx1 B subunit existed almost exclusively in its pentameric form under the solution conditions examined. Attempts to induce disassembly of the pentamer through dilution were unsuccessful. Dilution of the sample to subunit concentrations < 1 μM led to a significant degradation of the signal-to-noise ratio (S/N) of the spectra making it impossible to positively identify any B subunit ions. Consequently, it was not possible to establish whether assembly of Stx1 B into pentamers was reversible under these conditions.

In contrast to what we observed with the Stx1 B subunit, the assembly of Stx2 B subunit was found to be exquisitely sensitive to concentration. At the highest Stx2 B subunit concentrations investigated, 65 μM, the protonated B_5^{+n} ions, where n = 11 - 14, constituted the major ions observed in positive ion mode. However, ions corresponding to dimer (B_2^{+7}), trimer (B_3^{+9}, B_3^{+10}) and tetramer (B_4^{+10}, B_4^{+11}) were also clearly evident,

132

Figure 5.1 NanoES mass spectra of aqueous solutions of the Stx1 B acquired in positive mode at a subunit concentration of (a) 85 μM and (b) 4 μM, and in the negative mode at (c) 25 μM. All solutions contained 25 mM ammonium acetate and were at pH 7 and 25 °C.
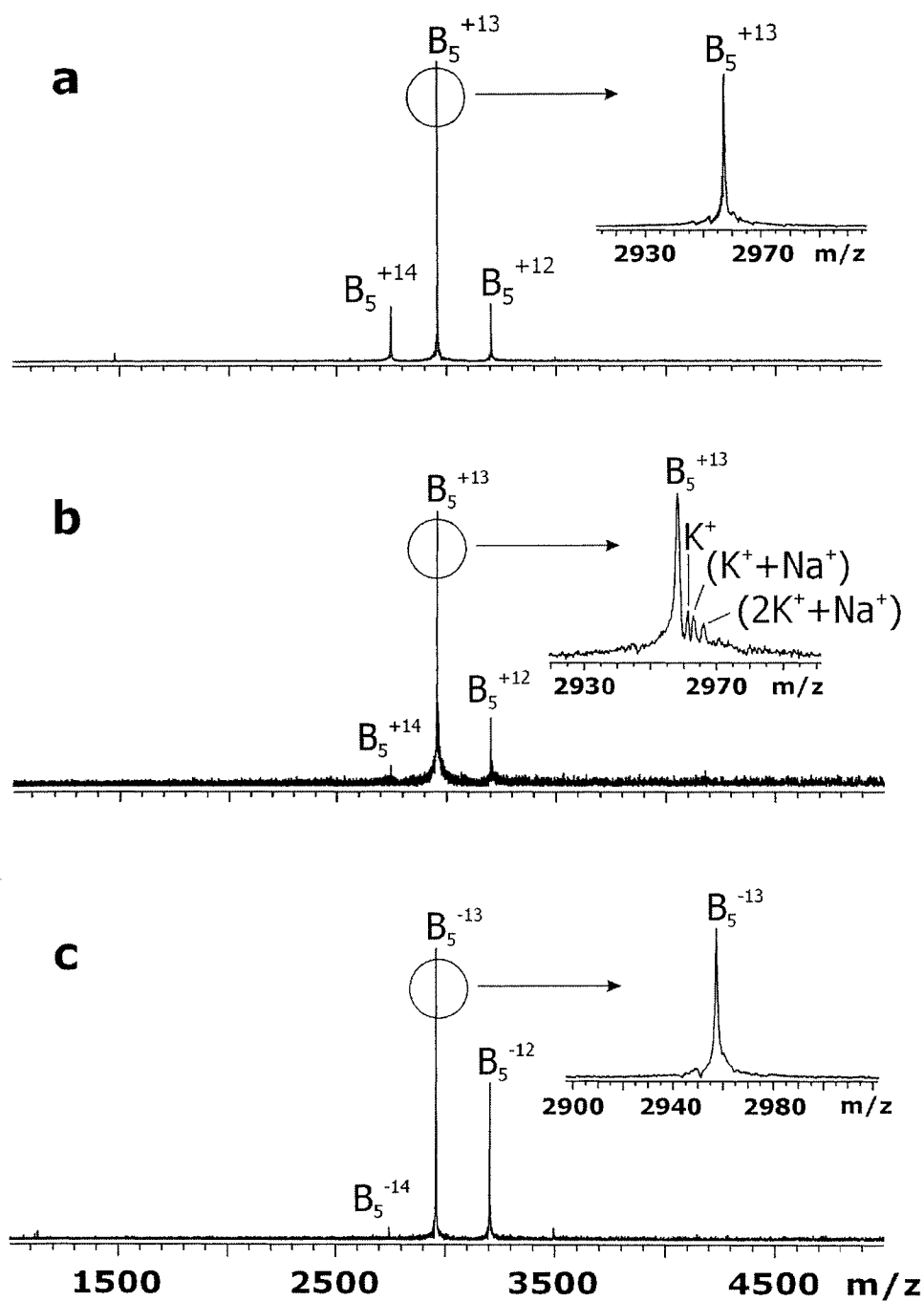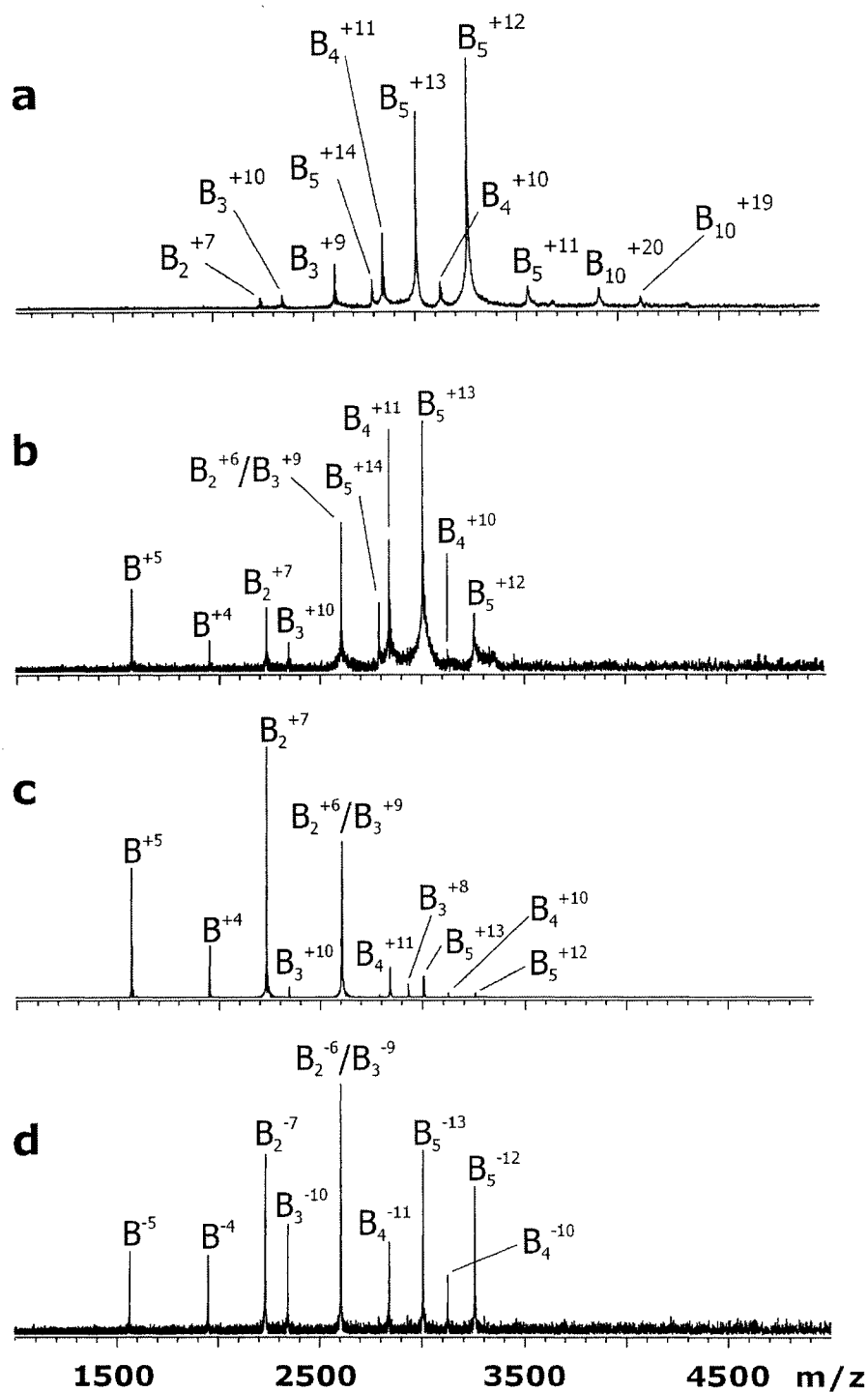
133

Figure 5.2 NanoES mass spectra of aqueous solutions of the Stx2 B acquired in positive ion mode at a subunit concentration of (a) 65 μM, (b) 48 μM and (c) 25 μM, and in negative mode at (d) 48 μM. All solutions contained 25 mM ammonium acetate and were at pH 7 and 25 °C.

134

albeit at lower abundance (Figure 5.2a). Interestingly, ions corresponding to the homodecamer, B_{10}^{+19} and B_{10}^{+20}, were also present in the spectra. The formation of the Stx2 B decamer has not, to our knowledge, been previously observed. It is possible that the decamer ions result from nonspecific dimerization of two pentamers during the nanoES process. Several laboratories have previously demonstrated that nonspecific protein complexes can form during the ES process [26, 27]. It has also been shown that the tendency for nonspecific binding is strongly dependent on analyte concentration, with higher concentrations leading to more extensive nonspecific complexes [28, 29]. While the possibility that the decamer was formed by nonspecific interactions can not be conclusively ruled out, it is, in our opinion, unlikely given that there was no evidence of the corresponding Stx1 B decamer ions, despite the higher concentrations of Stx1 pentamer in the nanoES solution. The present results suggest, therefore, that the decameric species observed for the Stx2 B subunit originated in solution.

Dilution of the Stx2 B subunit sample resulted in a decrease in the relative abundance of the pentamer, as well as the disappearance of the decamer, and a concomitant increase in the abundance of the smaller multimers and the appearance of B^{+4} and B^{+5} monomer ions (Figures 5.2b, c). Mass spectra acquired in negative ion mode were found to closely resemble the spectra measured in the positive ion mode, both in terms of the ions present and their relative abundance (Figure 5.2b, d). It should be noted that the nanoES mass spectra shown in Figure 5.2 were acquired after allowing the nanoES solutions to stand for more than 10 min after diluting the stock solution. This was done to ensure an equilibrium distribution of the different oligomeric forms of the B subunits in the nanoES solution. Mass spectra acquired at shorter times were found to

135

exhibit a striking dependence on spray time. Shown in Figure 5.3 are mass spectra acquired in positive ion mode at different spray times (while continuously spraying the solution), immediately following the preparation of a 25 μM solution of the Stx2 B subunit with 10 mM ammonium acetate. The mass spectra acquired immediately after preparation of the nanoES solution suffered from poor S/N. However, ions believed to correspond to B_5^{+n}, at charge states n = 11 - 13, and the B^{+5} monomer were observed (Figure 5.3a). The peaks corresponding to the B_5^{+n} ions are very broad and the ions are believed formed with a varying number of adducts. Due to limitations in the mass resolution achievable with the FT-ICR/MS used in the present work, the adducts could not be positively identified. However, several groups previously reported observing gaseous protein complex ions with extensive adducts, which they suggested to correspond to neutral or charged buffer species and alkali metal ions present in solution and, possibly, solvent molecules which were kinetically trapped within the complex [30 - 35]. In an effort to remove the adducts from the B_5^{+n} ions, the ions were heated in the ion cell with blackbody radiation prior to detection. Shown in Figure 5.4 are mass spectra obtained for the B_5^{+10} and B_5^{+11} ions before and after heating the ions for 5 s at a cell temperature of 160 °C. It can be seen that there is little change in the width of the peaks, indicating that the adducts are kinetically quite stable. Consequently, it is unlikely that the adducts are solvent molecules or neutral buffer components, since these would be expected to readily dissociate from the protein ions in the heated ion cell [36]. With increasing spray duration, the relative abundance of the Stx2 B pentamer ions decreased and concomitantly, ions corresponding to monomer (B^{+5} and B^{+4}), dimer (B_2^{+6} and B_2^{+7}), trimer (B_3^{+9} and B_3^{+10}) and tetramer ions (B_4^{+10} and B_4^{+11}) (Figures 5.3b, c) appeared in

136
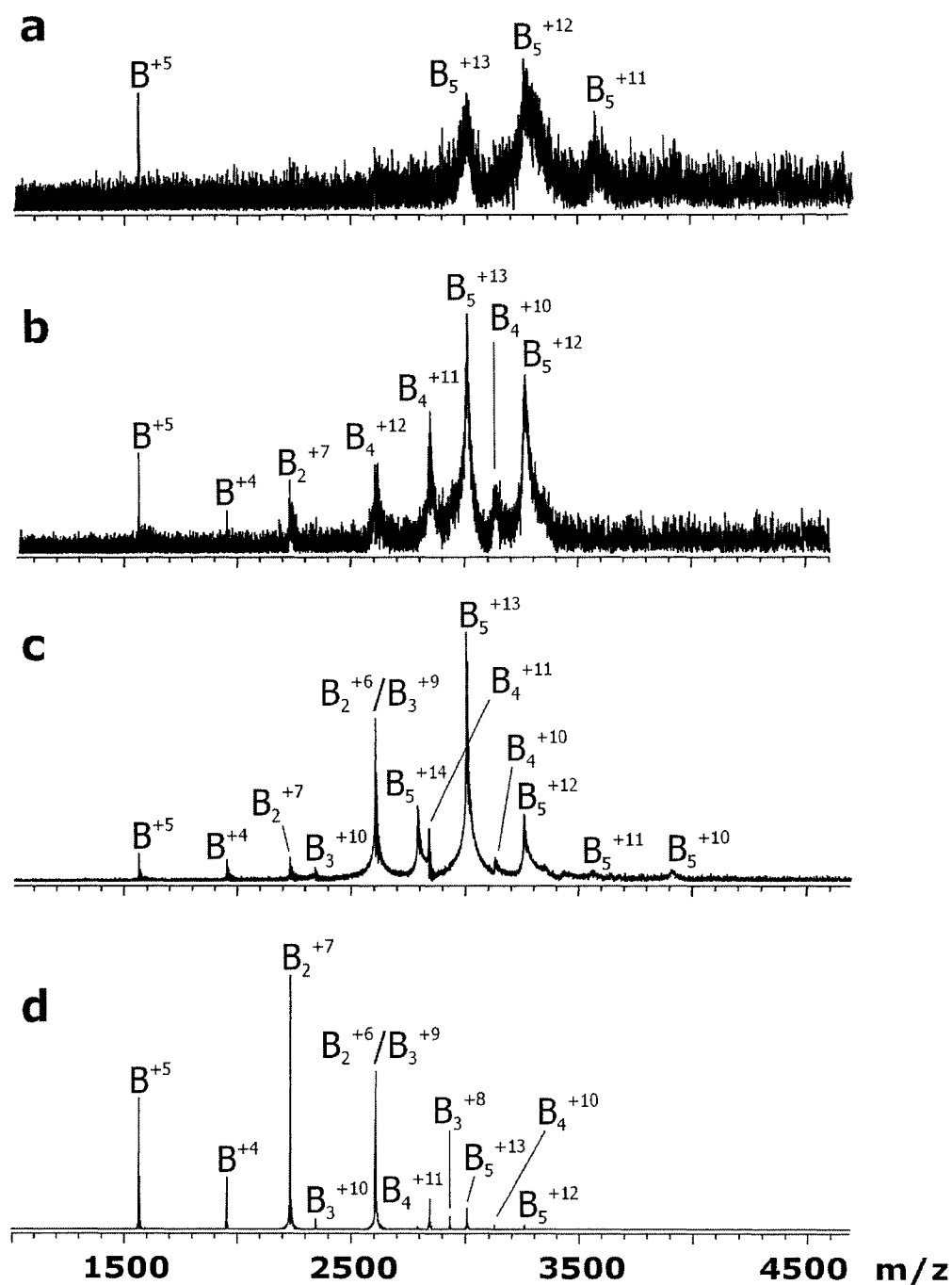
Figure 5.3 NanoES mass spectra of aqueous solutions of the Stx2 B (25 µM) in 10 mM ammonium acetate obtained in the positive mode immediately after preparing the sample solution (a) and after different spray time intervals of 3 min (b), 6 min (c) and 10 min (d). The solution contained 10 mM ammonium acetate and was at pH 7 and 25 °C.

137
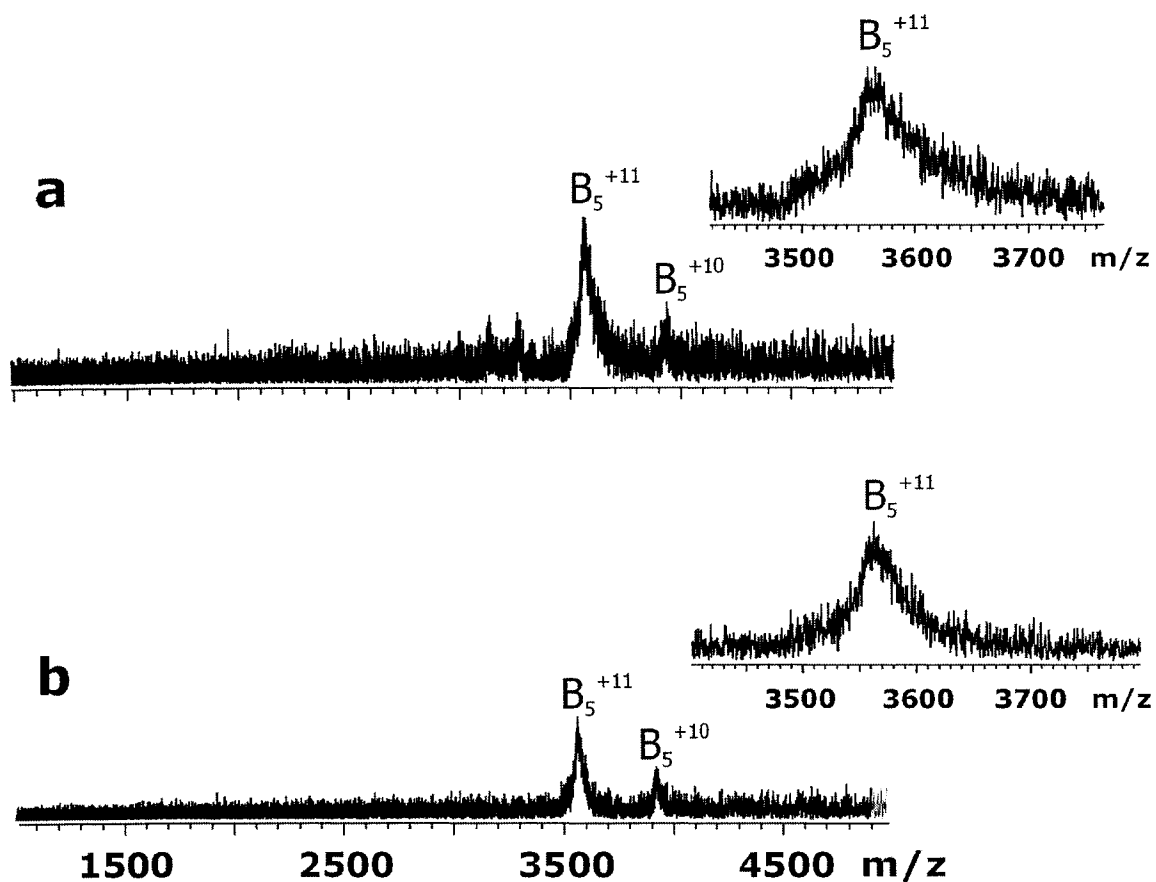
Figure 5.4 (a) NanoES spectrum acquired in positive ion mode for an aqueous solution of Stx2 B (25 μM) and 10 mM ammonium acetate at pH 7 and 25 °C; (b) BIRD snapshot mass spectrum obtained for the Stx2 B_5^{+10} and B_5^{+11} ions after heating for 5 s at a cell temperature of 160 °C.

the mass spectra. Interestingly, the longer spray times also resulted in a noticeable reduction in the abundance of adducts of the pentamer and smaller multimers. This phenomenon, which to our knowledge has not been previously described, was observed at all solution conditions investigated but was most noticeable at the lowest Stx2 B subunit concentration (25 µM), where little pentamer is present at equilibrium. Although the origin of this phenomenon is not known, it may arise from changes in the conformation of the B subunits in solution, perhaps due to the lower ionic strength of the diluted sample solution. At a spray time of ~10 min, the major ions observed in the mass spectra corresponded to protonated monomer ions and smaller oligomer ions, with very little pentamer present (Figure 5.3d). Mass spectra recorded at longer spray times did not exhibit any further changes indicating that an equilibrium distribution of the different forms of the B subunit was achieved after ~10 min.

The differences in the nanoES mass spectra recorded for solutions of the Stx1 and Stx2 B subunits strongly suggest that the thermodynamic stability of the homopentamers differ, at least under the solution conditions investigated. However, when evaluating protein oligomerization by ES/MS it is important to be vigilant against spectral artifacts arising from the ES process, such as nonspecific binding and gas phase dissociation reactions in the ion source. It is possible, that the spectral differences observed for the Stx1 and Stx2 B subunits originated from dissociation of the Stx2 B pentamer ions during sampling into the mass spectrometer. As described previously, the internal energy of gaseous ions sampled into the ion source of the mass spectrometer used for the present measurements is most significantly influenced by energetic collisions within the rf hexapole used to accumulate them [28]. Collisional heating during the accumulation

139

event may induce dissociation of the B_5^{+n} ions and smaller multimers, if present. In a previous study, it was shown that the +9 to +11 ions of a 27 kDa protein-trisaccharide complex had an effective temperature of ~140°C in the hexapole region at accumulation times $\geq$ 2 s [28]. The B_5^{+n} ions investigated here are also expected to be collisionally-heated in the hexapole, although because of their larger mass (39 kDa) they may experience lower effective temperatures. To establish whether the Stx2 B_5^{+n} ions, and smaller multimers, if present, undergo collision-induced dissociation in the source, the accumulation time was varied from 2 to 5 s. Shown in Figure 5.5 are mass spectra acquired for a 65 μM solution of the Stx2 B subunit with a hexapole accumulation time of 2 and 5 s. It can be seen that there is no significant difference in the mass spectra recorded at different accumulation times suggesting that gas phase dissociation of the Stx2 B_5^{+n} ions in the source does not occur to any appreciable extent. However, it is possible that some of the B_5^{+n} ions have lifetimes much shorter than the minimum sampling time (~2 s) and dissociate in the source region.

To more convincingly demonstrate that gas phase dissociation reactions do not contribute to the appearance of the Stx2 B subunit mass spectra, time-resolved BIRD experiments were performed on the protonated Stx2 B_5^{+12} and B_5^{+13} ions at temperatures ranging from 120 to 180 °C. Illustrative BIRD spectra are shown in Figure 5.6a, c. It can be seen that the Stx2 B_5^{+n} ions dissociated preferentially by the loss of a single B subunit, which was ejected with a significant fraction of the total charge available. Such "asymmetric" dissociation is known to be general for gaseous multiprotein complexes, independent of the number of subunits contained within the complex [22, 37, 38].

140
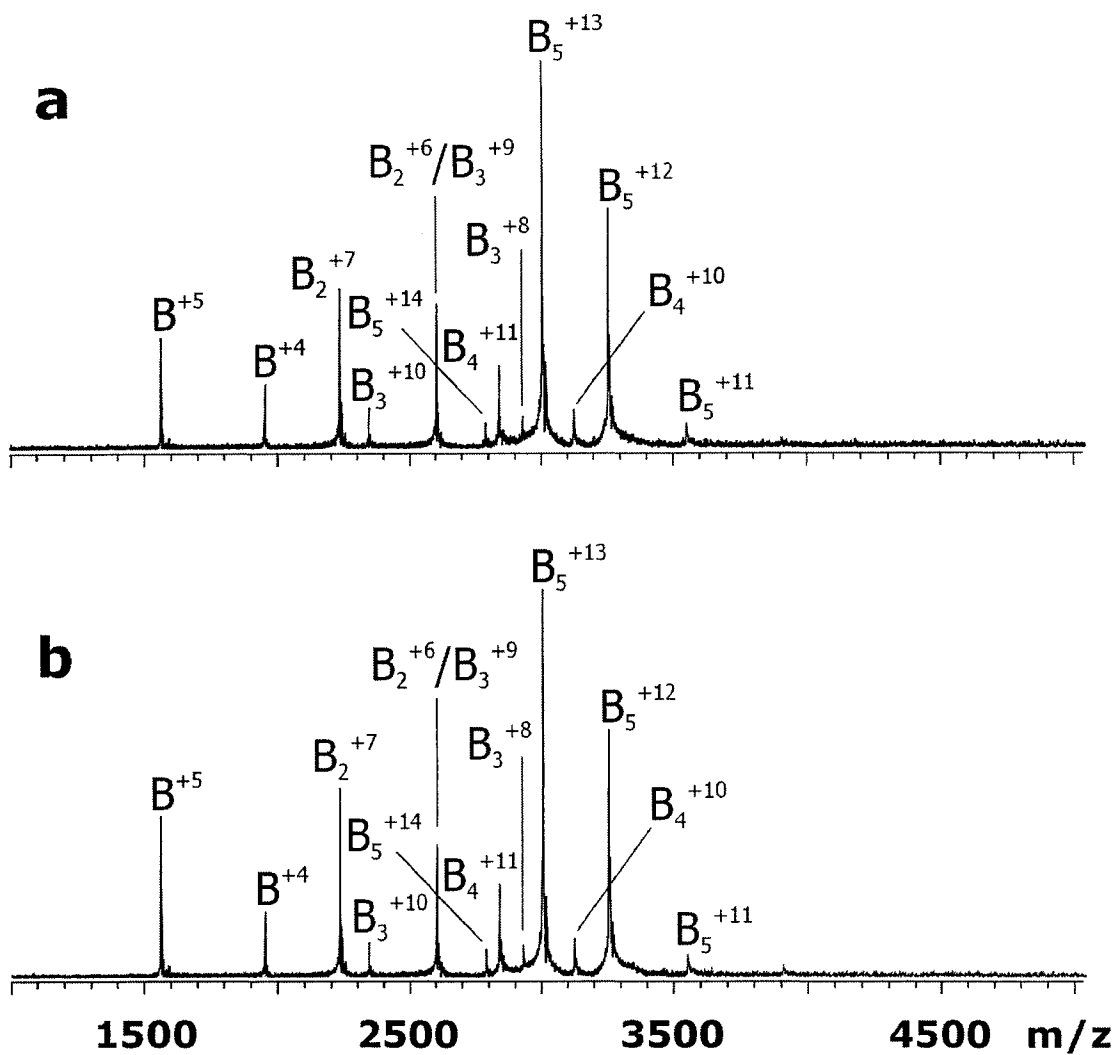
Figure 5.5 NanoES mass spectra acquired for an aqueous solution of Stx2 B (65 μM) with a hexapole accumulation time of (a) 2 s and (b) 5s.

141
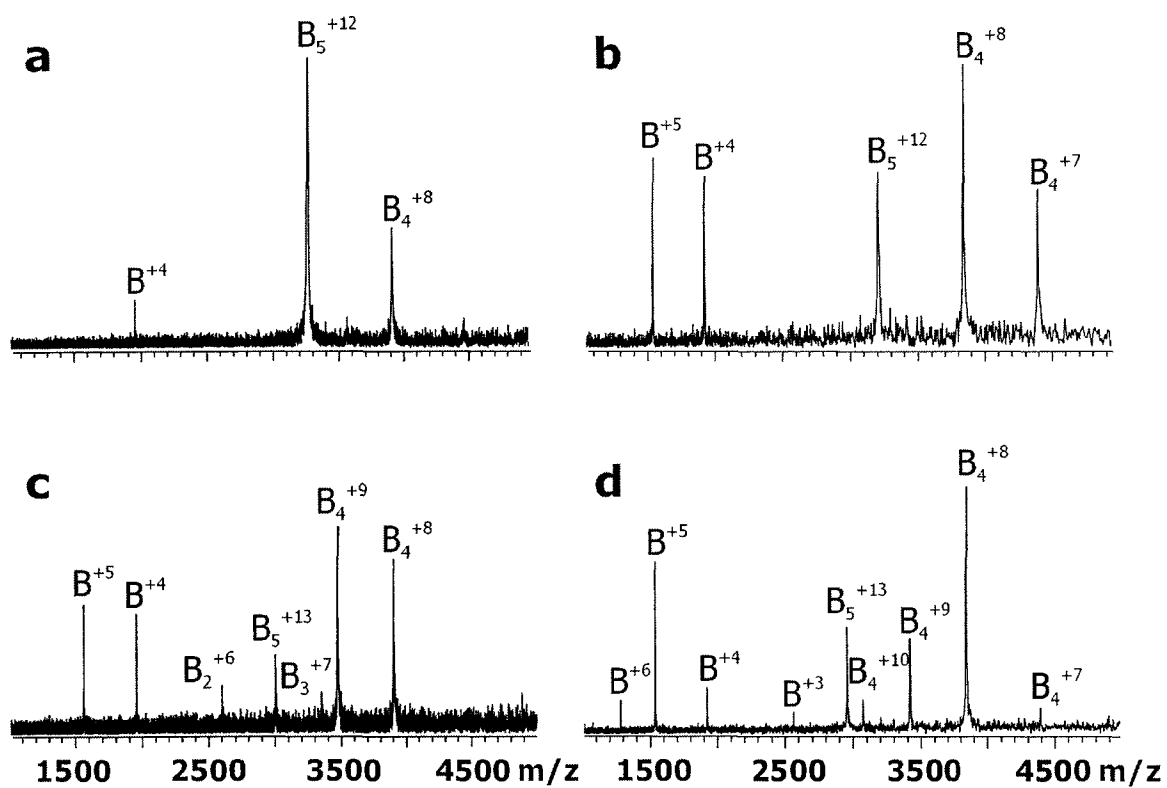
Figure 5.6 BIRD mass spectra of the protonated pentamer ions, Stx1 B_5 and Stx2 B_5, at charge states +12 and +13: (a) Stx2 B_5^{+12} and (b) Stx1 B_5^{+12} at a cell temperature of 170 °C and a reaction time 1.5 s; (c) Stx2 B_5^{+13} and (d) Stx1 B_5^{+13} at a cell temperature of 155 °C and a reaction time 3 s.

142

Dissociation of the Stx2 B_5^{+12} ion proceeded exclusively by the loss of a monomer at the +4 charge state (eq 5.1):

$$(\text{Stx2})\ B_5^{+12} \rightarrow B^{+4} + B_4^{+8} \tag{5.1}$$

Dissociation of the Stx2 B_5^{+13} proceeded preferentially by the loss of monomer at the +5 and +4 charge states (eq 5.2a, b). However, a second, but minor dissociation pathway, resulted in the formation of dimers and trimers at charge states +6 and +7, respectively (eq 5.2c).

$$(\text{Stx2})\ B_5^{+13} \rightarrow B^{+4} + B_4^{+9} \tag{5.2a}$$

$$\rightarrow B^{+5} + B_4^{+8} \tag{5.2b}$$

$$\rightarrow B_2^{+6} + B_3^{+7} \tag{5.2c}$$

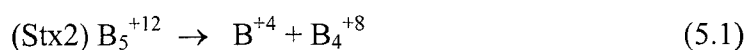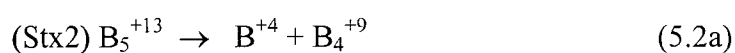BIRD measurements performed on the corresponding Stx1 B_5 ions were previously reported [22]. Illustrative spectra are shown in Figures 5.6b, d for comparison purposes. It can be seen that the dissociation pathways are quite similar, although charge enrichment of the ejected monomer is more pronounced in the case of the Stx1 B_5^{+n} ions. Although the monomer charge states observed in the BIRD spectra of the Stx2 B_5^{+n} ions are consistent with the charge observed in the nanoES mass spectra of the Stx2 B subunit (Figure 5.2), the tetramer ion charge states are not. More importantly, the abundant dimer and trimer ions observed in the nanoES mass spectra are inconsistent with the BIRD results, in which the production of dimer and trimer ions represents a minor dissociation pathway. Based on the BIRD data, as well as the insensitivity of the nanoES mass spectra to the source conditions, it is concluded that the monomer and small multimers observed in the spectra of the Stx2 B subunit originated from solution and not from gas phase dissociation of the Stx2 B_5^{+n} ions in the ion source.

143

The influence of subunit concentration on the relative abundance of the different multimeric forms of the Stx B subunits indicates that assembly into pentamer is fully reversible and that the different oligomeric forms co-exist at equilibrium. It is important to note that, because of anticipated differences in ionization efficiencies of the different oligomeric forms of the B subunit resulting from differences in their size and chemical properties (*e.g.* surface activity), the relative abundance of the subunit ions observed in the mass spectra likely does not reflect, quantitatively, their relative abundance in solution.

5.3.1.2 Influence of Temperature

To assess the influence of temperature on the quaternary structure of the Stx B subunits, nanoES mass spectra were measured for solutions of Stx1 B and Stx2 B subunits at solution temperatures ranging from 0 - 60 °C using a temperature-controlled nanoES device developed in our laboratory. It should be noted that Robinson and coworkers have previously reported the design of a temperature-controlled nanoES device and its application to the study of the assembly/disassembly of multimeric protein complexes by nanoES/MS [39-41]. Over the range of temperatures investigated, assembly of Stx1 B subunit exhibited only a minor dependence on temperature. Shown in Figures 5.7a, b are mass spectra acquired for a solution of 85 μM Stx1 B subunit at 2 and 58 °C, respectively. The mass spectra measured at 2 °C are virtually indistinguishable from those acquired at 25 °C, Figure 5.1, with only B_5^{+n} ions, at n = 11 - 13, observed. At 58 °C, the Stx1 B_5^{+n} ions represent the most abundant species present, although there was a noticeable shift in the charge state distribution to n = 12 - 15 and a significant increase in the abundance of alkali metal ion adducts. In addition, Stx1 B^{+4} and B^{+5} ions were also

144

evident, albeit at low abundance, but there was no evidence of corresponding tetramer ions. The shift to higher charge states is consistent with the thermal-induced unfolding of subunits within the pentamer and suggests that disassembly of the pentamer is promoted by the loss of structure of the subunits. In contrast to the Stx1 B subunit, the quaternary structure of the Stx2 B subunit exhibited striking temperature dependence. Shown in Figures 5.7c, d are mass spectra acquired for a solution of 65 μM Stx2 B at 8 and 57 $^{\circ}$C, respectively. At 8 $^{\circ}$C, the mass spectra revealed the presence of five different oligomeric states of Stx2 B subunit, monomer through pentamer. The charge states were similar to those observed at 25 $^{\circ}$C (Figure 5.2). At 57 $^{\circ}$C, the dominant Stx2 B subunit ions correspond to monomers, with small amounts of the other oligomeric forms. There was no significant difference in the charge states observed at low and high solution temperatures which suggests that disassembly of the Stx2 B pentamer is not accompanied by significant unfolding of the subunits. The influence of solution temperature on the assembly of the Stx2 B subunit is more clearly seen in Figure 5.8a where the fractions of Stx2 B subunits in the different oligomeric states are plotted versus solution temperature. Figure 5.8b illustrates the effect of solution ionic strength on the stability of the Stx2 B pentamer. It can be seen that at higher concentrations of ammonium acetate (34 mM versus 18 mM) the pentamer is more stable at solution temperatures higher than 35 $^{\circ}$C. The influence of salt concentration on the stability of the Stx2 B pentamer highlights the importance of electrostatic interactions between subunits for their association into the pentameric complex.

145
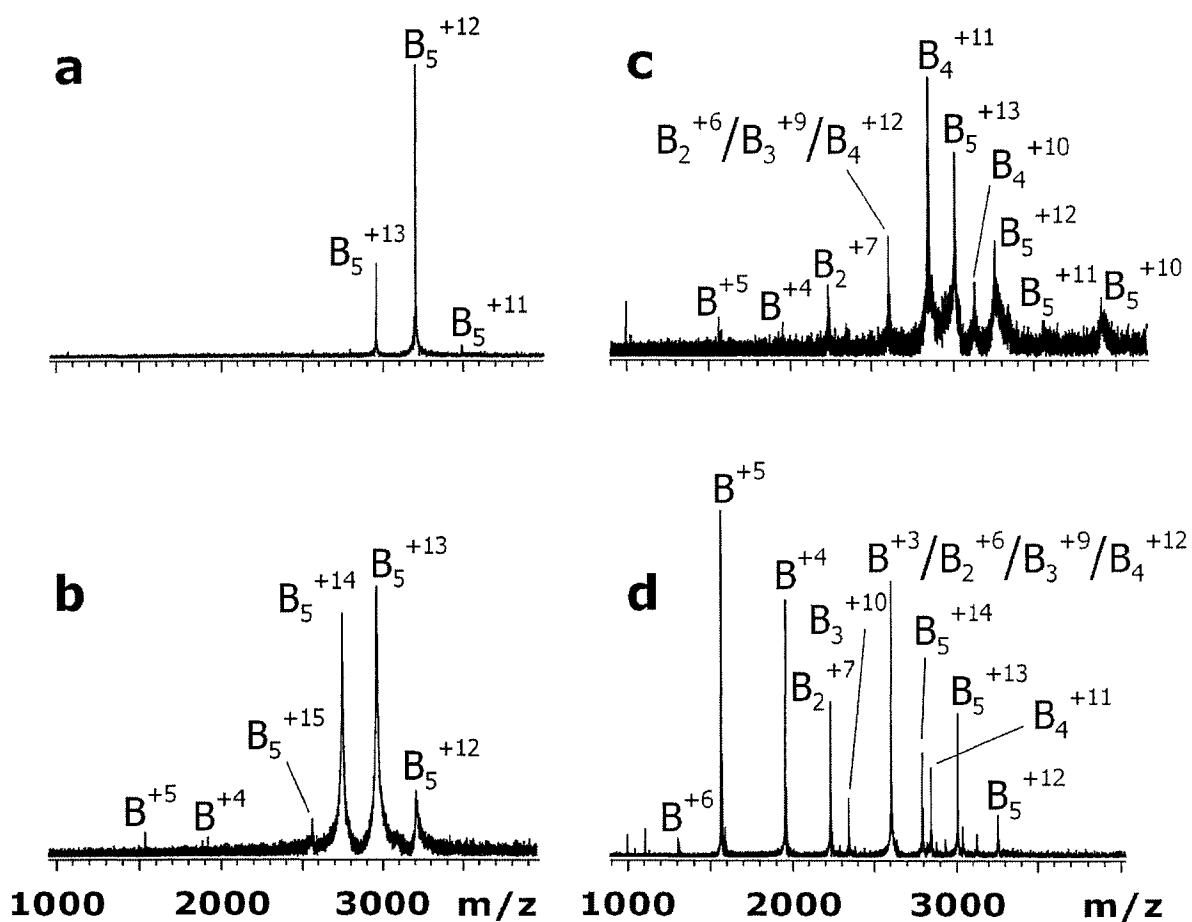
Figure 5.7 NanoES mass spectra of aqueous solutions of Stx1 B (85 μM) at solution temperatures of (a) 2 °C and (b) 58 °C, and of Stx2 B (85 μM) at solution temperatures of (c) 8 °C and (d) 57 °C.
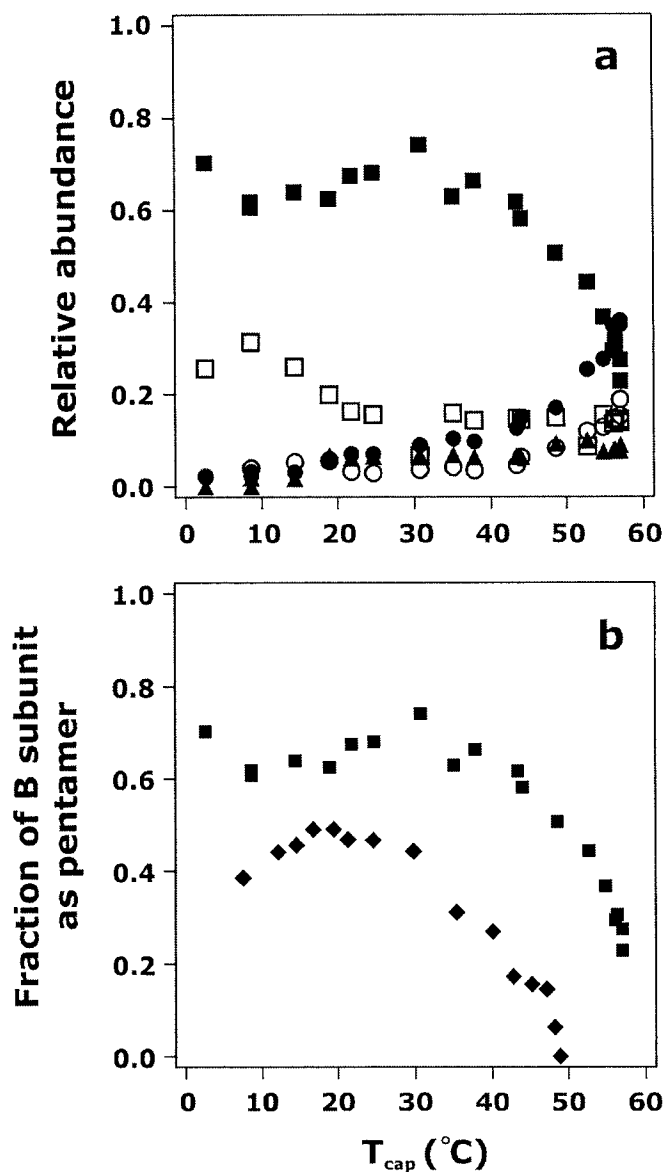
Figure 5.8 Influence of solution temperature on the assembly of the B subunit of Stx2 as monitored by nanoES/MS. (a) The relative abundance of monomer (●), dimer (○), trimer (▲), tetramer (□) and pentamer (■) determined for an aqueous solution of Stx2 B (85 μM) and ammonium acetate (34 mM) at different solution temperatures. (b) The fraction of Stx2 B subunit (85 μM) present in solution as pentamer as a function of solution temperature at two different concentrations of ammonium acetate: 18 mM (◆) and 34 mM (■).

147

5.3.1.3 Influence of pH

The influence of pH on the assembly of the Stx B subunits at 25°C was also investigated. Shown in Figure 5.9 are mass spectra acquired for solutions of the Stx1 (65 μM) and Stx2 B (65 μM) subunits at pH 4.0. In the case of the Stx1 B subunit, acidification results in the appearance of monomer, dimer, trimer, and tetramer ions (Figure 5.9a). Similar behaviour was observed for the Stx2 B subunit (Figure 5.9b). Interestingly, the differential stability of the Stx1 and Stx2 B subunits was less noticeable in acidified solutions. Under basic conditions (pH 9) the stability of both the Stx1 and Stx2 B pentamers was similar to what we observed when the experiments were performed at pH 7.

The acid-induced disassembly of the Stx1 pentamer may provide new insight into the origin of the loss of binding reported for the Stx1 B subunit - P^k trisaccharide complex under acidic conditions. Using isothermal titration calorimetry, Toone and coworkers found that binding between the Stx1 B subunit and the P^k trisaccharide is lost at pH < 5 [42]. It was proposed that protonation of a group of aspartate residues, believed to be important in the recognition of the P^k trisaccharide, was responsible for the loss of binding. However, the present results suggest that disassembly of the pentamer may be responsible for the loss of binding under acidic conditions. The similar stabilities of the pentamers of the B subunits of Stx1 and Stx2 observed under acidic conditions, together with sensitivity of Stx2 B subunit assembly to the presence of salt, suggests a possible role of destabilizing electrostatic interactions between an acidic residue, Asp70, located at its C-terminal end of Stx2 B and an acidic residue, Glu9, of the neighboring subunit as a likely cause of the differences in the assembly of the B subunits of Stx1 and Stx2.
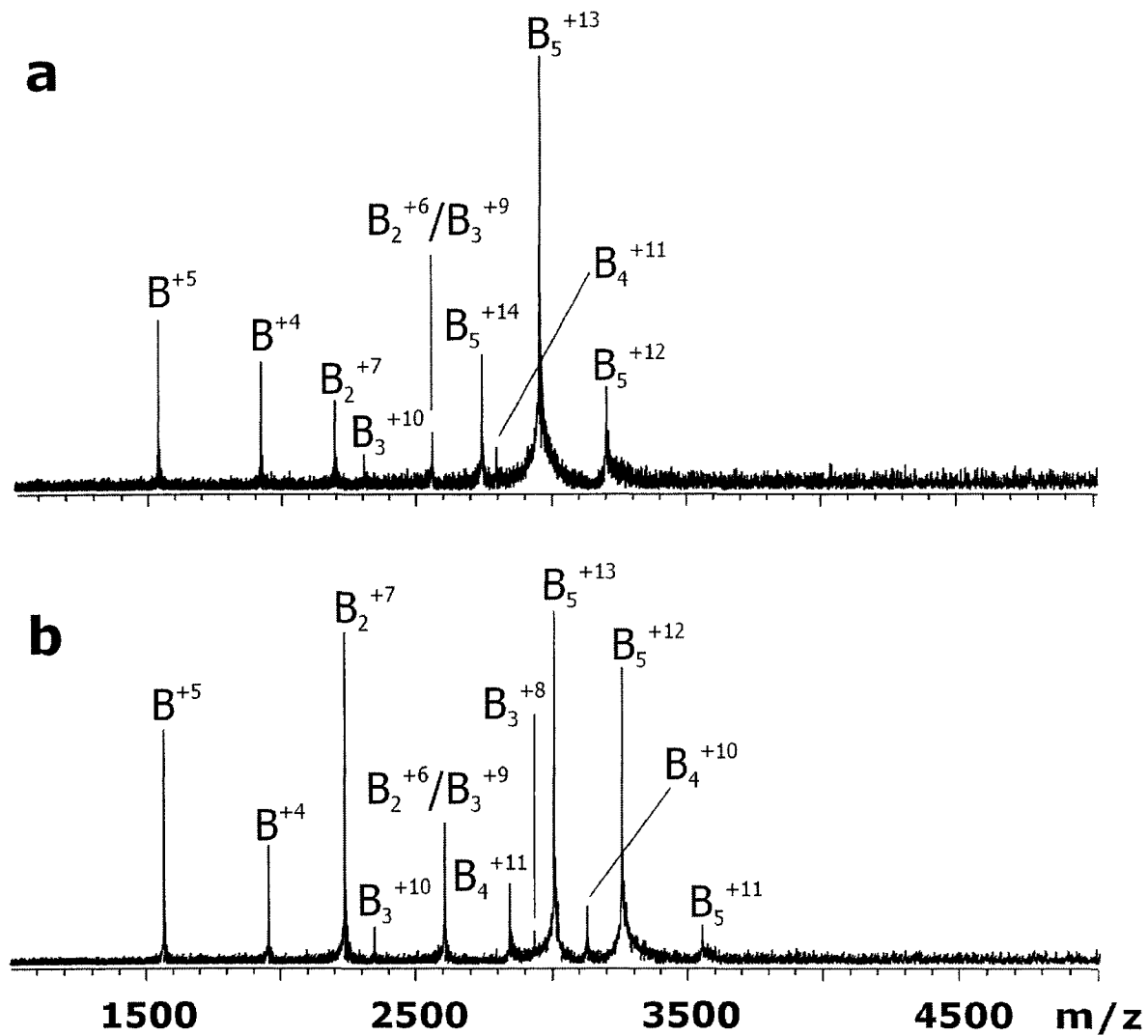
148

Figure 5.9 NanoES mass spectra of aqueous solutions of (a) Stx1 B (65 μM) and (b) Stx2 B (65 μM) with 25 mM ammonium acetate at pH 4.

149

In this regard, the Stx1 B subunit has a basic amino acid, Arg69, at its C-terminal end. Both the increased protonation (neutralization) of the acidic residues at low pH, as well as screening of electrostatic interactions at higher salt concentrations, is expected to eliminate or reduce the effects of the repulsive Asp70 - Glu9 interaction, in agreement with the experimental observations. Of course, protonation of the acidic residues would also result in a reduction of the stabilizing electrostatic interactions (*i.e.* salt bridges) [43, 44]. Consequently, the overall stability of Stx2 B pentamer would be expected to decrease with decreasing pH, which is consistent with our experimental observations.

Upon binding to their cell surface Gb3 receptors, Stx1 and Stx2 are believed to be internalized into endosomes which then transport the toxins, via a unique Golgi-directed bypass pathway, to their intracellular destination, the endoplasmic reticulum [45]. This unique trafficking pathway may prevent these holotoxins from being exposed to the degradative environment of the late endosome/pre-lysosome compartment. Acidification of the endosomal compartment is apparently required for these vesicles to access this bypass pathway [45]. The reduced stability of the Stx1 and Stx2 B subunits at pH 4, as observed in the nanoES/MS experiments may, therefore, be functionally important if disassembly of the holotoxins is also a necessary step in the cellular intoxication process.

5.4   Conclusions

NanoES and FT-ICR/MS mass spectrometry were used to investigate the stability of the B_5 homopentamer of Stx1 and Stx2 in aqueous solution. Despite the structural similarities suggested by their respective X-ray crystal structures, oligomerization of the B-subunits differs in solution, at least under the conditions investigated. At subunit

concentrations of 5 - 85 µM and temperatures ranging from 0 to 60 °C, the Stx1 B subunit exists almost exclusively in its pentameric form at neutral pH. Acidification was found to promote disassembly. In contrast, although the Stx2 B subunit forms abundant pentamer (~80%) at subunit concentrations of ~65 µM, neutral pH, ambient temperature and relatively high salt concentration, it dissociates into smaller oligomers and monomers when one or more of these parameters were altered. The lower thermodynamic stability of the B subunits of Stx2, compared to Stx1, is a significant finding since it may provide an explanation for the greater toxicity of Stx2 relative to Stx1. In an effort to establish whether a link between the stability of Stx B subunits and holotoxin toxicity exists, our laboratory has undertaken a comparative study of the stabilities of a number of mutant B subunits and the toxicities of the corresponding mutant holotoxins.

5.5   Acknowledgments

The author thanks E. N. Kitova for her contribution to this work.

151

5.6 Literature Cited

(1) Karmali, M. A. *Mol. Biotechnol.* **2004**, *26*, 117-122.

(2) Nataro, J. P.; Kaper, J. B. *Clin. Microbiol. Rev.* **1998**, *11*, 142-201.

(3) Fraser, M. E.; Chernaia, M. M.; Kozlov, Y. V.; James, M. N. *Nat. Struct. Biol.* **1994**, *1*, 59-64.

(4) Fraser, M. E.; Fujinaga, M.; Cherney, M. M.; Melton-Celsa, A. R.; Twiddy, E. M.; O'Brien, A. D.; James, M. N. *J. Biol. Chem.* **2004**, *279*, 27511-27517.

(5) Ling, H.; Boodhoo, A.; Hazes, B.; Cummings, M. D.; Armstrong, G. D.; Brunton, J. L.; Read, R. J. *Biochemistry* **1998**, *37*, 1777-1788.

(6) Calderwood, S. B.; Auclair, F.; Donohue-Rolfe, A.; Keusch, G. T.; Mekalanos, J. J. *Proc. Natl. Acad. Sci. U.S.A.* **1987**, *84*, 4364-4368.

(7) Strockbine, N. A.; Jackson, M. P.; Sung, L. M.; Holmes, R. K.; O'Brien, A. D. *J. Bacteriol.* **1988**, *170*, 1116-1122.

(8) Boodhoo, A.; Read, R. J.; Brunton, J. *J. Mol. Biol.* **1991**, *221*, 729-731.

(9) Richardson, J. M.; Evans, P. D.; Homans, S. W.; Donohue-Rolfe, A. *Nat. Struct. Biol.* **1997**, *4*, 190-193.

(10) Hashimoto, H.; Mizukoshi, K.; Nishi, M.; Kawakita, T.; Hasui, S.; Kato, Y.; Ueno, Y.; Takeya, R.; Okuda, N.; Takeda, T. *Pediatrics* **1999**, *103*, E2.

(11) Head, S. C.; Petric, M.; Richardson, S.; Roscoe, M.; Karmali, M. A. *Microbiology Letters* **1988**, *51*, 211-215.

(12) Kleanthous, H.; Smith, H. R.; Scotland. S. M.; Gross, R. J.; Rowe, B.; Taylor, C. M.; Milford, D. V. *Arch. Dis. Child* **1990**, *65*, 722-727.

(13)   Ostroff, S. M.; Tarr, P. I.; Neill, M. A.; Lewis, J. H.; Hargrett-Bean, N.; Kobayashi, J. M. *J. Infect. Dis.* **1989**, *160*, 994-998.

(14)   Scotland, S. M.; Willshaw, G. A.; Smith, H. R.; Rowe, B. *Epidemiol. Infect.* **1987**, *99*, 613-624.

(15)   Siegler, R. L.; Obrig, T. G.; Pysher, T. J.; Tesh, V. L.; Denkers, N. D.; Taylor, F. B. *Pediatr. Nephrol.* **2003**, *18*, 92-96.

(16)   Tesh, V. L.; Burris, J. A.; Owens, J. W.; Gordon, V. M.; Wadolkowski, E. A.; , A. D.; Samuel, J. E. *Infect. Immun.* **1993**, *61*, 3392-3402.

(17)   Wadolkowski, E. A.; Sung, L. M.; Burris, J. A.; Samuel, J. E.; O'Brien, A. D. *Infect. Immun.* **1990**, *58*, 3959-3965.

(18)   Head, S. C.; Karmali, M. A.; Lingwood, C. A. *J. Biol. Chem.* **1991**, *266*, 3617-3621.

(19)   Kitova E. N.; Kitov P. I.; Bundle D. R.; Klassen J. S. *Glycobiology* **2001**, *11*, 605-611.

(20)   Dunbar, R. C.; McMahon, T. B. *Science* **1998**, *279*, 194-197.

(21)   Price, W. D.; Schnier, P. D.; Jockusch, R. A.; Strittmatter, E. F.; Williams, E. R. *J. Am. Chem. Soc.* **1996**, *118*, 10640-10644.

(22)   Felitsyn, N. F.; Kitova, E. N.; Klassen, J. S. *Anal. Chem.* **2001**, 73, 4647-4661.

(23)   Marcato, P.; Mulvey, G.; Read, R. J.; Vander, H. K.; Nation, P. N.; Armstrong, G. D. *J. Infect. Dis.* **2001**, *183*, 435-443.

(24)   Mulvey, G.; Vanmaele, R.; Mrazek, M.; Cahill, M.; Armstrong, G. D. *J. Microbiol. Methods* **1998**, *32*, 247-252.

153

(25)   Daneshfar, R.; Kitova, E. N.; Klassen, J. S. *J. Am. Chem. Soc.* **2004**, *126*, 4786-
4787.

(26)   Versluis, C.; van der Staaij, A.; Stokvis, E.; Heck, A. J. R., de Craene, B. *J. Am. Soc. Mass Spectrom.* **2001**, *12*, 329-336.

(27)   Jurchen, J. C.; Williams, E. R. *J. Am. Chem. Soc.* **2003**, *125*, 2817-2826.

(28)   Wang, W. ; Kitova, E. N.; Klassen, J. S. *Anal. Chem.* **2003**, *75*, 4945-4955.

(29)   Wang, W.; Kitova, E. N.; Klassen, J. S. *Anal. Chem.* **2005**, 77, 3060-3071.

(30)   Loo, J. A. *Mass Spectrom. Rev.* **1997**, *16*, 1-23.

(31)   Nettleton, E. J.; Sunde, M.; Lai, Z. H.; Kelly, J. W.; Dobson, C. M.; Robinson, C. V. *J. Mol. Biol.* **1998**, *281*, 553-564.

(32)   Rostom, A. A.; Fucini, P.; Benjamin, D. R.; Juenemann, R.; Nierhaus, K. H.; Hartl, F. U.; Dobson, C. M.; Robinson, C. V. *Proc. Nat. Acad. Sci. USA* **2000**, *97*, 5185-5190.

(33)   Hanson, C. L.; Fucini, P.; Ilag, L. L.; Nierhaus, K. H.; Robinson, C. V. *J. Biol. Chem.* **2003**, *278*, 1259-1267.

(34)   Aquilina, J. A.; Robinson, C. V. *Biochem. J.* **2003**, *375*, 323-328.

(35)   Sobott, F.; McCammon, M. G.; Hernandez, H.; Robinson C. V. *Phil. Trans. R. Soc. B* **2005**, *363*, 379-389.

(36)   Peschke, M.; Verkerk, U. H.; Kebarle, P. *J. Am. Soc. Mass Spectrom.* **2004**, *15*, 1424-1434.

(37)   Light-Wahl, K. J.; Schwartz, B. L.; Smith, R. D. *J. Am. Chem. Soc.* **1994**, *116*, 5271-5278.

(38) Heck, A. J. R.; van den Heuvel, R. H. H. *Mass Spectrom. Rev.* **2004**, *23*, 368 - 389.

(39) Fandrich, M.; Tito, M. A.; Leroux, M. R.; Rostom, A. A.; Hartl, F. U.; Dobson, C. M., Robinson, C. V. *Proc. Nat. Acad. Sci. USA* **2000**, *97*, 14151-14155.

(40) Benesch, J. L. P.; Sobott, F.; Robinson, C. V. *Anal. Chem.* **2003**, 75, 2208-2214.

(41) Lentze, N.; Aquilina, J. A.; Lindbauer, M.; Robinson, C. V.; Narberhaus, F. *Eur. J. Biochem.* **2004**, *271*, 2494-2503.

(42) St. Hilaire, P. M.; Boyd, M. K.; Toone, E. J. *Biochemistry* **1994**, *33*, 14452-14463.

(43) Sinha, N.; Smith-Gill, S. J. *Curr. Protein Pept. Sci.* **2002**, *3*, 601-614.

(44) Yu, Y.; Monera, O. D.; Hodges, R. S.; Privalov, P. L. *J. Mol. Biol.* **1996**, *255*, 367-372.

(45) Natarajan, R.; Linstedt, A. D. *Mol. Biol. Cell* **2004**, *15*, 4798-4806.

Chapter 6

Conclusions and Future Work

The present work describes the development and application of MS-based approaches to the study stability of oligodeoxynucleotides (ODNs) and protein-ligand noncovalent complexes. Research work presented here included the study of the loss of neutral nucleobases from a series of thymine-rich (T-rich) 10-, 15- and 20-mer ODNs and influence of intramolecular interactions on dissociation kinetics and energetics (Chapters 2 and 3). In Chapter 4, association thermodynamic parameters, ΔH_{assoc} and ΔS_{assoc}, for protein-carbohydrate complexes were evaluated using a novel variable-temperature nanoelectrospray (nanoES) ionization device implemented with Fourier transform ion cyclotron mass spectrometer (FT-ICR/MS). The influence of solution conditions, such as temperature, protein concentration, pH, and ionic strength on the assembly of two structurally similar protein complexes were investigated using temperature-controlled nanoES-FT-ICR/MS (Chapter 5).

To elucidate the gas phase dissociation mechanism of ODNs, thermal decomposition of a series of T-rich doubly deprotonated 10-mer ODNs with a single reactive neucleobase (*i.e.* adenine, A, guanine, G, cytosine, C), at termini or internal positions, were studied using the BIRD technique in Chapter 2. Time-resolved blackbody infrared radiative dissociation (BIRD) experiments were used to evaluate dissociation kinetics and energetics for the loss of neutral nucleobase over the temperature range 120 - 190 °C. From the temperature dependence of the dissociation kinetics, Arrhenius activation parameters for the loss of specific nucleobases were determined for the first time. The dissociation kinetics and energetics for the loss of neutral nucleobase from a

156

given position within the ODNs were found to be sensitive to the identity of the base. In general, compared to A- and G-containing ODNs, the C-containing ODNs have been shown to have slower dissociation kinetics and higher activation energy values. The trends in the kinetic and energetic data were found to be different from previously reported results [1-4]. Moreover, the obtained energetic trend did not provide support for any of the commonly proposed mechanisms [3, 5]. It was suggested that the ability of nucleobases to participate in intermolecular interactions could influence the dissociation kinetics and energetics. The influence of length and charge state on dissociation kinetics and energetics, and stabilizing intramolecular interactions in the ODNs were examined in Chapter 3. We extended our ODN dissociation study to doubly and triply deprotonated T-rich 15- and 20-mer ODNs containing a single reactive base (A or C). The results from thermal dissociation experiments using BIRD technique revealed that of A-containing anions are significantly more reactive than the C-containing ions over the temperature range investigated. In contrast to the loss of CH from C-containing ions, Arrhenius parameters measured for the loss of AH exhibit strong dependence on size and, to some extent, charge state of the ODN. Based on determined preexponential (A-factor) values, the loss of CH is consistent with simple bond cleavage, but large A-factors measured for the 20-mer A-containing ions suggest that the reactive base experiences more internal solvation. However, results from hydrogen-deuterium exchange experiments on triply charged 20-mer A- and C-containing ions did not provide evidence for inherent differences in the internal solvation of A and C within the T-rich ODN anions. To further probe differences in internal solvation, Arrhenius parameters for the dissociation of noncovalent complexes of triply charged T_{20} and the neutral nucleobase AH and CH have

157

also been determined. Differences in the parameters indicate differences in the nature of the intramolecular interactions. It is proposed that neutral A-T interactions (*i.e.* base-base), which originate from solution, dominate in the case of the $(T_{20} + AH)^{-3}$ complex, while charge solvation, involving CH and a deprotonated phosphate group, is present for the $(T_{20} + CH)^{-3}$ complex.

A possible extension of this study is to use molecular dynamic simulations to examine the influence of conformation, sequence and charge distribution on conformation of T-rich ODN anions in the gas phase. Furthermore, as we explained in section 3.3.3, for sufficiently small strands (shorter than 10-mers) for which there is expected to be little or no contribution from solvation effects, the determination of dissociation activation energies may provide new insight into relative strength of the N-glycosidic bonds for different nucleobases.

In Chapter 4, we developed a novel temperature-controlled nanoES device to evaluate protein-carbohydrate binding affinities (K_{assoc}) over a temperature range of solution temperatures for the first time. K_{assoc} were measured at temperatures in the range of 5 - 40 °C. From the temperature dependence of K_{assoc}, values of ΔH_{assoc} and ΔS_{assoc} were determined and were in good agreement compared to values determined previously by isothermal titration calorimetry (ITC) technique. The application of temperature-controlled device in competitive binding experiments was also described. A future application of the temperature-controlled nanoES device, is its potential to combine with a functional group replacement strategy [6, 7] to rapidly evaluate the thermodynamic contributions of individual ligand functional groups or protein residues to protein-ligand binding. The comparison between mutant protein complexes with wild type protein

158

complexes can provide important insight into the nature of interaction(s) between a protein and its ligand. Our temperature-controlled nanoES combined with FT-ICR/MS also provides a fast and sensitive method with the advantage of low amount sample intake (~10 μg) compared to routinely used ITC technique with ~mg sample consumption for each analysis. In Chapter 5, we investigated the influence of solution conditions (protein concentration, temperature, pH, and ionic strength) on the stability of the assembly of the B subunits of Shiga toxins (Stx's) 1 and 2 using temperature-controlled nanoES-FT-ICR/MS. X-ray crystallography analysis predicated similar higher order structure for the B_5 homopentamers of Stx1 and Stx2. At subunit concentration range from 5 to 85 μM and solution temperature range 0 - 60 °C and at neutral pH, Stx1 B_5 was almost observed as the homopentamer, independent of the ionic strength. In contrast, the degree of assembly of Stx2 B subunit have shown dependence on subunit concentration, temperature, pH, and ionic strength. At subunit concentrations > 50 μM, neutral pH, and 25 ° C Stx1 B_5 exists prominently as pentamer, it dissociates into smaller oligomers and monomers when one or more of these parameters were changed. It is concluded that, under the solution conditions investigated, Stx2 B_5 is thermodynamically less stable than that of Stx1 B_5 which may provide an explanation for the greater toxicity of Stx2 relative to Stx1. In an effort to establish whether a link between the stability of Stx B subunits and Shiga toxin toxicity exists, our laboratory has undertaken a comparative study of the stabilities of the Shiga toxin, both wild type and mutated, and the relative toxicities.

159

Literature Cited

(1) McLuckey, S. A.; Habibi-Goudarzi, S. *J. Am. Chem. Soc.* **1993**, *115*, 12085-12095.

(2) Little, D. P.; Aaserud, D. J.; Valaskovic, G. A.; McLafferty, F. W. *J. Am. Chem. Soc.* **1996**, *118*, 9352-9359.

(3) Wan, K. X.; Gross, M. L. *J. Am. Soc. Mass Spectrom.* **2001**, *12*, 580-589.

(4) Luo, H.; Lipton, M. S.; Smith, R. D. *J. Am. Soc. Mass Spectrom.* **2002**, *13*, 195-199.

(5) Wan, K. X.; Gross, J.; Hillenkamp, F.; Gross, M. L. *J. Am. Soc. Mass Spectrom.* **2001**, *12*, 193-205.

(6) Kitova, E. N.; Bundle, D. R.; Klassen, J. S. *J. Am. Chem. Soc.* **2002**, *124*, 5902-5913.

(7) Kitova, E. N.; Bundle, D. R.; Klassen, J. S. *J. Am. Chem. Soc.* **2002**, *124*, 9340-9341.